TUNABLE VAN DER WAALS-BASED METASURFACES FOR PERFECT ABSORPTION, SENSING, RADIATIVE HEAT TRANSFER, BEAM SPLITTING AND 5G/BEYOND APPLICATIONS

A THESIS SUBMITTED TO

THE GRADUATE SCHOOL OF ENGINEERING AND SCIENCE

OF BILKENT UNIVERSITY

IN PARTIAL FULFILLMENT OF THE REQUIREMENTS FOR

THE DEGREE OF

MASTER OF SCIENCE

IN

ELECTRICAL AND ELECTRONICS ENGINEERING

By

Veysel ERÇAĞLAR

September 2022

Tunable Van Der Waals-Based Metasurfaces for Perfect Absorption, Sensing, Radiative Heat Transfer, Beam Splitting and 5G/Beyond Applications

By Veysel ERÇAĞLAR

September 2022

We certify that we have read this thesis and that in our opinion it is fully adequate, in scope and in quality, as a thesis for the degree of Master of Science.

Ekmel Özbay(Advisor)

Sefer Bora LİŞESİVDİN

Vakur Behçet ERTÜRK

Approved for the Graduate School of Engineering and Science:

Orhan Arıkan
Director of the Graduate School

ABSTRACT

TUNABLE VAN DER WAALS-BASED METASURFACES FOR PERFECT ABSORPTION, SENSING, RADIATIVE HEAT TRANSFER, BEAM SPLITTING AND 5G/BEYOND APPLICATIONS

Veysel ERÇAĞLAR
M.S. in Electrical and Electronics Engineering
Advisor: Ekmel Özbay
September 2022

Metasurfaces are thin, subwavelength structures that have extraordinary properties that cannot be found naturally. Tunable metasurfaces drew attention not only for their lightweight designs but also with the tunning option, having multiple responses without complex fabrication steps for each desired response. Besides tuning the structures by their intrinsic properties, the addition of van der Waals materials which are a specific type of 2D materials, can expand their tuning flexibilities and offer a wide range of applications. Here, we propose and investigate tunable metasurfaces in the following areas: Perfect Absorption, Sensing, Radiative Heat Transfer, Beam Splitting and 5G/Beyond Applications as: 1. All-Dielectric Metamirror for thermally tunable spectrally selective absorber, 2. Metasurface Design for Phonon-Induced Transparency and Nearly Perfect Resonant Absorption, 3. Near-Field Radiative Heat Transfer in Parallel-Plate Structures, 4. Gradient Metasurfaces for Beam Splitting and Light Absorption, 5. 5G and Beyond applications of mentioned works and future outlook.

In the first work, we numerically propose a temperature-tunable, ultra-narrowband one-way perfect near-infrared radiation absorber with high transmission in the longer wavelength neighboring spectral range. We obtained this functionality by using a guided-mode resonance-based grating-waveguide metamirror that is comprised of silicon, a spacer dielectric, an absorbing semiconductor, and germanium. Within the ultra-narrow bandwidth of the guided-mode resonance excited at 1.16 μm with a full width at half-maximum of 3.3 nm, we confirmed perfect absorption when light is incident from one of the two opposite directions. Excitation from the opposite direction resulted in perfect reflection. The

thickness of the entire structure is limited to about one third the operating wavelength. Furthermore, due to the temperature tunability of silicon and germanium the thermo-optical sensitivity was found to be approximately 0.068 nm/K. In addition to this spectral tunability, our proposed device supports transparency windows with 80% transmission in the higher wavelength ranges. Our device is highly promising in the applications of thermo-tunable modulators and obtaining single frequency near-infrared signals from broadband sources.

In the second work, A bi-tunable hexagonal boron nitride (hBN)-based metasurface with bi-functional phonon-induced transparency (PIT) and nearly perfect resonant absorption features in the mid-infrared (MIR) range is proposed. The metasurface, that is composed of axially symmetric hBN rings, is separated from a uniform thin vanadium dioxide (VO_2) film with a SiO_2 spacing layer and is integrated with a top graphene sheet. For the insulating phase of VO_2 (i-VO_2), PIT with an 80% transmission contrast ratio is observed inside the reststrahlen (RS) band of hBN due to the support of hyperbolic phonon polaritons. A considerably large group delay of 9.5 ps and up to 1.8 THz RIU^{-1} frequency shift per refractive index unit is also achieved for the i-VO_2 case. On the other hand, it is found that for the metallic phase of VO_2 (m-VO_2), light transmission is prohibited and nearly perfect resonant absorption peaks are appeared inside the RS band of hBN. Finally, by integrating the hBN-based metasurface into the graphene sheet on the top, a tunable PIT-like effect and nearly perfect light absorption is achieved duo to the hybridization of graphene plasmons and hBN phonons. This leads to a modulation depth as high as 87% in the transmission (i-VO_2) and 62% in the absorption (m-VO_2) responses. Our findings offer a tunable and bi-functional device that is practical for MIR slow-light, sensing, and thermal emission applications.

In the third work, we comprehensively analyze the near-field radiative heat transfer (NFRHT) between a pair of parallel non-rotated BP flakes that occurs due to the tunneling of the coupled anisotropic surface plasmon polaritons (SPPs) supported by the flakes. It is demonstrated that the covering of the BP flakes with (hBN) films leads to the hybridization of the BP's SPPs with the hBN's hyperbolic phonon polaritons and to the significant enhancement of the NFRHT at the hBN's epsilon-near-zero frequencies. It is also shown that the NFRHT in the BP/hBN parallel-plate structure can be actively switched between the ON and OFF states by changing the chemical potential of the BPs and that

the NFRHT can be modified by altering the number of the BP layers. Finally, we replace hBN with $\alpha - MoO_3$ and explore how the NFRHT is spectrally and strongly modified in the BP/$\alpha - MoO_3$ parallel-plate structure. We believe that the proposed BP/polar-vdW-material parallel-plate structures can prove useful in the thermal management of optoelectronic devices.

In the fourth work, we propose multifunctional gradient metasurfaces that are composed of a periodic array of binary Si microcylinders integrated with VO_2 and graphene. The metasurfaces act as transmittive (reflective) beamsplitters for the dielectric (metallic) phase of VO_2 with a switchable characteristic. Moreover, by integrating the metasurfaces with graphene and modifying its chemical potential, one can tune the intensity of the split beam as well as obtain nearly perfect resonant absorptions. Consequently, the proposed metasurfaces can find potential applications in THz interferometers, multiplexers, and light absorbers.

Finally, the works mentioned above, as well as diverse works in the literature will be explained and discussed upon emerging technologies in the area of communication and applications for 5G and mostly beyond and future outlook.

Keywords: Metamaterials, 2D Materials, Perfect Absorber, Sensor, Radiative Heat Transfer, Beam Splitter, 5G and Beyond.

ÖZET

MÜKEMMEL SOĞURUCU, SENSÖR, IŞINIMSAL ISI TRANSFERİ, DALGA AYIRICI VE 5G/ÖTESİ UYGULAMARI İÇİN VAN DER WAALS TABANLI AYARLANABİLİR META-YÜZEYLER

Veysel ERÇAĞLAR
Elektrik ve Elektronik Mühendisliği, Yüksek Lisans
Tez Danışmanı: Ekmel Özbay
Eylül 2022

Metayüzeyler doğal olarak bulunmayan olağandışı özelliklere sahip dalgaboyu-altı ince yapılardır. Ayarlanabilir metayüzeyler sadece hafif tasarımları için değil aynı zamanda birden çok yapı üretmeksizin sadece ayarlayarak çoklu cevap özellikleriyle dikkat çekiyorlar. Kendi ayarlanabilir özelliklerinin yanında, 2 boyutlu malzemelerin özel bir al türü olan van der Waals materyallerinin katkısıyla, ayarlanma esneklikleri artırılarak geniş uygulama alanları sunar. Burada aşağıdaki alanlarda ayarlanabilir metayüzeyler inceledik ve sunduk: Mükemmel soğurucu, sensör, ışınımsal ısı transferi, dalga ayırıcı, 5G ve ötesi uygulamaları: 1. Sıcaklıkla ayarlanabilir spektrum seçici soğurucu için tamamen yalıtkan metayna, 2. Fonon-idüklenmiş geçirgenlik ve mükemmel rezonans soğurucu için metayüzey tasarımı, 3. Paralel plaka yapılarında yakın alan ışınımsal ısı transferi, 4. Dalga ayırıcı ve ışık emici için gradyan metayüzeyler, 5. Bahsi geçen çalışmaların 5G ve ötesi uygulamaları and gelecekteki çalışmalar.

İlk çalışmada, sıcaklıkla ayarlanabilir ultra-darbant tek yönlü yakın kızılötesi uzun komşu dalgaboylarında yüksek geçirgenlikli mükemmel ışın soğurucuyu sunduk. Bu özelliği, silikon, ayırıcı yalıtkan, soğurucu yarıiletken germenyum birleşiminden meydana gelen rehberli-mod rezonans tabanlı ızgara dalga klavuzu metaayna kullanarak elde ettik. Rehberli-mod rezonansı 1.6μm'de bant genişliği maksimum yarısında tam genişlik 3.3nm olacak şekilde uyarıldı, ışık iki zıt yönden birinde çarptığında mükemmel soğurmanın gerçekleştiği onaylandı. Diğer yönden uyarılmada ise mükemmel yansımayla sonuçlandı. Tüm yapının kalınlığı çalışma dalgaboyunun üçte biri ile sınırlandı. Üstelik, silikon ve germanyumun sıcaklıkla kontrol edilebilirliği nedeniyle sıcaklık-optik hassalığı yaklaşık 0.068nm/K olarak

bulundu. Spektrumsal ayarlanabilirliğe ek olarak, sunduğumuz cihazımız daha uzun dalgaboyları aralığında %80'lik geçirgenlik penceresini desteklemektedir. Cihazımız, sıcaklık-ayarlı modulatörler ve genişbant kaynaklardan tek frekans yakın-kızılötesi sinyal elde etme uygulamalarında yüksek gelecek vadetmektedir.

İkinci çalışmada, çift-işlevli fonon kaynaklı şeffaflık(PIT) ve orta-kızılötesi aralığında neredeyse mükemmel rezonans emici özelliklerine sahip, çift-ayarlanabilir altıgen bor nitrür (hBN) bazlı metayüzey sunulmuştur. Eksenel olarak simetrik hBN halkalarından oluşan metayüzey, bir SiO_2 ayırıcı katman ile düz ince bir vanadyum dioksit (VO_2) filminden ayrılır ve bir üst grafen katmanı ile tamamlanır. Yalıtkan VO_2(i-VO_2) fazı için, hiperbolik fonon polaritonlarının desteğinden dolayı hBN'nin reststrahlen (RS) bandı içinde %80 geçirgenlik kontrast oranına sahip PIT gözlemlenir. i-VO_2 durumu için 9,5 ps'lik oldukça büyük bir grup gecikmesi ve 1,8 THz RIU^{-1}'a kadar kırılma indeksi birimi başına frekans kayması da elde edilir. Öte yandan, metalik VO_2 (m-VO_2) fazı için ışık iletiminin engellendiği ve hBN'nin RS bandında neredeyse mükemmel rezonans soğurma tepelerinin ortaya çıktığı bulunmuştur. Son olarak, hBN bazlı metayüzeyin üst kısımına grafen tabakasına entegre edilmesiyle, grafen plazmonların ve hBN fononlarının hibridizasyonu nedeniyle ayarlanabilir bir PIT benzeri etki ve neredeyse mükemmel ışık emilimi elde edilir. Bu, geçirgenlik(i-VO_2) ve soğurma(m-VO_2) yanıtlarında sırasıyla %87 ve %62'ye kadar yüksek bir modülasyon derinliğine yol açar. Bulgularımız, MIR yavaş-ışık, sensör ve termal yayılım uygulamaları için pratik olan ayarlanabilir ve çift-işlevli bir cihaz sunar.

Üçüncü çalışmada, katmanlar tarafından desteklenen eşleşmiş anizotropik yüzey plazmon polaritonlarının (SPPs) tünellenmesi nedeniyle meydana gelen bir çift paralel döndürülmemiş BP katmanı arasındaki yakın alan radyatif ısı transferini (NFRHT) kapsamlı bir şekilde analiz ediyoruz. BP katmanlarının (hBN) filmleriyle kaplanmasının, BP'nin SPP'lerinin hBN'nin hiperbolik fonon polaritonları ile hibridizasyonuna ve hBN'nin sıfıra yakın yalıtkanlık sabiti frekanslarında NFRHT'nin önemli ölçüde artmasına yol açtığı gösterilmiştir. BP/hBN paralel plaka yapısındaki NFRHT'nin, BP'lerin kimyasal potansiyelini değiştirerek AÇIK ve KAPALI durumları arasında aktif olarak değiştirilebileceği ve NFRHT'nin BP katmanlarının sayısı değiştirilerek düzenlenebileceği de gösterilmiştir. Son olarak, hBN'yi $\alpha - MoO_3$ ile değiştiriyoruz ve NFRHT'nin BP/$\alpha - MoO_3$ paralel plaka yapısında spektral olarak ve güçlü bir şekilde nasıl değiştirildiğini araştırıyoruz. Önerilen BP/polar-vdW-malzeme paralel plaka

yapılarının optoelektronik cihazların termal yönetiminde faydalı olabileceğine inanıyoruz.

Dördüncü çalışmada, VO_2 ve grafen ile entegre edilmiş periyodik bir ikili silikon mikrosilindir dizisinden oluşan çok işlevli gradyan metayüzey öneriyoruz. Metayüzey, VO_2'nin yalıtkan (metalik) fazı için değiştirilebilir bir karakteristik ile geçirgen (yansıtıcı) ışın ayırıcılar olarak davranır. Ayrıca, metayüzeyi grafen ile entegre ederek ve kimyasal potansiyelini değiştirerek, ayrılmış ışının yoğunluğunu ayarlayabilir ve neredeyse mükemmel rezonans soğurmaları elde edilebilir. Sonuç olarak, önerilen metayüzey THz interferometreler, çoklayıcılar ve ışık emicilerde potansiyel uygulamalar bulabilir.

Son olarak, yukarıda bahsedilen çalışmalar ve literatürdeki çeşitli çalışmalar açıklanacak, iletişim ve 5G ve çoğunlukla ötesi uygulamaları alanlarında gelişen teknolojiler ve gelecek görünümü üzerine tartışılacaktır.

Anahtar sözcükler: Metamayeryaller, 2D Materyaller, Mükemmel Soğrucu, Sensör, Işınımsal Isı Transferi, Dalga Ayırıcı, 5G ve Ötesi.

Acknowledgement

Above all, I would like to thank my academic advisor Prof. Ekmel Ozbay for his support and always being available for his students even though he has a very heavy schedule. During my study, he never let me to feel alone in my research. I will follow his example in my life as being such a hard-working person.

Next I would like to thank Prof. Sefer Bora Lişesivdin and Vakur Behçet Ertürk for being in thesis committee and providing valuable feedbacks to my thesis.

I owe my thanks to whole NANOTAM family but at first Dr. Hodjat Hajian, as helping me entire time I was there. Also I want thank to Oguz Odabasi and Tayfur Kaya not only sharing the same office for years but also providing their warm friendships and support always. Again, for being such great friends I want to thank to my friends Volkan Erturk and Deniz Umut Yildirim. I know we will meet again with all four of you guys! I want to thank Ataollah Kalantari Osgouei, Ebru Buhara, Ekin Bircan Bosdurmaz, Imre Ozbay. I want to especially thank to Gamze Segmenoglu, Mehmet Ozgur always helping with any problems.

In the Electrical and Electronics Engineering department, I would like to thank to Aydan Gencel being always available for any problems and never tired of explaining anything. In UNAM, I want to thank to Abdullah Kafadenk and Taha Ilikkan for their help in the cleanroom and trainings.

I thank to Fatih Develi and Furkan Gecekusu, since I first moved, just knowing the presence of them in Ankara was giving warmth and welcoming environment and having great times during our trips. My special thanks goes to Dilek Sevval Tumer for being great and close friend, when having hard time you know she is always there to listen, I know in the future you will be great psychologist!

Finally, the reason of my existence, and made me who I am today, words cannot be sufficient but I thank to my parents Zübeyde and İzzet Erçağlar and

of course my sisters Fatma and Ayşegül.

I want to thank to Mustafa Ilker Beyaz, Umit Demirbas, Cesim Erten and Yusuf Ozturk for opening this path from my undergraduate study.

Lastly, I thank to TUBITAK and BTK for supporting my study.

Contents

List of Figures

"This page intentionally left blank . . . "

Chapter 1

Introduction

This chapter is on part reprinted with permission from:
Veysel Erçağlar, Volkan Erturk, Amir Ghobadi, Deniz Umut Yildirim, and Ekmel Ozbay, *Optics Letters*, 2020, 45, 6174-6177, DOI: 10.1364/OL.409586
Veysel Erçağlar, Hodjat Hajian, and Ekmel Özbay, *Journal of Physics D: Applied Physics*, 2021, 54(24), 245101, DOI: 10.1088/1361-6463/abecb2
Hodjat Hajian, Ivan D. Rukhlenko, **Veysel Erçağlar**, George Hanson, and Ekmel Özbay, *Applied Physics Letters*, 2022, 120, 112204, DOI: 10.1063/5.0083817
Veysel Erçağlar, Hodjat Hajian, Andriy E. Serebryannikov, and Ekmel Özbay, *Optics Letters*, 2021, 46, 3953-3956, DOI: 10.1364/OL.435197
Ekin Bircan Boşdurmaz, Hodjat Hajian, **Veysel Erçağlar**, and Ekmel Özbay, *Journal of the Optical Society of America B*, 2021, B 38, C160-C167, DOI: 10.1364/JOSAB.427975

1.1 Background

1.1.1 Metamaterials

People give prominence to materials since the time of alchemy. Although the efforts of alchemists were not realistic, with scientific improvement, scientists started to beat the limits of nature. Eventually, metamaterials emerged. The Greek word *meta* means beyond which ultimately makes metamaterials beyond the regular materials. A metamaterial is a special type of material that cannot be found in nature but have extraordinary features that are physically realizable[1]. By engineering the geometrical parameters and the patterns, an effective refractive index is reached which is not present naturally on Earth. Currently, metamaterials have many different applications in photonics and optoelectronics applications. Such as sensors[2, 3], perfect narrowband[4] or broadband[5, 6, 7] absorbers, reflectors[8], antennas and emitters[9, 10, 11], coolers[12] and other wide range of photonic applications [13, 14, 15, 16, 17, 18, 19, 20, 21, 22].

1.1.2 Van Der Waals materials

Two-dimensional (2D) materials recently attracted great attention, especially after the isolation of graphene [23]. Van der Waals (vdW) materials are a special type of 2D materials that have strong covalent bonds in the 2D plane but weaker van der Waals forces in the third dimension. Thus, they can be easily stacked and isolated. They can be grouped either by their composing elements or by their electronic properties such as graphene, black phosphorus, III-VI, and transition-metal dichalcogenides families [24]. Their advantage of combining heterostructures as well as tuning properties made them admirable candidates in the area of metamaterials and optoelectronic applications. Although the 2D nature of vdW, fabrication steps are straightforward as other materials like chemical vapor deposition (CVD) or exfoliation, wet-transfer, and pick-and-lift techniques [23]. Further details of the materials used in this thesis will be discussed in the coming

chapters.

1.1.3 Simulation

Before fabrication of the metamaterials, structures and the design should carefully be investigated to avoid waste of time and energy. Thus, simulation software packages are available to get rid of any inconvenience. Simulation software packages are very powerful packages to examine thoroughly the structure before they are fabricated. A real-life situation can be applied so that experimenter knows what to expect. Even they are helpful to debug any issues in the experimental setup. simulation tools can be used not only to find reflection, transmission, or absorption results of a given metamaterial structure but also to understand the response to the other independent variables from the environment such as temperature or electric field. In subsections 1.1.3.1 and 1.1.3.2 simulation software of Lumerical and COMSOL will be discussed. Note that all the following discussions will be based on the proposed structure of SRR, differences may occur in the case of other structures or simulation setups.

1.1.3.1 Lumerical

Lumerical is a powerful tool for doing simulations based on a finite-difference-time-domain (FDTD) solver. The software itself includes a graphical user interface (GUI) to design and simulate the structure without switching software. Simulation procedure can be summarized as designing the geometry, setting the simulation region as boundary conditions, sources, monitors and the analysis of the results. In the following, the simulation procedure will be discussed in detail.

1.1.3.1.1 Design Tools

Firstly, the dimension of the simulation should be decided. In Lumerical 2D

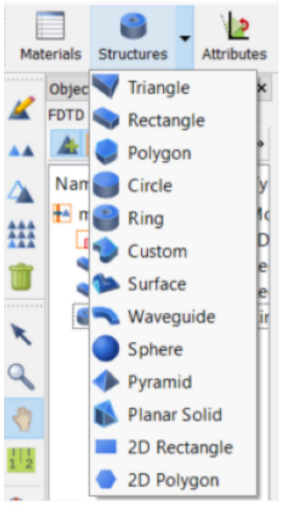

Figure 1.1: Predefined primitive structure in Lumerical

or 3D simulations can be conducted. Even though the final structure is 3D, if applicable, 2D simulation can be chosen to reduce simulation time and memory. To create designs in Lumerical, there are predefined primitive structures as shown in Fig. 1.1. After the combination of primitive structures, desired design of a final metamaterial structure can be created as in Fig. 1.2. Overlapping areas are determined by mesh orders. After finalizing the design of the structure materials should be determined. There is a large number of materials in the material library of Lumerical.

1.1.3.1.2 Simulation and Meshing

After finalizing the design by choosing the correct geometries and materials, the next step is setting the simulation region properly. In order to conduct an appropriate simulation, there are a few points to be careful about while setting the simulation region but before sources and monitors should be placed. For the simulation of the specific structure, the distance between the source and structure should be at least $2 \times \lambda_{max}$ which λ_{max} being the longest wavelength injected. After deciding the distance according to the longest wavelength, the source should be placed by choosing angle, polarization, direction and wavelength

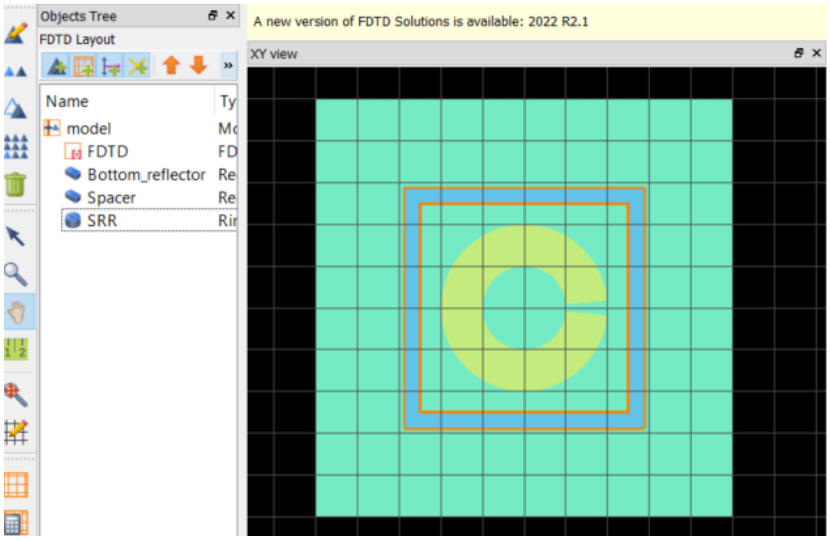

Figure 1.2: Split ring resonator structure in Lumerical

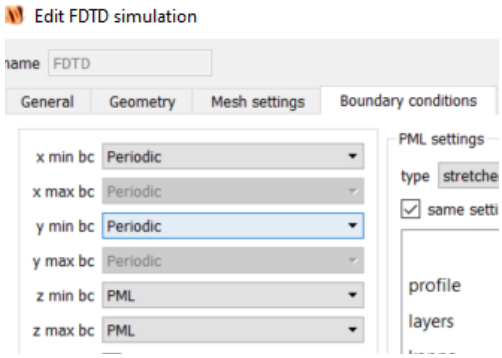

Figure 1.3: Boundary conditions in Lumerical

range. In some cases, the source type (e.g. angled case) or distance between the source and the structure (e.g. near field case) can also be changed. Besides plane wave source, there are other types of sources as well like gaussian or dipole. Next, the setting of the boundary conditions should be decided. In this specific example in Fig. 1.2, boundary conditions should be set to the periodic state in the direction of periodicity and an absorbing layer of perfectly matched layer (PML) in the direction of injection as seen in Fig. 1.3. PML parameters should also be modified in the angled case. Next crucial point is to determine the mesh step. To have a finer result and less oscillation in results, the mesh step should be set as at most the tenth of the smallest feature in structure in each direction. Finally, after setting all the points properly, the simulation region should be as

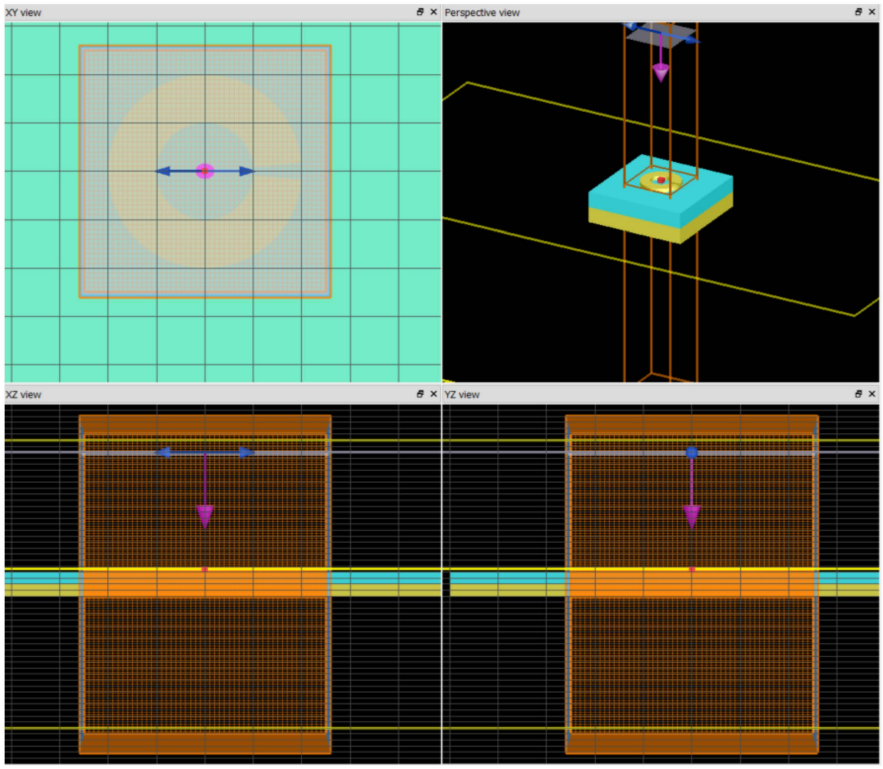

Figure 1.4: Meshing in Lumerical

seen in Fig. 1.4. However, of course, for other examples the points mentioned above can be modified.

1.1.3.1.3 Results

Depending on the size of the simulation region or meshing, a simulation may take from seconds to hours. However, there is always an option to stop the simulation before it reaches an auto-shutoff level without losing data. After a successful simulation, results can be seen from the monitors placed in the simulation region. There are monitors to record data of power, field profiles, time or even movie monitor. Usually, the analysis is conducted on the reflection and the transmission data and the mode profiles. The reflection result of the specific example can be seen in Fig. 1.5. Besides, electric and magnetic field mode profiles can also be investigated from monitors as in Fig. 1.6.

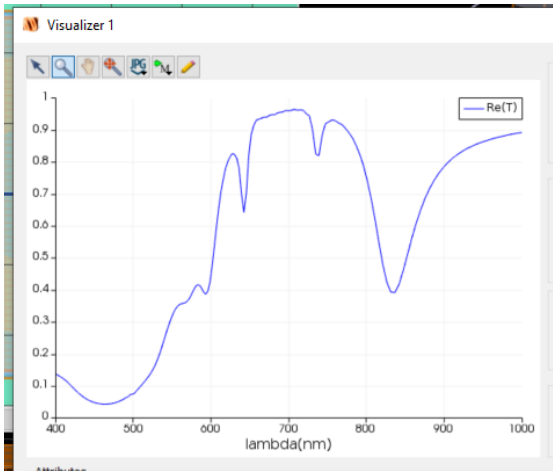

Figure 1.5: Reflection result in Lumerical

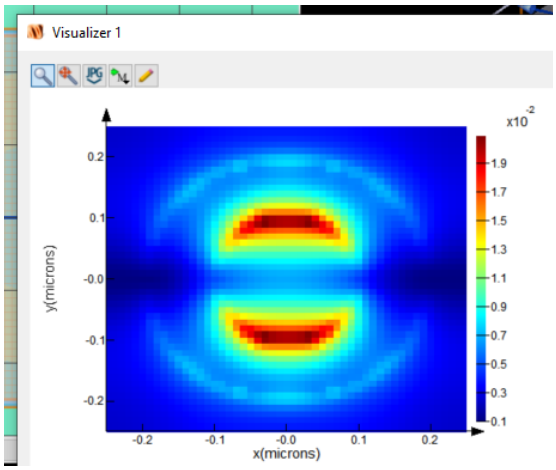

Figure 1.6: Magnetic field mode profile in Lumerical

1.1.3.2 COMSOL

COMSOL is software that supports multiphysics options to combine multiple solvers from other modules. For instance, optical simulation can be combined with heat or electrical simulation. The power of combining modules from the multiphysics option makes COMSOL a great tool for even more complex structures. Unlike Lumerical, COMSOL uses the finite element method for its computation. Besides the multiphysics option, as Lumerical, COMSOL also includes a graphical user interface (GUI) to design and simulate the structure without switching software. The simulation procedure is similar to Lumerical and straightforward

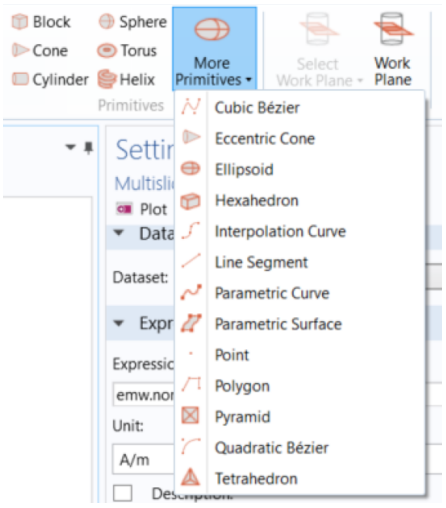

Figure 1.7: Predefined primitive structure in COMSOL

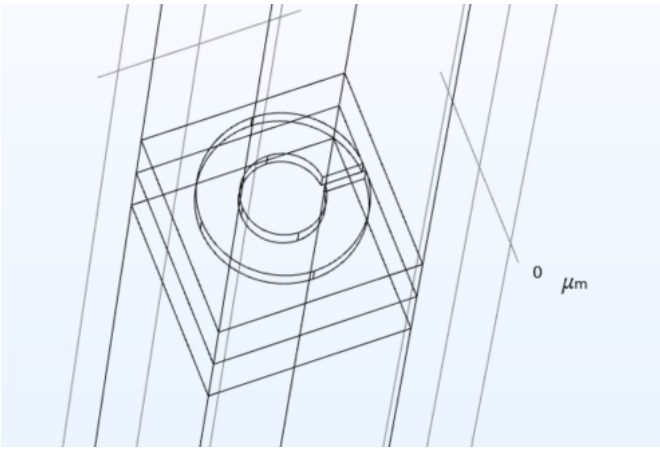

Figure 1.8: Split ring resonator structure in COMSOL

as follows designing the geometry, determining the materials, setting the simulation region by boundary conditions and ports, and adding PML domains can be the main points of setting a comprehensive simulation.

1.1.3.2.1 Design Tools

Just as in Lumerical, firstly simulation dimension should be determined from various options 1D, 2D, 3D or others. Lower dimensions help simulation to be

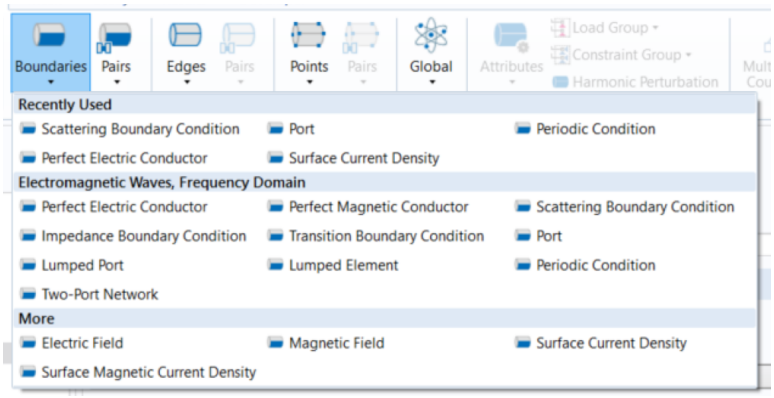

Figure 1.9: Boundary conditions in COMSOL

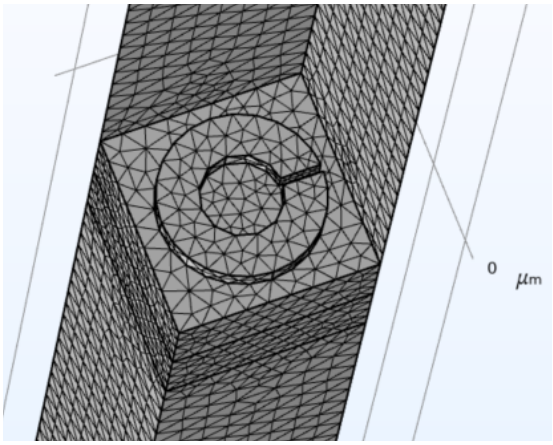

Figure 1.10: Meshing in COMSOL

computed faster, with lower energy, and easy to analyze. To create structures in COMSOL, there are predefined primitive structures as shown in Fig. 1.7. After combining the primitive geometries, desired design of the final metamaterial structure discussed in Fig. 1.2 can also be created in COMSOL as in Fig. 1.8. As the next step, materials should be chosen. There are preexisting materials in the material database of COMSOL but if desired there is always an option to import materials from experiments. Note that in COMSOL, material air should be chosen explicitly.

1.1.3.2.2 Simulation and Meshing

After the design and material preferences are set, the simulation region also should be determined. Note that in COMSOL, the whole simulation region is created by the geometry section. Next, simulation height should be set properly, unlike Lumerical, in COMSOL source is embedded in ports. Distance between the source port and structure should be at least $2 \times \lambda_{max}$ as in Lumerical. The boundary where the source will be injected should be assigned as a port and the option which states that the port will be a source should be checked in the port settings. Again, unlike Lumerical, setting up the boundary conditions in COMSOL is different as seen in Fig. 1.9. To conduct a proper simulation, there are still some points to pay attention to. Boundary conditions should be set to the periodic state in the direction of periodicity as in Lumerical however each boundary should be selected separately. Since the simulation region is periodic, ports also should be set as periodic or continuity explicitly. Also, PML should be set in the direction of injection, not as a boundary but as a domain. Besides, meshing is different, which is set automatically but of course, there is a manual option too. However, the automatic option is better since the meshing is determined by the study and the option that quickly switches from coarser to finer meshes with multiple degrees is another advantage of automatic meshing. The simulation region should be as seen in Fig. 1.10 if it is set properly.

If the simulation region seems to have no problem, the next step is the study should be set which states at what frequency range simulation will be conducted. The study can be from different options such as frequency domain, eigenvalue, etc. However, this option is usually set at the beginning while creating the project but of course, studies can be added later. In this project, the frequency domain is set and the frequency range is selected as in Lumerical. Note that there is a strong relation between meshing and maximum frequency or smallest wavelength.

1.1.3.2.3 Results

Since COMSOL uses the FEM solver, each frequency step is solved separately. This may cause a longer simulation time even though, the geometry is simple.

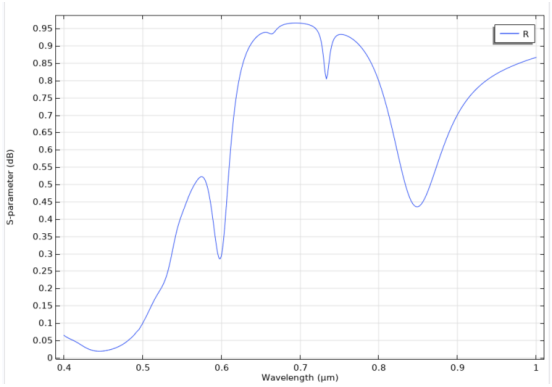

Figure 1.11: Reflection result in COMSOL

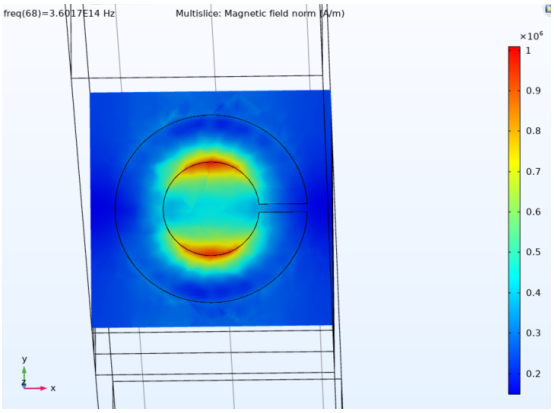

Figure 1.12: Magnetic field mode profile in COMSOL

In the results section of COMSOL after a successful simulation, reflection and transmission results can be visualized as in Fig. 1.11. However, on plain results, mathematical operations can be applied. Besides, electric and magnetic field mode profiles can also be investigated from the results tab as in Fig. 1.12.

1.1.4 Analytical Calculation

In some cases, a simulation may take an enormous amount of time. Obtaining device response by analytical calculation instead of running complex simulations is an easier and more effective way to predict the behavior of the structure by changing the physical parameters. Some devices can be treated as Salisbury screens thus an analytical model can be established on the basic circuit model[25].

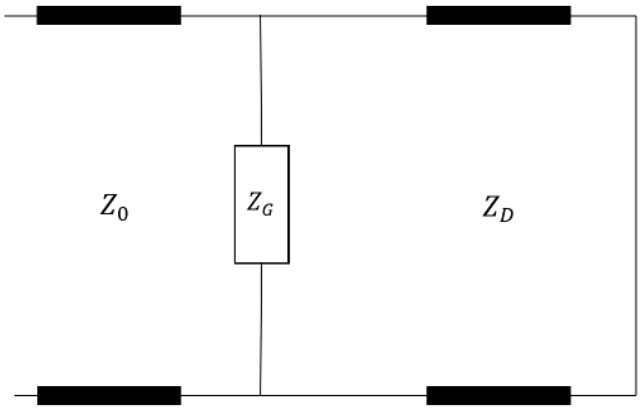

Figure 1.13: Circuit model of a single conductive sheet

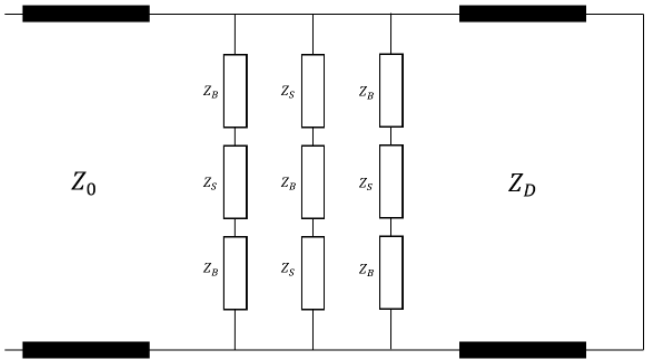

Figure 1.14: Circuit model of a two different conductive sheet combined

Thus, a circuit model of a device can be drawn as seen in Fig. 1.13. To test the analytical model in even more complex structures, different structures can be combined as seen in Fig. 1.14. In this section, the structure in Ref [26] is investigated. Since the structure is composed of two different patches, two different impedances can be set for each patch as Z_S and Z_B for the smaller and the bigger patch, and the overall impedance for the smaller patch is $Z_S = 1/Y_{G,S}$, besides for the bigger patch is $Z_B = 1/Y_{G,B}$. Later, by taking the polarization into account, Z_S and Z_B are connected in series and parallel accordingly as in Fig 1.14.

The admittance of a single graphene patch, Y_G, can be calculated by eq 1.1.

$$Y_G = m_1 \left(\frac{w}{D}\right)^2 \left(\sigma^{-1} + \frac{m_2}{j\omega\varepsilon_{eff}}\right)^{-1} \tag{1.1}$$

Where m_1 and m_2 are constant coefficients, w is the width of the patch, and D is the periodicity. ε_{eff} is calculated by the refractive index of the dielectric layer between patches and the bottom reflector layer as $\varepsilon_{eff} = \varepsilon_0(1 + n_s^2)/2$, and σ is the conductivity of the patch. Besides the admittance of the patches, the admittance of the dielectric layer is also calculated by the formula below in eq. 1.2.

$$Y_D = -j \left(\frac{n_s}{\eta_0}\right) cot(\beta_s h) \tag{1.2}$$

Where η_0 is the impedance of free space, $\beta_s = \frac{\omega n_s}{c}$, and c is the speed of light. After inserting each parameter into the formula, $Y_{G,S}$ and $Y_{G,B}$ are calculated for the smaller and the bigger patches respectively. Next, the input admittances $Y_{in,S}$ and $Y_{in,B}$ are calculated by $Y_{in} = Y_G + Y_D$. From the admittance, impedance values of Z_S and Z_B are calculated by inverting the admittance. Lastly, the equivalent circuit impedance is obtained by the formula, $Z_{in} = \frac{(Z_B + Z_S/2)(Z_B + 2Z_S)}{2Z_B + 5Z_S}$. Finally, after having the final equivalent input impedance, the reflection of the circuit can be calculated with respect to air, Z_0, with formulation $R = \left|\frac{Z_{in} - Z_0}{Z_{in} + Z_0}\right|$ as a one-port network since the bottom reflector layer is thick enough to block any transmission.

After inserting the parameters into the equation, the analytical reflection result is calculated and shown in Fig. 1.15. On top of the analytical calculation, the reflection result from the simulation is also drawn for comparison purposes. As can be seen in Fig. 1.15, results from the simulation and analytical approach are in good agreement. Python script belongs to the calculation can also be found in Appendix B

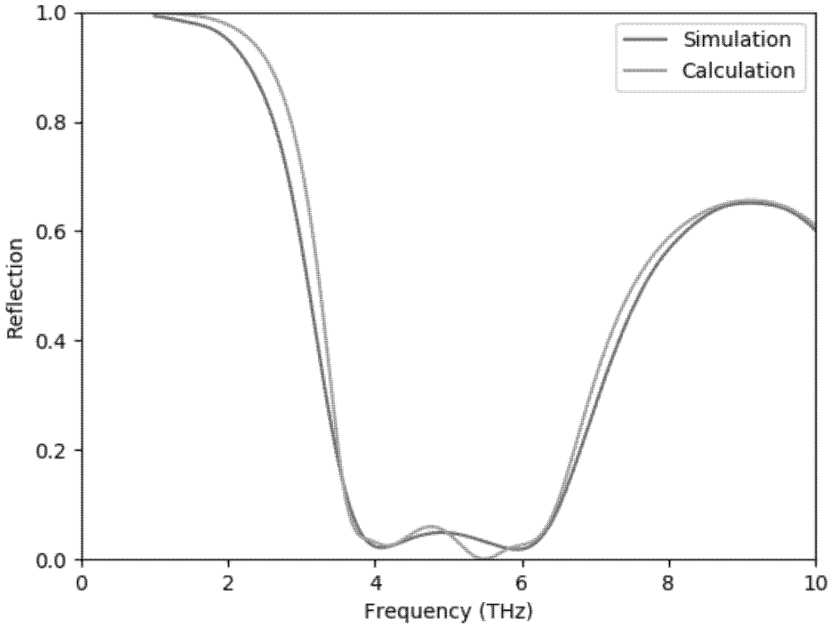

Figure 1.15: Analytical calculation and simulation results are compared

1.2 All-Dielectric Metamirror for thermally tunable spectrally selective absorber

Metamaterials are man-made, i.e. synthetic artificial materials that can achieve optical properties that are not available in nature[1]. In optics, they are used in a wide range of applications such as sensors[2, 3], reflectors[27], imaging devices[28], cloaking and invisibility[29], and perfect narrowband[4] or broadband[5] absorbers. Recently, multifunctional metamaterial devices that yield perfect, one-way electromagnetic wave (EMW) absorption in a required frequency bands[30], have received much interest in passive terrestrial radiative coolers and single frequency receiver from near-infrared (NIR) sources.

There are several proposed structures that achieve the near-perfect absorption of EM waves such as metal-based plasmonic absorbers and one particular structure that is commonly employed in the literature is the metal-insulator-metal (MIM) cavity architecture[31]. The main disadvantage of this approach is the ohmic losses coming from metal layers that reduce the quality factor of optical

cavities and broadens the resonances[32]. In addition to this, using thick metallic reflectors to block the transmission of the radiation in the structure causes the structure to not support transparency and be spectrally selective.

Instead of using optically thick metallic bottom reflectors, by coupling the incident electromagnetic (EM) radiation to the guided modes of the grating structure, perfect reflection is achievable under guided-mode resonance (GMR) conditions[33] for narrow and broadband applications[34]. The thick metallic bottom reflectors of MIM cavities can then be mimicked by these grating structures in a spectrally selective fashion, while simultaneously supporting transparency in the neighboring non-resonant sidebands. Another interesting aspect of grating dielectric grating reflectors is that the spectral position of the excited resonance highly depends on the refractive index of the grating material because it acts as the core material of a dielectric slab waveguide[35, 36]. Therefore, even small changes in the refractive index, which may be induced with temperature, as an example, may cause significant shifts in the position of the excited GMRs[36].

1.3 Metasurface Design for Phonon-Induced Transparency and Nearly Perfect Resonant Absorption

Electromagnetically induced transparency (EIT) is a quantum interference effect that was first observed in a three-level atomic system[37]. This phenomenon leads to a narrow transparent spectrum through an opaque medium accompanied with strong dispersion, and thereby produces ultraslow group velocity and enhanced light-matter interactions [38, 39]. However, because of the specific experimental conditions, such as low temperature and stable gas lasers, the investigations and practical applications of the EIT in an atomic system are significantly completed [37, 38, 39]. To overcome this limitation, extending from microwaves to the visible light regime, plasmon-induced[40, 41, 42, 43, 44, 45, 46, 47, 48, 49, 50, 51] and phonon-induced transparency (PIT) [51] in metamaterials and metasurfaces

have been employed to mimic the aforementioned EIT effect in quantum systems without the need in extreme experimental requirements. The EIT-like response of metastructures exhibit potential capabilities in light modulation and switching [52], sensing [53], and slow light [54] applications.

The EIT-like behavior of metastructures is generally obtained through two main mechanisms, i.e. bright-bright mode coupling[40, 41] and bright-dark mode coupling [43, 45, 46]. The first mechanism is based on the frequency detuning and weak hybridization of two bright modes, while the second one is based on destructive interferences between bright and dark modes.

Achieving dynamic control on the EIT window and light modulation in metastructures without the need to change the geometry of the elements would be considerably advantageous. With this aim, some approaches such as employing thermally tunable superconducting materials [55], optically tunable photoconductive materials[56], and micro-electro mechanical systems (MEMS) based metamaterials have also recently been reported to actively manipulate the transparency window[57]. However, low modulation depth is achievable by the optical and thermal excitations, and complex and massive fabrication steps are needed in MEMS-based metamaterials to achieve high modulation depth. Moreover, most of the aforementioned metastructures are composed of metallic components with natural Ohmic losses that affect their efficiency. Due to its specific features, such as low Ohmic losses, high field confinement and gate-tunable electro-optical response, graphene has also been employed as a building block component to achieve tunable and efficient EIT-like response; i.e. by either patterning graphene itself or by its integration to metasurfaces[58, 59, 60, 61, 62, 63, 64]. Moreover, integrating metasurfaces with anisotropic 2D materials can lead to strong light modulation and tunable EIT-like response[65].

Hexagonal boron nitride (hBN) can be considered as an alternative low-loss material for the mid-infrared (MIR) EIT-like response. hBN is a natural hyperbolic material in the MIR region and is capable of supporting sub-diffractional volume confined hyperbolic phonon polaritons (HPPs or HP^2 modes) for transverse magnetic (TM) polarization[66, 67]. There are two approaches for dynamically

tuning the HP^2s of hBN. The first approach is to integrate hBN with graphene in graphene/hBN heterostructures. This leads to the hybridization of the HP^2s of hBN with surface plasmons polaritons of graphene (SP^2s) and, therefore, the support of hybrid plasmon-phonon polaritons, called SP^3 and HP^3 modes[68]. Due to the presence of graphene, dynamic tuning of the hyperbolic phonons of hBN is achievable by electrostatic gating in the resulted heterostructures. This feature makes the graphene/hBN systems a platform to achieve a new class of tunable waveguides and light modulators operating in the MIR range. The second approach to achieve the dynamic tuning of the HP^2 modes is to employ vanadium dioxide (VO_2). As a phase change material, VO_2 exhibits a dramatic change in its complex refractive index due to a reversible insulator-to-metal transition (IMT) near room temperature. This material can be a promising building block in tunable or reconfigurable metamaterial light absorbers, switches, and modulators [69, 70]. Very recently, the hybridization between the HP^2 modes of hBN and the IMT of VO_2 (i.e. hybrid HP^2-IMT modes) has been theoretically and experimentally investigated in hBN/VO_2 heterostructures[71, 72, 73, 74]. It has been found that the HP^2s of hBN are insensitive to external stimuli and, therefore, by varying the temperature of the heterostructures, it is possible to dynamically tune the spectroscopic phonon resonances of hBN in both reststrahlen (RS) bands. In this way, it is possible to achieve MIR bi-functional devices based on hBN/VO_2 heterostructures. It is worth mentioning that silica gratings bounded by graphene-hBN heterostructures has been recently suggested for the observation of the PIT-like response in the MIR range[75]. Moreover, VO_2 has been also employed as a thermally switchable element in the metastructures with PIT-like responses within the THz range[76, 77]. However, to our knowledge, a bi-tunable VO_2-graphene-integrated hBN-based metasurface with bi-functional PIT-like response has not been reported to the present.

1.4 Near-Field Radiative Heat Transfer in Parallel-Plate Structures

Following the pioneering work of Polder and Hove[78], the near-field radiative heat transfer (NFRHT) has attracted considerable attention in the last two decades due to its promising applications in thermophotovoltaics[79, 80], thermal rectification[81], electroluminescent cooling[82], thermal diodes[83], and transistors[84]. While the propagating waves contribute to the far-field radiative heat transfer[85], the evanescent waves are responsible for the heat flux in the NFRHT-also referred to as photon tunneling.

It is known that the NFRHT is considerably enhanced due the excitation of surface polaritons[86, 87]. The efficiency of the NFRHT can exceed the blackbody limit by several orders in magnitude via the resonant coupling of surface plasmon polaritons (SPPs) in structures based on metals[88, 89], doped Si[78, 79, 80, 81, 82, 83, 84, 85, 86, 87, 88, 89, 90, 91], and surface phonon polaritons in heat transfer devices composed of SiO_2[92], Al_2O_3[93], and SiC[94, 95]. Moreover, it was shown that due to the thermal excitation of isotropic graphene SPPs, NFRHT between two closely spaced parallel-plates of graphene can be strongly mediated, enhanced, and tuned via the modification of the chemical potential of graphene in the infrared range[96, 97, 98, 99].

Black phosphorous (BP) is often used as an anisotropic plasmonic van der Waals (vdW) material for the realization of enhanced NFRHT[100, 101]. It has a tunable bandgap, ranging from 1.51eV for a monolayer BP to 0.59eV for a five-layer BP, and a thickness-dependent anisotropic absorption coefficient[102]. The latter feature implies that, unlike graphene, the SPPs of BP exhibit anisotropic behavior[103]. Moreover, it has been reported that the thermal conductivities of BP along the zigzag and armchair directions are three orders of magnitude lower than that of graphene at 300K[104]. This makes BP a better candidate than graphene for the heat management via NFRHT.

Recent studies have revealed that the NFRHT is greatly enhanced by the

out-of-plane hyperbolic plasmon polaritons or phonon polaritons (HPPs) of metamaterials[105, 106, 107, 108, 109] as well as by the in-plane modes of the graphene-based[110, 111] or BP-based[112] metasurfaces. However, the dependence of the maximum wavenumber of HPPs on the size of the unit cell and the associated fabrication complexity (due to electron beam lithography or several film deposition processes) of the hyperbolic metamaterials or metasurfaces challenge their practical realization for the NFRHT purposes.

Natural hyperbolic vdW materials, such as hexagonal boron nitride (hBN)[113, 114, 115] and $\alpha - MoO_3$[116, 117], have also been used to enhance the NFRHT. It has been demonstrated that the NFRHT can be mechanically tuned in twisted hBN films[114] or actively modulated in graphene-hBN heterostructures[118, 119, 120]. Because $\alpha - MoO_3$ has different optical responses along its three crystallographic directions, a similar mechanical modulation of the NFRHT is observed for the twisted films of $\alpha - MoO_3$ with differently aligned surfaces[117]. Despite a great deal of recent studies on this topic, the active modulation of enhanced NFRHT in non-rotated epsilon-near-zero BP/hBN and BP/$\alpha - MoO_3$ parallel-plate structures has not been analyzed so far to the best of our knowledge.

1.5 Gradient Metasurfaces for Beam Splitting and Light Absorption

Metasurfaces, two dimensional (2D) metamaterials composed of subwavelength resonators, can be utilized to tailor the amplitude, phase, and polarization of an incident electromagnetic wave [121, 122]. Based on these outstanding characteristics, metasurfaces have been used in many applications, such as metamirrors [123, 124], light absorbers [125], polarization converters, holograms, flat lenses, optical vortex generators, and beam splitters [126, 127]. Beam splitters are devices that operate like prisms that split an incident polychromatic wave into its spectrum with varying angles. Since the traditional beam splitters are too

bulky, it is challenging to integrate them with compact photonics devices. Consequently, recently there has been considerable attention in the design and realization of miniaturized metasurface beam splitters (MBSs) operating in the visible [128, 129, 130, 131, 132, 133, 134, 135, 136], infrared [137, 138, 139], terahertz (THz) [123, 140, 141, 142, 143], and microwave ranges [144]. In addition to being categorized according to their operating frequencies, MBSs can also be classified as either transmittive devices or reflective ones. To achieve high efficiency transmittive MBSs by avoiding lossy components, high index dielectric resonators have been employed [129, 134, 135, 136, 138, 140] while either gap-surface plasmon metasurfaces [127, 128, 130, 131, 132, 133, 141, 142] or meta-mirrors [123] have been utilized for the realization of reflective MBSs. Employing graphene, as a low-loss plasmonic material in the IR and THz ranges, in the design and fabrication of metasurfaces is an alternative approach to overcome the loss effects [139, 143]. Moreover, it is also possible to take advantage of the gate-tunable characteristic of graphene to obtain tunable MBSs. Vanadium dioxide (VO_2) is another example of an active material that exhibits reversible insulator-to-metal transition (IMT) by external stimuli, such as heat, in the visible, IR [145], and THz ranges [146]. Therefore, by taking advantage of its reversible insulator ($i - VO_2$; i.e. $T = 298\ K$) to metal ($m - VO_2$; i.e. $T = 358\ K$) transition, this material can be employed in multifunctional devices with reconfigurable characteristics [138, 146, 147, 148]. It is noteworthy that multifunctional metasurfaces have recently attracted considerable attention due to providing diverse optical functionalities in the desired operating frequencies [149]. However, to the best of our knowledge, no study on a THz metasurface with transmittive/reflective beam splitting and light absorption functionalities has been reported yet.

1.6 Thesis Outline

In chapter 2, we propose an ultra-narrowband one-way perfect absorber tuned by temperature and operating in the near-infrared region with high transmission in the longer wavelength neighboring sideband. This feature is obtained by a guided-mode resonance-based grating-waveguide metamirror that is composed of silicon,

a spacer dielectric layer of silicon nitride, and an absorbing layer of semiconductor germanium. Within the ultra-narrow bandwidth of the guided-mode resonance excited at 1.16 m with a full width at half-maximum of 3.3 nm, perfect absorption is confirmed when light is incident from top-side directions. Excitation from the bottom-side direction resulted in perfect reflection. The thickness of the whole structure is about one-third of the operating wavelength. Furthermore, due to the temperature tunability of materials used, the thermo-optical sensitivity was found to be approximately 0.068 nm/K. In addition to this spectral tunability, the proposed device supports transparency windows with 80% transmission in the higher wavelength.

In chapter 3, we investigate a bi-tunable hexagonal boron nitride (hBN)-based metasurface with bi-functional phonon-induced transparency (PIT) and nearly perfect absorption functionality in the mid-infrared (MIR) range. The structure is composed of axially symmetric hBN rings, SiO_2 spacing layer, a uniform thin vanadium dioxide (VO_2) film, and integrated a top graphene sheet. For the insulating phase of VO_2 (i-VO_2), PIT with an 80% transmission contrast ratio is found inside the reststrahlen (RS) band of hBN due to hyperbolic phonon polaritons. A large group delay of 9.5 ps and up to 1.8 THz RIU^1 frequency shift per refractive index unit is also achieved for the i-VO_2 case. Furthermore, for the metallic phase of VO_2 (m-VO_2), light transmission is prohibited and nearly perfect absorption peaks appeared inside the RS band of hBN. Finally, integration of the hBN-based metasurface into the graphene sheet on the top, a tunable PIT-like effect and nearly perfect light absorption is achieved due to the hybridization of graphene plasmons and hBN phonons. This leads to a modulation depth as high as 87% in the transmission (i-VO_2) and 62% in the absorption (m-VO_2) responses.

In chapter 4, we analyze the near-field radiative heat transfer (NFRHT) between a pair of parallel non-rotated BP flakes that occurs due to the tunneling of the coupled anisotropic surface plasmon polaritons (SPPs) supported by the flakes. It is shown that the covering of the BP flakes with hexagonal boron nitride (hBN) films leads to the hybridization of the BP's SPPs with the hBN's hyperbolic phonon polaritons and to the significant enhancement of the NFRHT at

the hBN's epsilon-near-zero frequencies. It is also shown that the NFRHT in the BP/hBN parallel-plate structure can be actively switched between the ON and OFF states by changing the chemical potential of the BPs and that the NFRHT can be modified by altering the number of the BP layers. Finally, hBN is replaced with $\alpha - MoO_3$ and how the NFRHT is spectrally and strongly modified in the BP/$\alpha - MoO_3$ parallel-plate structure is explored.

In chapter 5, we propose a multifunctional gradient metasurface that is composed of a periodic array of binary Si microrods integrated with VO_2 and graphene. The metasurface act as transmissive (reflective) beamsplitters for the dielectric (metallic) phase of VO_2 with a switchable characteristic. Moreover, with the integration of the metasurface with graphene and modifying the chemical potential, the intensity of the split beam can be tuned as well as nearly perfect resonant absorptions are obtained.

In chapter 6, for proposed structures in previous chapters, the conclusion and future and potential applications for 5G and beyond are presented.

Chapter 2

Numerical Analysis of a Thermally Tunable Spectrally Selective Absorber Enabled by an All-Dielectric Metamirror

This chapter is on part reprinted with permission from: **Veysel Erçağlar**, Volkan Erturk, Amir Ghobadi, Deniz Umut Yildirim, and Ekmel Ozbay, *Optics Letters*, 2020, 45, 6174-6177, DOI: 10.1364/OL.409586

2.1 Introduction

In this sction, we make use of the finite-difference-time-domain (FDTD) method to numerically propose an all-dielectric absorber that shows high dynamic tunability by temperature. This functionality is obtained by using Si as a grating buried inside a Si nitride (SiN) layer to build a GMR-based metamirror and adding a germanium (Ge) layer as a lossy material on top. The structure with optimized dimensions behaves as a near-perfect absorber for the NIR radiation,

which occurs when the incident radiation is coupled to the guided modes of the grating-waveguide structure. We achieved near-unity absorption at a wavelength of 1160 nm, and the resonance is determined to have a full width half-maximum (FWHM) of 3.3 nm. When the radiation is incident from the opposite direction, near-perfect reflection is also verified. Furthermore, thermo-optical sensitivity was found to be 0.068 nm/K. When NIR radiation is incident from the opposite direction, it behaves as a reflector. In addition to this, deriving this functionality with an all-dielectric structure provides transparency, i.e., high transmission in the lower energy spectral bands neighboring the resonant window. The thickness of the overall structure is also limited to the sub-wavelength range, only 395 nm, as opposed to the operation wavelength of 1160 nm.

2.2 Results and Discussion

2.2.1 Numerical and Theoretical Design of All-dielectric Metamirror

Our proposed structure in Figs. 2.1(a) and 2.1(b) consists of a Si frequency-selective reflector, SiN spacer, and Ge absorbing layer. It is designed in such a way to give different responses when excited from the top or bottom. These two types of excitations are defined as follows: when the incoming radiation is incident from the Ge (Si) side and travels in the $-z$ ($+z$) direction of Fig. 2.1(a), it is defined as forward (backward) excitation.

We utilize FDTD simulations to scrutinize the spectral response of our proposed device. In the simulations, we illuminated the unit cell with a broadband plane-wave at normal incidence whose electric field (E-field) is polarized in the direction (θ=0, p polarization). In the x and y directions of the simulation region, we employed periodic boundary conditions, while in the z direction perfectly matched layers (PML) are adopted. We use two monitors to find the reflected (R) and transmitted (T) power, normalized to the incident power. The dispersion

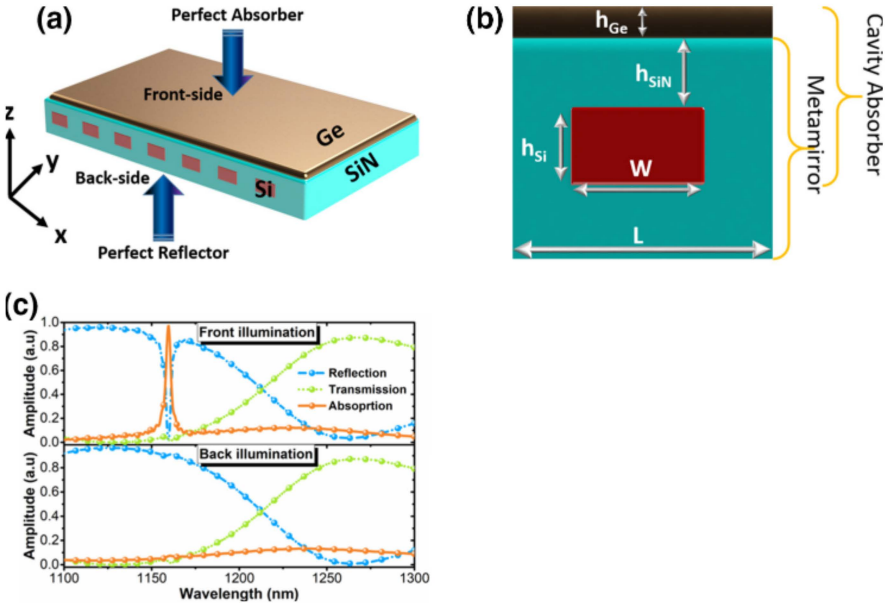

Figure 2.1: (a) Three-dimensional (3D) layout of the structure. (b) Two-dimensional (2D) front view of the structure, scrutinizing the unit cell. Spectral response of the proposed device under (c) forward and backward illumination cases.

effect of Si, SiN, and Ge are retrieved with ellipsometry measurements at 273 K, and they were observed to be in good agreement with the models based on the Sellmeier equation[150].

We started our analysis of the proposed design by setting the geometrical dimensions outlined in Fig. 2.1(a) to their optimized values: thickness of Si grating stripes, h_{Si}=260nm; SiN thickness above and below Si, h_{SiN}=50nm; Ge layer thickness, h_{Ge}=30nm; grating stripe width, W=550nm; unit-cell periodicity, L=975nm. We then simulated this structure to find R and T and passed it to the absorption (A) by using the formula $A = 1 - R - T$. The spectral response of this device, under forward and backward illumination cases, is shown in the top and bottom subfigures of Fig. 2.1(c), respectively. Figure 2.1(c) shows a sharp GMR that peaks at 1160 nm, with a FWHM of 3.3 nm. This figure also proves the asymmetric reflection/absorption property of our device with transparency in the longer wavelength regimes. This asymmetry is because of the fact that under forward excitation and within the bandwidth of this GMR, the Si grating

effectively acts as a mirror, and, with the addition of a SiN spacer and Ge absorbing layers, the structure mimics a Fabry-Perot-type cavity absorber. In the backward illumination case, however, the grating directly reflects the incident radiation before it can reach the Ge layer to be harnessed there.

Excitation of the GMR, which gives our device our asymmetric absorption/reflection functionality, with transparency functionality that stems from the fact that the Si grating, buried inside the SiN layer, also acts a waveguide core, if a diffracted order is phase-matched to a guided mode of the waveguide core. For a one-dimensional (1D) grating, as in this work, this physical phenomenon is governed by Eq. (2.1)[33]:

$$k_{x,g} = mK_x = m\frac{2\pi}{\Lambda_x} = m\frac{2\pi}{L}, \beta = |k_{x,g}\hat{\boldsymbol{x}}|, \tag{2.1}$$

where β is the propagation wavenumber along the guiding direction, Λ_x (K_x) is the grating period (reciprocal lattice vector) along the x direction. m is the diffraction order along the x direction, and $k_{x,g}$ is the wavevector component of the guided mode along the x direction. As the guided mode propagates, it also continually leaks energy to the far field because of the periodicity of the waveguide core. The sharp increase in the reflection is because the re-radiated waves destructively interfere with the directly T waves, but constructively with the R waves.

To further support this result, we use symmetric dielectric waveguide theory, where the core material is the Si-SiN hybrid, and the cladding materials are SiN. For practicality in equations, we assume that cladding layers extend well beyond the evanescent decay length of the guided mode. The effective refractive index of the core material is calculated by adopting Rytovs formula in Eq. (2.2) [151], for the case of the E-field being perpendicular to the grating grooves:

$$\frac{1}{n_{\text{core}}^2} = f\frac{1}{n_{\text{Si}}^2} + (1-f)\frac{1}{n_{\text{SiN}}^2}, \tag{2.2}$$

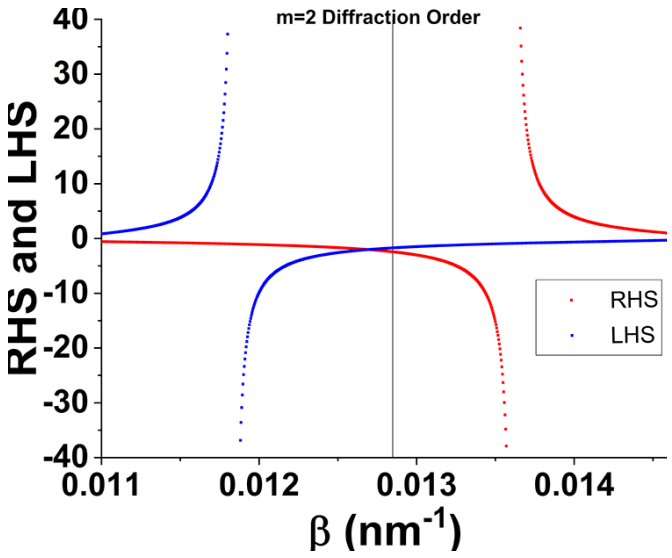

Figure 2.2: Quantitaive analysis of the excited GMR.

$$\tan(ht_{\text{core}}) = \frac{2\bar{p}}{h\left(1 - \frac{\bar{p}^2}{h^2}\right)}, \tag{2.3}$$

where f is the fill factor for the grating, which is W/L in our case. Then, because the incident magnetic field (H-field) is polarized transverse to the grating vector, we investigated the TM-mode excitation in a symmetric dielectric waveguide, the transcendental equation for which is given in Eq. (2.2) [35]. In this equation, $h = k_0\sqrt{n_{core}^2 - n_{eff}^2}$ is the transverse component of the wavevector in the core, $\bar{p} = n_{core}^2/n_{SiN}^2 * k_0\sqrt{n_{eff}^2 - n_{SiN}^2}$ is the decay constant of the guided mode in the cladding. Then, the right-hand and left-hand side (RHS and LHS, respectively) of Eq. (2.3) is plotted, along with Eq. (2.1), with m=2 value, and their intersection is observed in Fig. 2.2. The β value coming from the reciprocal lattice vector is slightly off from the intersection of RHS and LHS. This is because h_{SiN} is picked thin for reasons that will be explained later, so the actual structure differs from the infinite cladding model. Therefore, although Eq. (2.3) gives a firm starting point to investigate mode excitation, it is not totally exact for our case.

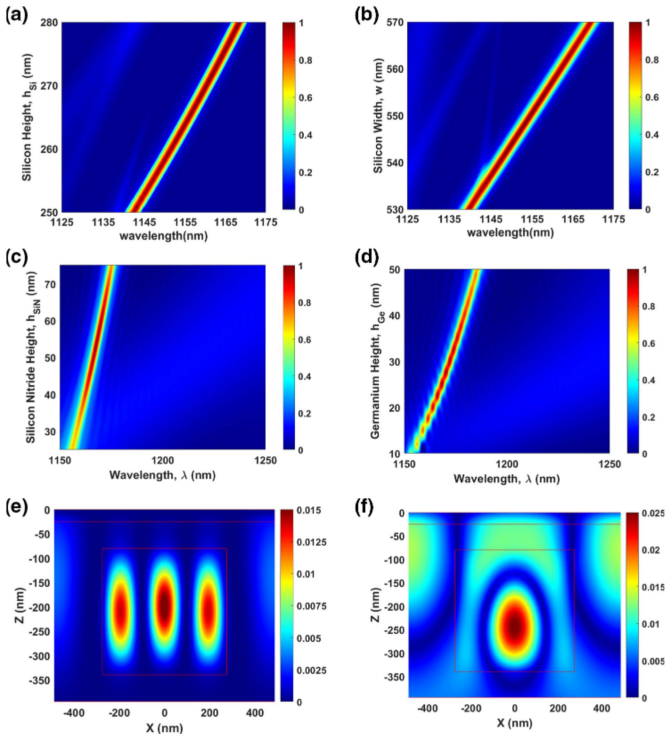

Figure 2.3: Absorption spectra for (a) thickness of Si layer versus wavelength when the width of the Si layer is kept constant at 550 nm and (b) width of Si layer versus wavelength when thickness of the Si layer is kept constant at 260 nm. Absorption spectra for (c) thickness of SiN layer versus wavelength when thickness of the Ge layer is kept constant at 35 nm and (d) thickness of Ge layer versus wavelength when the thickness of the SiN layer is kept constant at 300 nm. At resonant wavelength, H-field magnitude ($|\mathbf{H}|^2$) profile at the XZ plane under (e) forward excitation and (f) backward excitation conditions that are being scrutinized.

Geometrical parameter adjustment also gives our design a wide range of tunability, in terms of the resonant window. By adjusting the geometrical parameters of the Si grating, buried inside the SiN material, we were able to adjust the spectral position of peak reflection, as can be seen in Figs. 2.3(a) and 2.3(b), for changing h_{Si} and W. In Fig. 2.3(a), we sweep h_{Si}, while keeping the other parameters in their aforementioned values. We observed that as h_{Si} is increased, the existing mode red shifts, which is an expected result from the dielectric waveguide theory because modes are supported above a certain normalized core thickness, h_{Si}/λ, so an increase in the former also increases the latter [35]. In Fig. 2.3(b), W is swept while the other parameters are kept constant. It is observed that,

with increasing W, the waveguide mode again red shifts because the waveguide effective core refractive index increases due to the larger filling factor of Si. It is also critical to mention that GMRs can give both a narrowband and broadband behavior depending on the confinement of the mode to the waveguide core and the spectral overlap between distinct modes [34]. For our aim of realizing a dynamically tunable device, we designed our reflector to operate in one of the narrowband modes because a narrow linewidth increases the modulation depth and, consequently, the figure-of-merit[152] in a modulator, which is another potential application of our proposed device. We also swept h_{SiN}, while keeping the other parameters constant, and the result is outlined in Fig. 2.3(c). It is seen that h_{SiN} has an optimum value for perfect absorption because it creates the necessary phase accumulation to redirect the EMWs mostly to the top absorbing layer. Next, h_{Ge} is swept, the results of which are depicted in Fig. 2.3(d). It is seen that a thick layer of Ge cannot give perfect absorption because it decouples the cavity from the incoming radiation, due to not letting the radiation effectively reach the cavity. On the other hand, as h_{Ge} decreases too much, the radiation that is re-directed to this layer cannot be harnessed and leaks out as radiation. It is noteworthy that GMRs red shift when h_{Ge} and h_{SiN} increase. This is because their thickness is picked less than the evanescent decay length of the guided mode in the cladding region, i.e., the SiN-Ge combination, so the optical fields in these layers are not small enough to be neglected, and they necessitate new boundary conditions. Therefore, β and the GMR peak wavelength are modified compared to an infinite cladding dielectric waveguide[34]. Due to this, the optimization of the structure is performed holistically by having all layers present in the simulation, instead of first optimizing the metamirror and then adding the Ge layer. Thicker layers of SiN could be picked to make the GMR wavelength insensitive to variations in h_{Ge} and h_{SiN}, but it would make the device thicker and thereby bulkier. It is also worth mentioning that dielectric spacers other than SiN could also be used, such as Si dioxide (SiO_2) and Magnesium Fluoride (MgF_2). The reason for picking SiN is that GMR linewidth is proportional to the difference between the permittivities of core material and surrounding medium [33], so using SiN results in a smaller linewidth compared to the other two. Compared to other high-refractive index materials like TiO_2, as an example, it provides better

adhesion to Si, so it makes experimental verification more practicable.

2.2.2 Thermal-tuning of the Metasurface

To further discern the resonance behavior, we also plotted the H-field in resonance conditions for forward and backward excitations, the results of which are shown in Figs. 2.3(e) and 2.3(f), respectively. Comparison between these figures indicate two orders of magnitude enhancement H-field and, more importantly, localization in the Si waveguide core. Importantly, Fig. 2.3(e) shows that the third-order mode of the waveguide is excited. The reason for this choice of ours is that higher-order modes, compared to the fundamental mode, can give smaller linewidths due to being closer to the mode cutoff[153]. However, these higher-order modes also necessitate a larger core thickness, h_{Si}, to be supported. We, therefore, used the third-order mode as it gives a good trade-off between these two concerns. Finally, the structure has been simulated for various temperatures. Changes in temperature bring changes in the refractive index of materials and their dimensions. However, changes in dimensions are too small compared to the overall structure, i.e., on the order of 10^{-4}nm[154]. Therefore, our focus has been on the changes in the dielectric permittivity of the materials, especially Si and Ge, to dynamically tune our device. To model the permittivity of the materials as a function of temperature, temperature dependent Sellmeiers coefficients[150] are used to calculate the refractive indices of the materials, as given in Eq. (2.4):

$$\begin{aligned} n^2(\lambda, T) - 1 &= \sum_{i}^{n} \frac{S_i(T) \cdot \lambda^2}{\lambda^2 - \lambda_i^2(T)}, \\ S_i(T) = \sum_{j}^{m} S_{ij}(T) \cdot T^j, \lambda_i(T) &= \sum_{j}^{m} \lambda_{ij}(T) \cdot T^j. \end{aligned} \tag{2.4}$$

Although the refractive index change of Si and Ge with temperature may be approximated as a linear increase, the method above gives more accurate refractive index values. The thermo-optic coefficient (dn/dT) of Si and Ge were

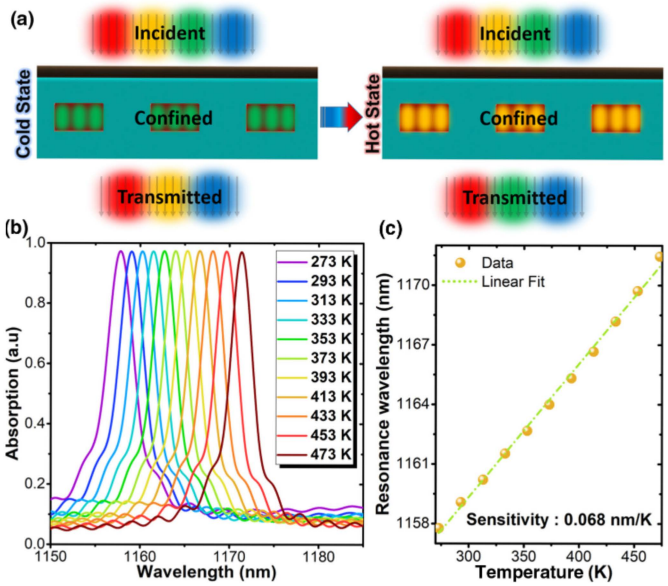

Figure 2.4: (a) Illustration of red shift of the absorption peak as the temperature is increased. (b) Absorption spectrum change with temperature. (c) Resonance wavelengths for different applied temperature values and linear fit in order to find the thermo-optical sensitivity of the proposed device.

found to be approximately $1.9 * 10^{-4} K^{-1}$ and $3 * 10^{-3} K^{-1}$, respectively, between 273 K and 473 K at operating wavelengths[155]. SiN, however, has very small temperature dependency of the refractive index. As the temperature increases, an absorption peak has shifted to longer wavelengths without a change in the absorption amplitude, which is depicted with visible radiation for demonstration purposes in Fig. 2.4(a) and numerically in Fig. 2.4(b). Next, a straight line for the set of resonance peak λ_{max} values with respect to the applied temperature is generated by utilizing the linear polynomial fitting function of MATLAB, and, from the slope of this line, the thermo-optical sensitivity of the structure was found to be 0.068 nm/K, which is shown in Fig. 2.4(c). The equation for this line is $\lambda_{max} = 0.068T + 1138.87$. While the thermo-optic response of Si modifies the core refractive index of the core, the response of Ge modifies that of the cladding, therefore modifying β, and thereby the peak GMR wavelength. This is another reason as to why we picked h_{SiN} thin. By this way, Ge was able to contribute to the thermo-optical sensitivity by being able to influence β, because otherwise the guided mode would decay a lot before interacting with the Ge layer, i.e., only SiN would be influencing β.

2.3 Experimental Approach

Experimental verification of this work can be performed by patterning the Si layer with electron-beam lithography and then deposition of the other dielectric layers. The characterization can be done by using a Fourier transform infrared spectroscopy setup.

2.4 Conclusion

In conclusion, in this chapter, we proposed a metamaterial structure that achieves thermally tunable narrowband absorption from one side and reflection from the other side, while supporting transparency in the higher-wavelength range. In our final design, the device had perfect absorption with a resonance linewidth of 3.3 nm and a thermo-optical sensitivity of 0.068 nm/K.

Chapter 3

VO_2-Graphene-Integrated hBN-based Metasurface for Bi-Tunable Phonon-Induced Transparency and Nearly Perfect Resonant Absorption

This chapter is on part reprinted with permission from: **Veysel Erçağlar**, Hodjat Hajian, and Ekmel Özbay, *Journal of Physics D: Applied Physics*, 2021, 54(24), 245101, DOI: 10.1088/1361-6463/abecb2

3.1 Introduction

In this chapter, we design a metasurface that is composed of periodic array of axially symmetric rings of hBN that are separated from a thin film of VO_2 by a SiO_2 spacer layer. For practical purposes, the VO_2 thin film is considered to be deposited on an Al_2O_3 substrate. It is shown that, based on the destructive

interference between two bright modes supported by the hBN rings, the PIT-like response with a transmission contrast ratio as high as 80% is achieved for the insulating phase of VO_2 (i-VO_2) in the RS band of hBN. Moreover, our analytical investigations on the guided HP^2 modes of a film of hBN proves that the resonances are obtained based on the support of the mentioned modes. It is also expected that, due to the symmetry of the structure, the observed PIT effect would be insensitive to the polarization of the incident wave. Our calculations based on phase of the transmitted light prove that the suggested structure is capable of achieving a 9.5 ps group delay. Moreover, our analysis shows that the hBN-based metasurface represents frequency shift per refractive index unit of up to 1.8 THz RIU^{-1}. On the other hand, by heating the system, for the metallic phase of VO_2 (m-VO_2), the hBN-based metasurface acts as a nearly perfect resonant light absorber at the same resonant wavelengths that the PIT effect was observed for the i-VO_2 case. This unique bi-functional characteristic makes our proposed device an outstanding candidate for MIR slow light, sensing, and directional thermal emission applications. Finally, by integrating the hBN-based metasurface with a top graphene layer, it is proven that, due to the hybridization of graphene SP2s and hBN HP^2s, the optical response of the device, in both m-VO_2 and i-VO_2 cases, can be tuned via the chemical potential of graphene inside and outside of the RS band. This tunable feature leads to a modulation depth as high as 87% in the transmission (i-VO_2) and 62% in the absorption (m-VO_2) responses.

3.2 Results and Discussion

3.2.1 Bi-functional hBN-based Metasurface

A schematic of the hBN-based metasurface considered in this study is shown in figures 3.1(a) and (b).

Perspective view of the hBN-based metasurface is shown in panel (a) of figure

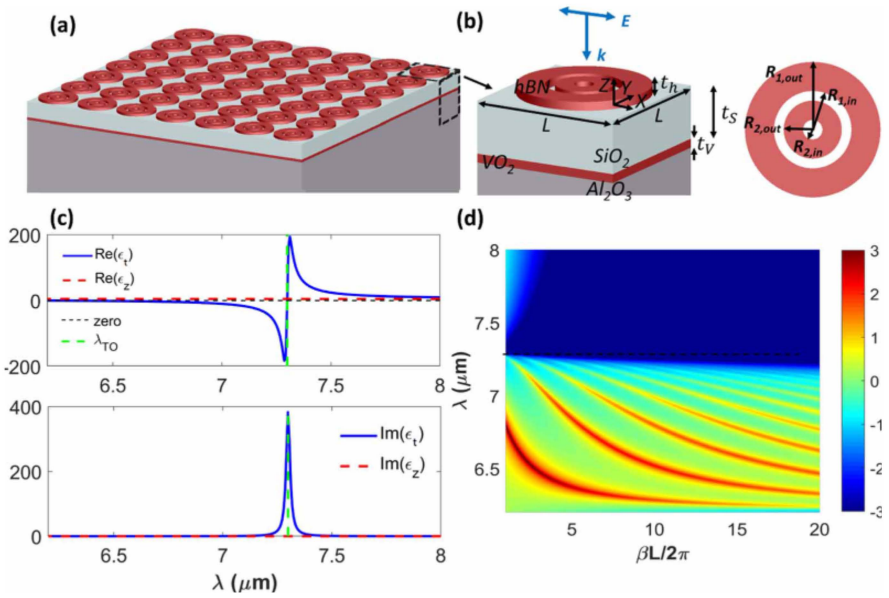

Figure 3.1: (a) Perspective of the hBN-based metasurface. (b) Close-up of a single unit cell of the device. As seen, the hBN-based metasurface of thickness t_{h} (that is placed at $z = 0$) is separated from the VO_2 film (t_{V}) by a SiO_2 spacing layer (t_{S}). Top-view schematic of the axially symmetric hBN rings is also shown on the right hand side of this panel. The rings are labeled as R_1 ($R_{1,\mathrm{out}}$, $R_{1,\mathrm{in}}$) and R_2($R_{2,\mathrm{out}}$, $R_{2,\mathrm{in}}$) in agreement with their corresponding inner and outer radii. Moreover, L denotes the periodicity of the metasurface. Real and imaginary plots of the x- and z-components of permittivity of hBN within the wavelength range of interest in this chapter ($6.2\ \mu\mathrm{m} < \lambda < 8\ \mu\mathrm{m}$) are represented in panel (c). (d) TMM-calculated transmission of light passing through a slab of hBN on SiO_2 substrate. The solid vertical (horizontal) line(s) in panel (c) [(d)] highlight(s) the edge of the RS band of hBN.

3.1. A single unit cell of the metasurface that is composed of axially symmetric hBN rings of thickness t_{h} is depicted in figure 3.1(b). The surface dimensions of the outer (inner) ring is determined by $R_{1,\mathrm{out}}$ and $R_{1,\mathrm{in}}$ ($R_{2,\mathrm{out}}$ and $R_{2,\mathrm{in}}$). As seen, the rings are sperated from the VO_2 film (t_{V}) by the SiO_2 spacer layer of thickness t_{S}. In this paper, the following optimized values are chosen in the calculations: $t_{\mathrm{h}} = 100\,\mathrm{nm}$, $R_{1,\mathrm{out}} = 350\,\mathrm{nm}$, $R_{1,\mathrm{in}} = 200\,\mathrm{nm}$, $R_{2,\mathrm{out}} = 150\,\mathrm{nm}$, $R_{2,\mathrm{in}} = 50\,\mathrm{nm}$, $t_{\mathrm{S}} = 600\,\mathrm{nm}$ and $t_{\mathrm{V}} = 25\,\mathrm{nm}$. The periodicity of the hBN rings is also taken to be as $L = 800\,\mathrm{nm}$. It should be noted that the aforementioned optimized values of the geometrical parameters are obtained by sweeping the parameters in the simulations. The parameter sweep processes are performed to obtain high

transmission contrast ratio in the PIT window for the i-VO_2 case while keeping the resonant absorptive response of the metasurface as nearly perfect in the m-VO_2 case.

It is well-known that the permittivity of hBN is given by [66]

$$\varepsilon_m = \varepsilon_{\infty,m} \times \left[1 + \frac{\omega_{LO,m}^2 - \omega_{TO,m}^2}{\omega_{TO,m}^2 - \omega^2 - i\omega\Gamma_m}\right], m = t, z \tag{3.1}$$

where $\varepsilon_{\infty,t} = 2.95$, $\varepsilon_{\infty,z} = 4.87$, $\omega_{\mathrm{LO},t} = 1610\ \mathrm{cm}^{-1}$ ($\lambda_{\mathrm{LO},t} = 6.2\ \mu\mathrm{m}$), $\omega_{\mathrm{TO},t} = 1370\ \mathrm{cm}^{-1}$ ($\lambda_{\mathrm{TO},t} = 7.3\ \mu\mathrm{m}$), $\omega_{\mathrm{LO},z} = 830\ \mathrm{cm}^{-1}$, $\omega_{\mathrm{TO},z} = 780\ \mathrm{cm}^{-1}$, $\Gamma_t = 4\ \mathrm{cm}^{-1}$ and $\Gamma_z = 5\ \mathrm{cm}^{-1}$. In agreement with the wavelength range of interest in this chapter (i.e. $6.2\ \mu\mathrm{m} < \lambda < 8\ \mu\mathrm{m}$), the real and imaginary parts of the different components of hBN permittivity are illustrated in panel (c) of figure 3.1. As observed, in $\lambda_{\mathrm{LO},t} < \lambda < \lambda_{\mathrm{TO},t}$ hBN acts as a natural type-II hyperbolic material with $\varepsilon_t < 0$ and $\varepsilon_z > 0$. Due to this characteristic, a film of hBN can support sub-diffractional volume HP^2s [30-32]. To understand how the HP^2 modes can strongly/weakly be transmitted through the hBN/SiO_2 system, we employ the transfer matrix method (TMM). Considering the y component of the magnetic field as

$$H_y(z) = \begin{cases} A_i e^{ik_A(z-t_h/2)} + A_r e^{-ik_A(z-t_h/2)}, & z > t_h/2 \\ h_1 e^{-ik_h z} + h_1 e^{ik_h z}, & -t_h/2 \le z \le t_h/2 \\ S_t e^{ik_s(z+t_h/2)}, & z \le -t_h/2 \end{cases} \tag{3.2}$$

and applying the boundary conditions for TM polarization [68], we arrive at $\Im = |t|^2$ with $t = 1/M_{11}$ and $M = \begin{bmatrix} M_{11} \\ M_{12} \end{bmatrix} = M_A^{-1} M_{\mathrm{h1}} M_{\mathrm{h2}}^{-1} M_S$. Here,

$$M_A = \begin{bmatrix} ik_A/\varepsilon_A & -ik_A/\varepsilon_A \\ 1 - i\alpha_g k_A/\varepsilon_A & 1 + i\alpha_g k_A/\varepsilon_A \end{bmatrix}, M_S = \begin{bmatrix} ik_s/\varepsilon_s \\ 1 \end{bmatrix}, \tag{3.3a}$$

$$M_{h1} = \begin{bmatrix} ik_h/\varepsilon_t & -ik_h/\varepsilon_t \\ 1 & 1 \end{bmatrix}, \tag{3.3b}$$

$$M_{h2} = \begin{bmatrix} ik_h e^{ik_h t_h}/\varepsilon_t & -ik_h e^{-ik_h t_h}/\varepsilon_t \\ e^{ik_h t_h} & e^{-ik_h t_h} \end{bmatrix}, \tag{3.3c}$$

and $\alpha_{\mathrm{g}} = \frac{\sigma_{\mathrm{g}}}{i\omega\epsilon_0}$, $k_{\mathrm{h}} = \sqrt{\varepsilon_t(-\beta^2 + \varepsilon_z\beta_0^2)/\varepsilon_z}$, $k_i = \sqrt{-\beta^2 + \varepsilon_i\beta_0^2}$ $(i = A, S)$ $\beta = k_t$, $\beta_0 = \omega/c$. Note that for the results represented in section 3.2.1, $\alpha_{\mathrm{g}} = 0$.

The corresponding TMM-calculated result, figure 3.1(d), shows how the highly transmittive high-β HP^2s can pass through the thin slab of hBN. More investigations prove that by increasing the thickness of hBN, additional closely packed dispersion curves can be achieved. This feature makes hBN very appropriate for guided ray purposes. It is understood from figure 3.1(d) that by appropriately designing the metasurface, it is possible to excite the proper volume confined HP^2 modes within the RS band. In the following subsections, we examine the optical responses of the hBN-based metasurfaces for the i-VO_2 and m-VO_2 phases.

3.2.1.1 i-VO_2 case

As mentioned hereinabove, for practical purposes, we have chosen materials with realistic losses as the spacer (SiO_2) and substrate (Al_2O_3) in the calculations based on Palik's data base [156]. Moreover, experimental permittivity values have been used in the calculations for the i-VO_2 and m-VO_2 phases [69]. Consequently, to demonstrate the PIT-like response, the transmission (T), reflection (R), and absorption (A, i.e. $A = 1 - R - T$) spectra of the considered hBN-based metasurface are shown in figure 3.2(a). It is worth mentioning that Lumerical/FDTD has been utilized to obtain numerical results [157]. In the simulations, the structure is illuminated by a backward-Z plane wave (see figure 3.1(b)). And, periodic boundary condition is applied in X and Y directions while perfect matched layer

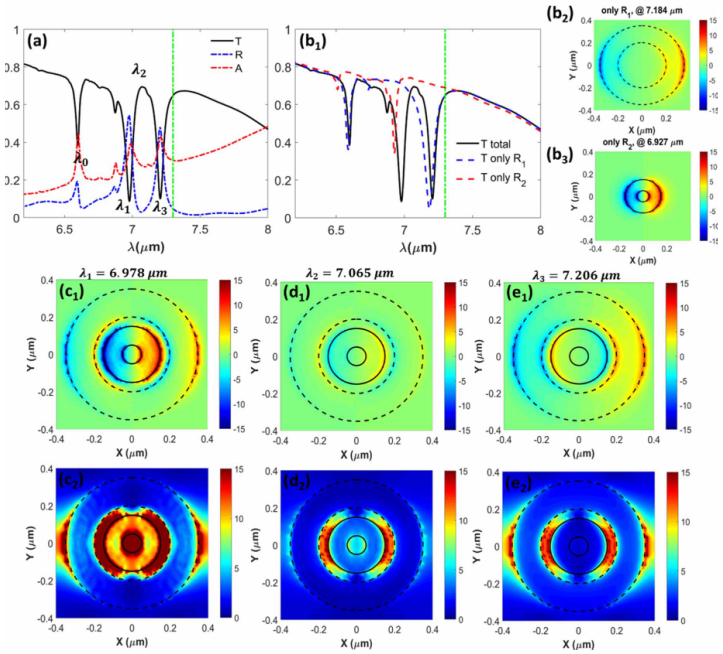

Figure 3.2: Optical responses of the hBN-based metasurface for the i-VO2 case. (a) Transmission (solid-black), reflection (dashed-blue) and absorption (dashed-red) of a normally incident y-polarized light on the metasurface. (b_1) Total transmission (solid-black), R_1-active transmission (dashed-blue) and R_2-active transmission of light through the metasurface. (b_2) and (b_3), respectively, show top-view E_z mode profiles at the longer-wavelength resonant deeps of the dashed-blue and dashed-red curves in panel (b_1). (c_1) and (e_1) represent top-view E_z mode profiles at the strong deeps in total transmission of the structure at $\lambda_1 = 6.978\ \mu$m and $\lambda_3 = 7.206\ \mu$m, respectively. (d_1) illustrates the top-view E_z mode profile at the center wavelength of the PIT window; i.e. $\lambda_2 = 7.065\ \mu$m. Panels (c_2), (d_2) and (e_2) show the corresponding top-view $|\boldsymbol{E}|$ mode profiles. Note that the dashed (solid) circles in the mode profiles highlight the edges of the R_1 (R_2) ring.

one is employed in the Z direction. The hBN-based metasurface is meshed with 10 nm mesh steps and the applied one for the SiO_2 and VO_2 layers are 60 nm and 2.5 nm, respectively.

According to the solid-black curve shown in figure 3.2(a), for an x-polarized incident field, a PIT window with over 70% transmission at $\lambda_2 = 7.065\ \mu$m located between two dips at $\lambda_1 = 6.978\ \mu$m and $\lambda_3 = 7.206\ \mu$m is observed for the insulating phase of VO_2. This is equivalent to a transmission contrast ratio (TR, TR $= \frac{T_{\max}-T_{\min}}{T_{\max}+T_{\min}} \times 100$) of ~80%. Note that in case of removing losses

from both the spacer layer and the substrate, TR value can be increased up to 95%. Moreover, it is evident from the dashed-blue (red) curve in figure 3.2(a) that at the above-mentioned dips of transmission, the structure shows moderately strong (weak) resonant reflective (absorptive) responses for the i-VO_2 case. The absorptive response is stronger than the reflective one at $\lambda_0 = 6.597$ μm. In fact, a second and wide PIT window can also be considered between this resonance and λ_1, but the maximum value of the calculated TR for this case is $\sim$32%. Therefore, in the upcoming investigations for the i-VO_2 case, we focus on the examination of the transmittive and modal features of the hBN-based metasurface at larger wavelengths; λ_1, λ_2 and λ_3.

In order to gain more insight into the physical mechanism behind the PIT effect in the proposed hBN-based metasurface, in figure 3.2(b_1) total light transmission through the metasurface (solid-black) is shown together with transmission once only the R_1 ring is activated (dashed-blue) and for the case only R_2 ring is present (dashed-red). Once the dashed-blue and dashed-red curves are compared with the solid-black one, it is observed that resonances in the total transmission at λ_0 and λ_3 are originated from the R_1 ring while the R_2 ring is responsible for the deep in transmission at λ_1. On the right hand side of figure 3.2(b_1), the corresponding top view E_z mode profiles at the strong deeps in dashed-blue curve in figure 3.2(b_1) for the R_1-active case (@ 7.184 μm) and dashed-red one for R_2-active case (@ 6.927 μm) are also illustrated in figures 3.2(b_2) and (b_3), respectively. The mode profiles clearly represent dipole-activated or bright resonances when R_1 and R_2 rings are separately present in the metasurface. Panels (c_1), (d_1) and (e_1) of figure 3.2, respectively, show top view E_z mode profiles at λ_1, λ_2, and λ_3; i.e. at the corresponding transmission deeps and the PIT peak in the solid-black curve of figure 3.2(a). Similar to the mode profile for the R_2-active case (@ 6.927 μm), it is observed from figure 3.2(c_1) that the R_2 ring exhibits a bright mode response that resembles the one observed in figure 3.2(b_3). Thus it can be strongly excited by the incident field. However, due to a strong, near field coupling between the two rings, two dipole-like resonances with opposite mutual directions are also induced at the inner and outer edges of the R_1 ring at this wavelength. A comparable response is observed at the second strong deep in transmission; i.e. it is observed

in figure 3.2(e_1) that at λ_3 a strong bright mode is supported on the R_1 ring that resembles the R_1-active mode @ 7.184 μm shown in figure 3.2(b_2). Moreover, due to a near field interaction with the R_1 ring, a dipole resonance with the opposite direction is also induced on the R_2 ring, as observed in panel (e_1) of figure 3.2. However, according to figure 3.2(d_1), at the transmission peak at λ_2, the electric field distribution is considerably weakened due to detuning from the resonant conditions at the dips. This can be related to destructive interference of the dipole responses of the R_1 and R_2 rings. In agreement with the E_z mode profiles, the top-view $|\boldsymbol{E}|$ mode profiles are also represented in panels (c_2), (d_2) and (e_2). It is seen that the electric field is considerably localized at the separating gap between the rings, as expected. Moreover, panels (c_2) and (e_2) illustrate that there are electric field localizations between the adjacent unit cells. This point conveys the support of Bloch phononic resonances by the metasurface at λ_1 and λ_3 wavelengths that leads to the appearance of the resonant absorption peaks shown in dashed-red curve in figure 3.2(a).

As mentioned above, it is well-known that the metastructures with the PIT-like response are potentially beneficial for slow-light and sensing applications. Note that the slow-light feature is practical for the case the metasurface operates at the transmittive mode; i.e. for the i-VO_2 case. Therefore, we investigate these applications for the i-VO_2 case. The slow light effect is obtained due to the strong dispersion properties of the PIT window and can be measured by group delay. The group delay is defined as $-\mathrm{d}\varphi/\mathrm{d}\omega$ where φ is phase of the transmitted light [74]. The positive and negative values of the group delay are also related to the slowness and fastness of light passing through the device, respectively.

Panels (a) and (b) of figure 3.3, respectively, represent the phase and the group delay of transmitted light. From panel (a) it is observed that the phase varies from -0.34π to 0.94π within the wavelength range of interest. This leads to the group delay variation from -16.74 ps to 16.74 ps. The calculated value of the group delay at the peak of the PIT window ($T_{\max} = 0.7$ at λ_2) is 9.5 ps that corresponds to 2.85 mm distance delay in light propagation in free space. Moreover, the maximum value of the group delay, i.e. 16.74 ps, is obtained at $\lambda = 7.012\mu$m correspondong to $T = 0.5$. These achieved values are considerably

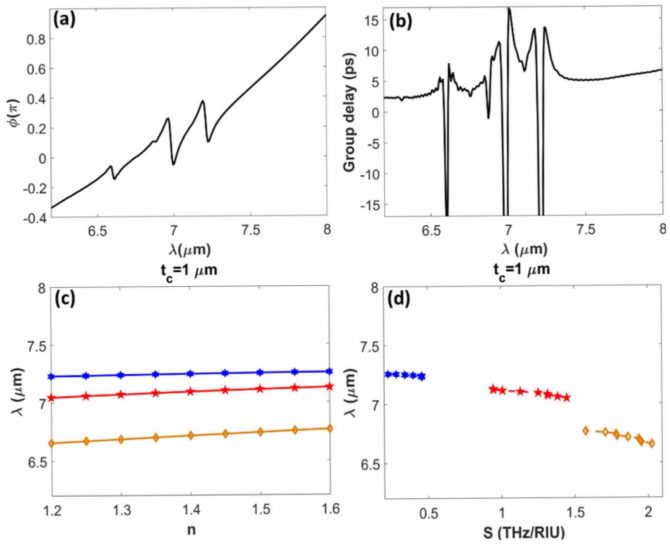

Figure 3.3: Slow-light and sensing features of the hBN-based metasurface for the i-VO_2 case. (a) Phase of transmitted light through the metasurface and the corresponding group delay that is shown in panel (b). (c) Dependence of the resonance frequencies, the three deeps in transmission in figure 2(a) (i.e. λ_0, λ_1 and λ_3), versus changes in the refractive index of the covering medium with thickness of 1 μm. (d) The corresponding sensitivity of the structure for the resonances investigated in panel (c).

higher than the previously obtained ones that have been reported metastructures based on graphene and hBN[58, 59, 60, 61, 62, 63, 64, 75].

Sensing is another remarkable application of the PIT-like response of the metastructures. Figure 3.3(c) illustrates how the wavelengths of the three resonant deeps in the solid-black curve in figure 3.2(a) change via the refractive index of the cladding medium with a thickness of 1 μm. It is seen that the resonance wavelengths linearly red-shifted by increasing the refractive index (n) of the cladding medium from 1.2 to 1.6. To get more insight into this effect, the refractive index sensitivity (S)-that is defined as the frequency shift of the resonances per refractive index change unit (RIU); i.e. $|\mathrm{d}f/\mathrm{d}n|$-is represented in figure 3.3(d). It is observed that a sensitivity up to an averaged value of 1.8 THz RIU^{-1} for $6.656 < \lambda\,(\mu\mathrm{m}) < 6.767$ can be obtained by the hBN-based metasurface.

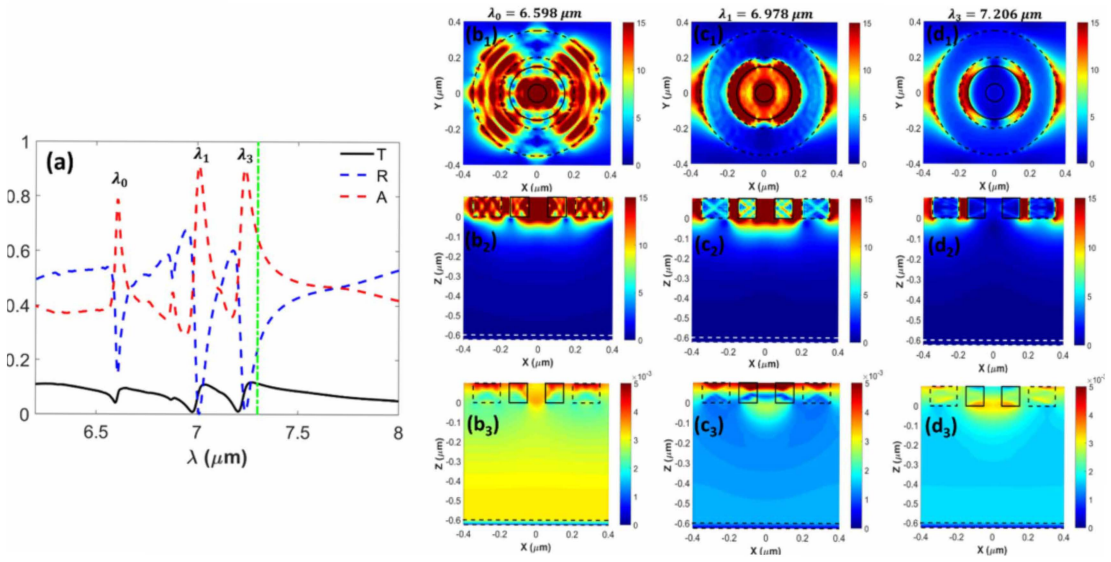

Figure 3.4: Optical responses of the hBN-based metasurface for the m-VO_2 case. Transmission (solid-black), reflection (dashed-blue) and absorption (dashed-red) of the hBN-based metasurface. (b_1), (c_1), and (d_1) illustrate the top-view $|\boldsymbol{E}|$ mode profiles at, respectively, λ_0, λ_1 and λ_3 that correspond to resonant nearly perfect absorption peaks observed in panel (a). In agreement with figure 3.2, the dashed and solid circles highlight the places of R_1 and R_2 rings, respectively. Panels (b_2) [(b_3)], (c_2) [(c_3)], and (d_2) [(d_3)] represent side-view $|\boldsymbol{E}|$ ($|\boldsymbol{H}|$) mode profiles at those wavelengths. In the side-view mode profiles, the bottom (top) dashed (dashed/solid) rectangles highlight place of the VO_2 film (R_1/R_2 hBN rings).

3.2.1.2 m-VO_2 case

It is well-know that due to its temperature-dependent permittivity, VO_2 can be employed as an active component in photonic devices. This material behaves as an insulator at the room temperature while acts as a metal at higher temperatures (85 °C) [69, 70]. In this section, we investigate how the optical response of the hBN-based metasurface can be modified at the m-VO_2 phase. The corresponding results are shown in figure 3.4.

Figure 3.4(a) represent transmission, reflection, and absorption of the hBN-based metasurface for m-VO_2 case. It is observed that by increasing the temperature, transmission is almost 90% blocked owing to the IMT effect and the metallic response of the thin VO_2 film; therefore, reflection is considerably increased. The

rise in reflection for the m-VO_2 case leads to the support of Fabry-Perot cavity resonances and satisfaction of the impedance-matching condition at the resonant λ_0, λ_1 and λ_3 wavelengths. This is the main mechanism in the observation of nearly perfect absorption responses in metamaterials and metasurfaces. Consequently, the functionality of the hBN-based metasurface is switched from transmittive PIT-like feature for the i-VO_2 case to nearly perfect light absorption characteristic for the m-VO_2 case. This bi-functional feature makes the suggested device practical for slow-light, sensing (for the i-VO_2 case) and thermal emission (for the m-VO_2 case) applications. Panels (b_i), (c_i) and ($d_{i=1,2,3}$), respectively, show top- and side-view $|\boldsymbol{E}|$, and side-view $|\boldsymbol{H}|$ mode profiles at the nearly perfect absorption resonances represented in figure 3.4(a). The top view mode profiles shown in Figs. (c_1) and (d_1) resembles the one illustrated in panels (c_2) and (e_2) of figure 3.2. However, figure 3.4(b_1) exhibits the strong propagation of HP^2 rays inside the R_1 ring at $\lambda_0 = 6.598$ μm. In agreement with the top-view mode profile, side-view of $|\boldsymbol{E}|$ at this wavelength, figure 3.4(b_2), verifies this point that the HPP rays are strongly confined inside the rings. This effect is weakened at λ_1 and λ_3, as seen from figure 3.4(c_2) and 4(d_2); at these wavelengths light is mostly confined in the gaps in between the rings. Side-view $|\boldsymbol{H}|$ mode profiles shown in panels (b_3), (c_3) and (d_3) clarify how the magnetic field part of the incident light interacts with the structure, especially with the m-VO_2 film that is highlighted with the dashed rectangles in the bottom of the panels. It is observed from these panels that the magnetic field is not only confined in the hBN-metasurface, but also enhanced in the SiO_2 region that notifies the support of Bloch phononic resonances.

3.2.2 Graphene-Integrated hBN-based Metasurface

In this section, we investigate how the bi-functional optical responses of the hBN-based metasurface can be tuned by integrating it with a top graphene layer. It has been theoretically and experimentally proved that in graphene/hBN heterostructures, the monolayer of graphene can efficiently impact the dispersion characteristics of the HP^2 modes of an hBN film with thickness of up to 300 nm[68]. As

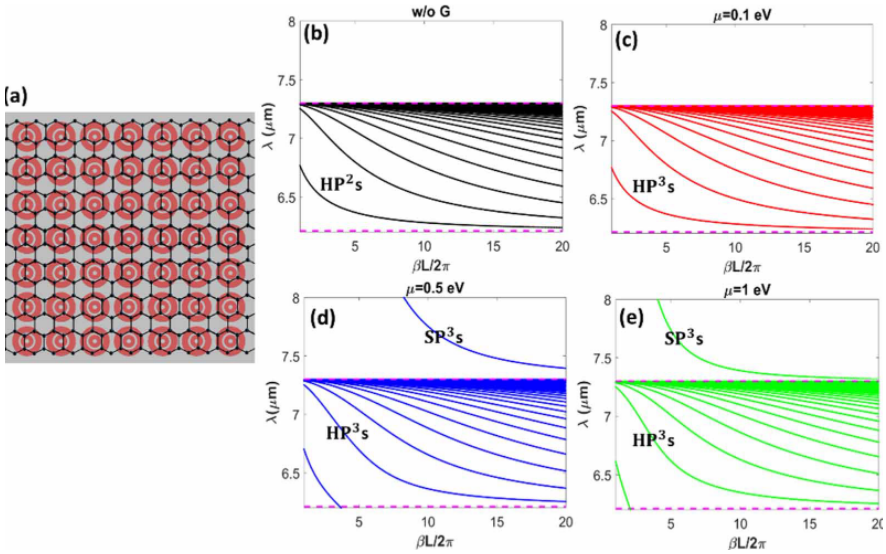

Figure 3.5: (a) Top-view schematic of the graphene-integrated hBN-based metasurface. The graphene layer is considered to be on top of the metasurface. Panel (b), in agreement with figure 3.1(d), illustrates dispersion relation of the guided HP^2 modes supported by the 100 nm thick film of hBN. (c)(e) Represents dispersion relations of the hybrid guided modes supported by the graphene/hBN heterostructure for $\mu = 0.1$ eV, 0.5 eV, and 1 eV, respectively.

mentioned in the introduction part, in the graphene/hBN heterostructures hybrid HP^3 and SP^3 modes can be supported inside and outside of the RS bands of hBN, respectively. Through this hybridization, by modifying the chemical potential of graphene via gating, it is possible to tune hBN's phonons.

Top view schematic of the graphene-integrated hBN-based metasurface is illustrated in figure 3.5(a). In order to obtain a deep insight on how the presence of graphene can affect HP^2s of hBN, we investigate the dispersion of the hybrid guided modes supported by A/G/hBN/sub heterostructure where A, S, and G, respectively, stand for air ($\varepsilon_A = 1$), substrate ($\varepsilon_S = \varepsilon_{SiO_2}$) and graphene. Taking H_y similar to equation (3.1) and applying TM boundary conditions, we arrive at the following dispersion relation of the hybrid guided modes supported by the A/G/hBN/sub heterostructure

$$tanh(q_h t_h) = -\frac{\Gamma_A + \Gamma_S}{1 - \Gamma_A \Gamma_S} \tag{3.4}$$

where $\Gamma_A = \frac{q_h \varepsilon_A}{\varepsilon_t q_A} + \alpha_{\mathrm{g}}$, $\Gamma_S = \frac{q_h \varepsilon_S}{\varepsilon_t q_S}$, and $q_j = -ik_j$ ($j = A,\ h,\ S$). The optical conductivity of the graphene ($\sigma_{\mathrm{g}} = \sigma_{\mathrm{g}}^{\mathrm{intra}} + \sigma_{\mathrm{g}}^{\mathrm{inter}}$), that is a function of frequency and temperature, can also be formulated as[158]

$$\sigma_g^{intra}(\omega, T) = \frac{e^2}{4\hbar}\frac{i}{2\pi}\left\{\frac{16k_BT}{\hbar\Omega} ln\left(2cosh\left(\frac{\mu}{2k_BT}\right)\right)\right\}, \tag{3.5a}$$

$$\sigma_g^{inter}(\omega, T) = \frac{e^2}{4\hbar}\left\{\frac{1}{2} + \frac{1}{\pi} arctan\left(\frac{\hbar\Omega - 2\mu}{2k_BT}\right) - \frac{i}{2\pi} ln\frac{(\hbar\Omega + 2\mu)^2}{(\hbar\Omega - 2\mu)^2 + (2k_BT)^2}\right\} \tag{3.5b}$$

with $\Omega = \omega + i\tau^{-1}$, e is the electron charge, k_{B} is the Boltzmann constant, τ is electron relation time, and $\hbar$ is the Plank constant over 2π. Moreover, the relaxation time of graphene is taken to be $\tau = 0.3$ ps in our calculations in the present chapter. In agreement with figure 3.1(d), dispersion of the guided high-β HP^2s supported by the A/hBN/sub structure is also shown in figure 3.5(b). The numerous, densely packed curves in this figure are a sign of the hyperbolic characteristic of the guided modes in the $\beta_x - \beta_z$ plane. Once graphene is introduced into the structure, i.e. A/G/hBN/sub, for low values of graphene chemical potential ($\mu = 0.1$ eV) no mode is supported outside of the RS band of hBN. Moreover, the dispersion curves of the phononic HP^3 modes inside the RS band are weekly modified, as the red curves in figure 3.5(c) are compared to the black ones in figure 3.5(b). It is observed from panels (d) ($\mu = 0.5$ eV) and (e) ($\mu = 1$ eV) of figure 3.5 that by increasing values of the chemical potential, in addition to modifying dispersion of the HP^3 modes inside the RS band, one branch of plasmonic SP^3 modes is supported outside of it. By comparing figures 3.5(d) and (e), it is understood that, by increasing the chemical potential of graphene, it is possible to shift the supported modes to smaller wavenumbers.

In the last step of our investigations, we examine how the presence of graphene on the top of the hBN-based metasurface, as schematically shown in figure 3.5(a), can affect the response of the device for i-VO_2 and m-VO_2 cases. It should be noted that, in the calculations related to the optical conductivity of graphene, temperature is taken as 27 °C and 85 °C for, respectively, for the i-VO_2 and

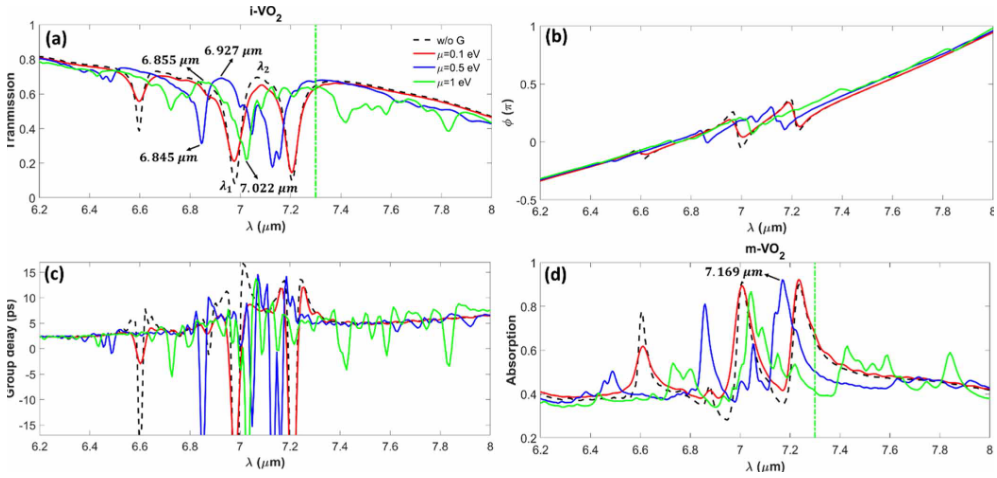

Figure 3.6: (a) Transmission of the graphene-integrated hBN-based metasurface for the i-VO_2 case at different values of the chemical potential of graphene; i.e. $\mu = 0.1$ eV, 0.5 eV and 1 eV. Transmission of the i-VO_2 case at the absence of graphene is also shown with the dashed-black curve as the reference. Panels (b) and (c) are, respectively, the corresponding phase and the group delay of the metasurface for the i-VO_2 case. (d) Absorption of the metasurface for different values of μ for the m-VO_2 case. In agreement with figure 3.4(a), the dashed-black curve shows absorption in the absence of graphene as the reference.

m-VO_2 cases.

Panels (a)-(c) of figure 3.6 examine the effect of the presence of the top graphene layer on the optical response of the device for the i-VO_2 case. In agreement with the point understood in figures 3.5(b) and (c), it is seen from the solid-red curve in figure 3.6(a) that the presence of graphene has negligible effect on the PIT-like response at $\mu = 0.1$ eV. By increasing the chemical potential of graphene till 0.5 eV, HP^3s dispersion are more modified and a branch of SP^3s appeared at $\lambda > 7.3$ μm for $\frac{\beta L}{2\pi} > 8$, see figure 3.5(d). Consequently, at $\mu = 0.5$ eV, the PIT response of the device is considerably modified, as the solid-blue curve is compared to the dashed-black one in figure 3.6(a). It is observed from this figure that the resonances are blue-shifted for this case and in addition to the primary PIT window (centered at λ_2), an additional one is appeared at 6.927 μm (highlighted in figure 3.6(a)). By further increasing the chemical potential, the main resonances in transmission are more shifted to shorter wavelengths and additional resonances are appeared outside of the RS band of hBN at

$\lambda = 7.421\ \mu$m and $7.831\,\mu$m. The appearance of these resonances is due to the support of hybrid SP^3 modes at $\frac{\beta L}{2\pi} > 4$, see figure 3.5(e). It is worth mentioning that at λ_2 an almost 25% modulation depth ($\frac{\left|T_{\mathrm{G}} - T_{\mathrm{w/o\ G}}\right|}{\max\left\{T_{\mathrm{G}}, T_{\mathrm{w/o\ G}}\right\}} \times 100$) is observed once the case for which the graphene layer is absent (i.e. w/o G) is compared to the case of $\mu = 0.5$ eV in figure 3.6(a). Note that, at λ_1 (that is located in the PIT window for the case of $\mu = 0.5$ eV and corresponds to the deep for the w/o G case) almost 87% modulation depth is observed once the solid blue curve and the dashed-black curve in figure 3.6(a) are compared. It should be mentioned that for $\mu = 0.5$ eV the transmission contrast ratio also reaches 38% once transmission values at 6.927 μm and 6.845 μm are compared. Moreover, for $\mu = 1\,eV$, TR = 50% for transmission values at 7.022 μm and 6.855 μm.

As a direct consequence of tunable transmission response of the device for the i-VO_2 case, figure 3.6(b) proves the modification of the phase of transmitted light via the chemical potential of graphene. This effect leads to the direct tuning of the group delay of light passing through the hBN-based metasurface that is shown in figure 3.6(c). As an example, it was mentioned hereinabove that at the absence of graphene, 9.5 ps group delay is achieved at the center of the PIT window at λ_2 whereas it can be increased up to 13.72 ps at $\mu = 1$ eV, as seen from figure 3.6(c). Moreover, at the peaks' wavelengths of the PIT windows for the case of $\mu = 0.5$ eV, i.e. $\lambda = 6.927\ \mu$m and λ_2, the obtained values of the group delay are, respectively, 6.8 ps and 14.55 ps. Furthermore, for $\mu = 1$ eV, the obtained group delay values at $\lambda = 6.855\ \mu$m is 5 ps. This observation verifies that the suggested tunable device is practical for tunable slow-light applications in a broad wavelength range. We also investigated the sensing capability of the graphene-integrated hBN-based metasurface by covering the structure with a 1 μm thick dielectric layer ($1.2 < n < 1.6$). Detailed investigations reveal that for $\mu = 0.5$ eV and 1 eV, a sensitivity up to an averaged value of 2.5 THz RIU^{-1} for $6.925 < \lambda\,(\mu\mathrm{m}) < 7.095$ and $7.118 < \lambda\,(\mu\mathrm{m}) < 7.21$ can be obtained by the hBN-based metasurface, respectively.

The graphene-integrated hBN-based metasurface can act as bi-tunable device with bi-functional features. As a remind, the bi-functionality comes from two

different MIR operating characteristics for different phases of VO_2; i.e. a device with PIT-like response for i-VO_2 phase and nearly perfect narrowband light absorptions for the m-VO_2 phase. Bi-tunability of the device is own to the presence of VO_2 (as a thermally tunable/switchable element) and graphene (as a gate-tunable element). figure 3.6(d) shows how the gate-tunability of graphene can control the nearly perfect absorptive responses of the metasurface. This figure depicts that the resonant absorption peaks of the device can be blue-shifted by increasing μ and some additional resonances appear outside of the RS band of hBN due to the plasmon-phonon hybridization at high values of the chemical potential of graphene ($\mu = 1$ eV). Moreover, as an example of the tunable absorptive response of the device, it is seen that $\sim 62\%$ absorption modulation depth is also obtained at $\lambda = 7.169$ μm, once the peak in the solid-blue curve (that corresponds to $\mu = 0.5$ eV) is compared to the deep in the dashed-black curve in figure 3.6(d). Similar comparisons can be done at the other wavelengths. This bi-tunable attribute makes the bi-functional device capable of operating in a broad wavelength range that enhances its functionalities for slow-light and sensing (for the i-VO_2 phase) and thermal emission (for the m-VO_2 phase) applications. It should also be noted that, due to the symmetry of the structure, the above-examined optical responses are expected to be insensitive to the polarization of the incident light.

3.3 Conclusion

In conclusion, we have proposed a novel metasurface based on axially symmetric hBN rings that is separated from a thin uniform VO_2 film by a SiO_2 layer. For the insulating phase of VO_2, the proposed device exhibits electromagnetic induced transparency with an 80% transmission contrast ratio inside the RS band of hBN due to the support of HPPs. Further investigations prove that, for the i-VO_2 case, a substantially large group delay of 9.5 ps and 1.8 THz RIU^{-1} frequency shift per refractive index unit can also by obtained. On the contrary, for the m-VO_2 case, transmission is eliminated and nearly perfect resonant absorption peaks are observed. By integrating the bi-functional device with a top graphene sheet,

due to the hybridization of graphene plasmons and hBN phonons, tunable PIT-like effect for the i-VO_2 case and nearly perfect light absorption for the m-VO_2 one is observed inside and outside of the RS band. Consequently, a modulation depth as high as 87% in the transmission (i-VO_2) and 62% in the absorption (m-VO_2) responses are achieved. According to our findings, it is expected that the tunable and bi-functional hBN-based metasurface proposed in this study will find potential applications in the MIR slow-light devices, sensors, and thermal emitters.

Chapter 4

Epsilon-Near-Zero Enhancement of Near-Field Radiative Heat Transfer in BP/hBN and BP/$\alpha - MoO_3$ Parallel-Plate Structures

This chapter is on part reprinted with permission from: Hodjat Hajian, Ivan D. Rukhlenko, **Veysel Erçağlar**, George Hanson, and Ekmel Özbay, *Applied Physics Letters*, 2022, 120, 112204, DOI: 10.1063/5.0083817

4.1 Introduction

In the present chapter, we comprehensively analyze the NFRHT between two parallel non-rotated BP flakes covered with hBN films [Fig. 4.1(b)]. It is found that the coupling of the anisotropic plasmons of BP with the hyperbolic phonons of hBN considerably enhances the NFRHT near the edges of the Reststrahlen

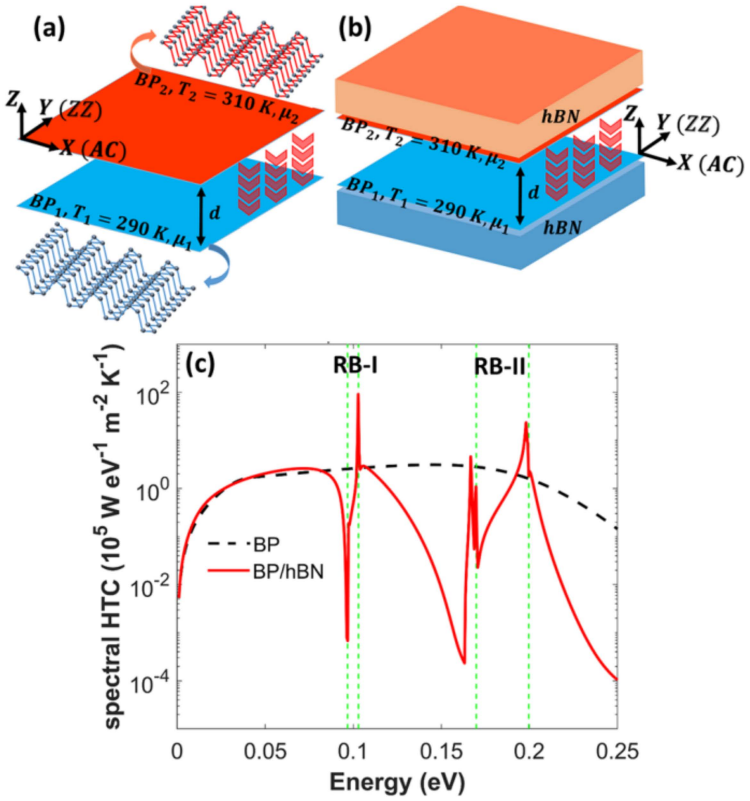

Figure 4.1: A pair of parallel (a) BP and (b) BP/hBN plates separated by a vacuum gap of width d. The temperatures of the emitters and receivers are $T_2 = 310$ and $T_1 = 290K$.(c) SHTC for BP (dashed black curve) and BP/hBN (solid red curve) structures with $N = 3, \mu = 0.1eV$, and $d = 20nm$. Vertical dashed lines are the edges of the RBs of hBN.

bands (RBs) of hBN, where hBN exhibits the epsilon-near-zero (ENZ) feature. We demonstrate the possibilities of the active and passive tunings of the NFRHT through changing the chemical potential and altering the number of layers of the BP flakes. It is also shown that the replacement of hBN with $\alpha - MoO_3$ allows one to strongly manipulate the spectrum of the NFRHT in the structure.

4.2 Results and Discussion

4.2.1 Numerical and Theoretical Design of Parallel-Plate Structures

Figure 4.1(a) shows a schematic of two parallel and non-rotated N-layer BP flakes, which are separated by a vacuum gap of width d. The x and y axes denote the armchair (AC) and zigzag (ZZ) crystalline directions of the BP layers. In Fig. 4.1(b), the BP flakes are covered with hBN films which their optical axes are aligned in the z direction. The top (emitter) and bottom (receiver) layers are kept at constant temperatures of $T_2 = 310$ and $T_1 = 290K$. The NFRHT is characterized by the heat transfer coefficient (HTC), which measures the radiative heat conductance per unit area in the units of $W/(m^2K)$ and is defined by the triple integral[87, 159]

$$\begin{aligned} h &= \frac{q}{\Delta T}, \\ &= \frac{1}{8\pi^3 \Delta T} \int_0^\infty \left[\Theta(\omega, T_2) - \Theta(\omega, T_1)\right] d\omega \iint_{-\infty}^{\infty} \xi(\omega, \beta_x, \beta_y) d\beta_x d\beta_y \end{aligned} \tag{4.1}$$

where q is net power per unit of area exchanged between the parallel plates, $\Theta(\omega, T_i) = \hbar\omega / \left[exp(\hbar\omega/k_B T_i) - 1\right]$ is the mean energy of a Planck oscillator at angular frequency ω and temperature $T_i, \hbar$ is the reduced Planck's constant, $\Delta T = T_2 - T_1$, and k_B is the Boltzmann's constant. Moreover, for the case of $\Delta T \to 0, \frac{\Theta(\omega,T_2)-\Theta(\omega,T_1)}{\Delta T}$ should be replaced with $\frac{\delta\Theta(\omega,T)}{\delta T}$. The energy transmission coefficient or photon tunneling probability for propagating ($\beta < \beta_0$) and evanescent ($\beta > \beta_0$) modes is given by Ref. [87]

$$\xi(\omega, \beta_x, \beta_y) = \begin{cases} Tr\left[(\mathbf{I} - \mathbf{R_2^\dagger R_2}) \mathbf{D_{12}} (\mathbf{I} - \mathbf{R_1^\dagger R_1}) \mathbf{D_{12}^\dagger}\right], & \beta < \beta_0 \\ Tr\left[(\mathbf{R_2^\dagger} - \mathbf{R_2}) \mathbf{D_{12}} (\mathbf{R_1^\dagger} - \mathbf{R_1}) \mathbf{D_{12}^\dagger}\right] e^{-2|k_z|d} & \beta > \beta_0 \end{cases} \tag{4.2}$$

where $\beta_0 = \omega/c, \beta = \sqrt{\beta_x^2 + \beta_y^2}$, and $k_z = \sqrt{\beta_0^2 + \beta^2}$ is the perpendicular wave vector component in vacuum. Here, the dagger denotes conjugate transpose, $\mathbf{I}$ is a 2×2 unit matrix, $\mathbf{D_{12}} = (\mathbf{I} - \mathbf{R_1}\mathbf{R_2}e^{2ik_z d})^{-1}$, and

$$\mathbf{R}_{1,2} = \begin{bmatrix} r_{21,12}^{ss} & r_{21,12}^{sp} \\ r_{21,12}^{ps} & r_{21,12}^{pp} \end{bmatrix} \tag{4.3}$$

includes the Fresnel's reflections coefficients for the s- and p-polarized plane waves incident from the vacuum (medium 2) onto medium 1 and vice versa. The first and second letters of the superscript in each coefficient indicate the polarization states of the incident and the reflected waves, respectively.

In agreement with Ref. [160], the details of derivations, the permittivity of hBN, and the optical conductivity $\sigma(N, \mu, T, \omega)$ of the N-layer BP (where μ is the chemical potential of BP equal to the difference between the Fermi level and the first conduction subband[102]) are provided in the supplementary material of Ref. [161]. In what follows, we calculate the spectral heat flux defined as the HTC per unit photon energy (SHTC) and measured in the units of $W/(m^2 KeV)$. We also assume that $N = 3, \mu = 0.1eV$ (or $n = 6.4 \times 10^{12} cm^{-2}$ in agreement with the experimental data in Ref. [162]) and $d = 20nm$, unless otherwise stated.

Figure 4.1(c) compares the SHTC of the BP and BP/hBN parallel-plate structures. In agreement with the results of Ref. [100], the SHTC of BP (dashed black curve) reaches its peak of 3.1×10^5 at 0.146eV. The proximity of this value to the Wien's frequency at 310K ($\lambda_{max} T_2 = 2898 \mu m K$) indicates thermal occupation at this temperature. The solid red curve in Fig. 4.1(c) shows that the covering of the BP flakes with hBN films considerably enhances the SHTC at the upper edges of the RBs of hBN (i.e., at $\hbar\omega = 0.102$ and 0.198eV), where hBN acts as an ENZ medium. The SHTC in the BP/hBN structure is also notably enhanced compared to the bare hBN structure. Furthermore, the SHTC in the considered structure is higher than in the case of the graphene/hBN parallel-plate structure since $HTC_{BP} > HTC_G$.

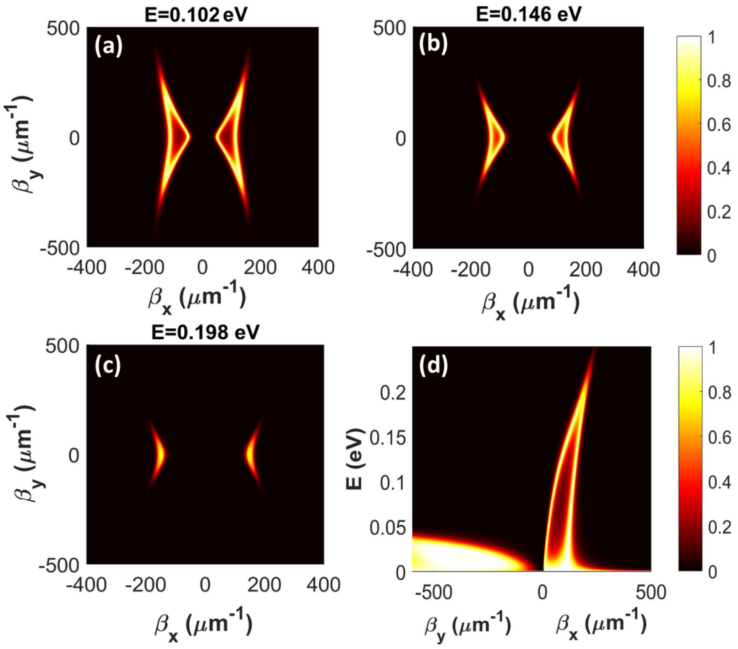

Figure 4.2: Energy transmission coefficient $\xi(\hbar\omega, \beta_x, \beta_y)$ of BP parallel-plate structure for (a) $\hbar\omega = 0.102$, (b) $\hbar\omega = 0.146$, and (c) $\hbar\omega = 0.198eV$. (d) Spectra of energy transmission coefficient along the x and y axes. Regions with high values of ξ in this panel highlight the support of coupled anisotropic SPPs by the BP parallel-plate structure.

4.2.2 Analysis of Energy Transmission

To understand the origin of the enhanced NFRHT in the considered structures, we next analyze their energy transmission coefficients.

Figures 4.2(a)4.2(c) show the plots of $\xi(\omega, \beta_x, \beta_y)$ in the (β_x, β_y) plane for photons of three energies incident onto the BP parallel-plate structure. The emerging density plots, determined by the conductivity tensor components σ''_{yy} and σ''_{xx}, represent two branches of the coupled anisotropic SPPs of the BP flakes. Note that the strong anisotropic response of BP [i.e., $\sigma''_{yy} \gg \sigma''_{xx} > 0$] leads to the canalization of the coupled SPPs along the AC direction (x-axis). The two branches are clearly distinct at $\hbar\omega = 0.102eV$ [Fig. 4.2(a)], while they merge at $\hbar\omega = 0.198eV$ [Fig. 4.2(c)], indicating that the coupling is weakened by increasing the frequency and that the wavenumbers region of non-negligible ξ is

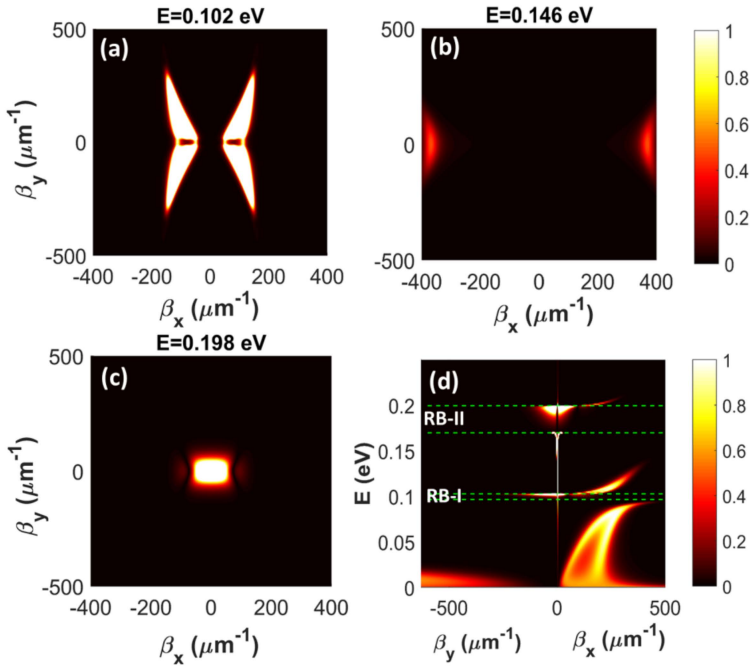

Figure 4.3: Density plots of $\xi(\hbar\omega, \beta_x, \beta_y)$ for hBN-covered BP parallel-plate structure at (a) $\hbar\omega = 0.102eV$, (b) $\hbar\omega = 0.146eV$, and (c) $\hbar\omega = 0.198eV$; horizontal dashed lines in (d) are the edges of the RBs of hBN; and the high-ξ regions indicate the supported hybrid SPP-HPP modes.

getting narrower. Moreover, the tunneling of the hybridized SPPs of the BP flakes leads to high values of the energy transmission coefficients that are recognized as the bright (ξ=1) regions. The brightest region in Fig. 4.2(b) corresponds to the maximum SHTC of the parallel-plate BP structure; i.e., to the dashed black curve in Fig. 4.1(c) at $\hbar\omega = 0.146eV$. Figure 4.2(d) shows $\xi(\omega, \beta_x, 0)$ and $\xi(\omega, 0, \beta_y)$ of the coupled anisotropic SPPs, which are notably different due to the strong anisotropy of BP. It is also seen that the maximum value of $\xi(\omega, \beta_x, 0)$ is achieved over a broad range of frequencies and a narrow range of wave vectors, whereas the situation is reverse for $\xi(\omega, 0, \beta_y)$.

It is known that the integration of an anisotropic 2D material with other functional materials, such as graphene[163] or hBN[164], modifies the supported modes. This is confirmed by Fig. 4.3(a) where the bright regions show that the BP/hBN parallel-plate structure supports hybrid modes of a modified topology and the corresponding ξ reaches its maximum over a broader area in the (β_x, β_y)

plane for $\hbar\omega = 0.102eV$, as compared to Fig. 4.2(a). Note that here topology refers to the trend of regions with high values of ξ. At this frequency, which almost coincides with the upper edge of the RB-I, hBN acts as an ENZ medium with $\varepsilon'_x = -0.2$. The support of the hybrid SPP-HPP mode at the hBN's ENZ frequency leads to a more than 36-fold enhancement of the SHTC, which is represented by the first peak of the solid red curve in Fig. 4.1(c). The small values of ξ at $\hbar\omega = 0.146eV$ [Fig. 4.3(b)] result in the negligible SHTCs in Fig. 4.1(c). Figure 4.3(c) shows the energy transmission coefficient plot of the hybrid SPP-HPP mode with energy 0.198eV, which is close to the upper edge of RB-II and corresponds to $\varepsilon'_x = -0.18$. One can see that the noticeable modification of the mode topology [cf. Fig. 4.2(c)] leads to higher energy transmission coefficients. This explains the considerably high value of SHTC ($= 23.4 \times 10^5$) evidenced by the corresponding sharp peak of the solid red curve in Fig. 4.1(c).

In Fig. 4.3(d), we plot the energy transmission coefficient of the coupled SPP-HPP modes along the x and y axes. One can see that, outside the RBs, the modes predominantly have the anisotropic characteristics of the BP's SPPs, whereas inside the RB-II, they inherit the isotropic features of the hBN's HPPs in the xy plane. It is also observed that the coupling of the HPPs of hBN to the SPPs of BP along the AC direction gives $\xi(\omega, 0, \beta_y)$ its maximum values around the upper edge of RB-I.

As the final point, we analyze how changing the parameters of BP (μ and N), altering the gap d between the plates, and replacing hBN with $\alpha - MoO_3$ modify the NFRHT. The active tuning of the SHTC by varying the chemical potential of BP, which is practically achievable by gating[165], is illustrated in Fig. 4.4(a). It is seen that outside of the RBs, the NFRHT can be switched between the ON ($\mu = 0.2eV$ or $n = 3.3 \times 10^{13} cm^{-2}$) and OFF ($\mu = 0.05eV$ or $n = 1.3 \times 10^{12} cm^{-2}$) states indicated by the double-sided arrows. The ON/OFF functionality comes from the tunability of BP SPPs. In fact, outside of the RBs, the supported modes posses characteristics of SPPs of the BP parallel-plate structure that can be noticeably tuned by μ. This property leads to the tunability of the SHTC of the BP parallel-plate, as discussed in Ref. [100], and consequently the active tuning of the BP/hBN parallel-plates' SHTC. This feature is also observed for

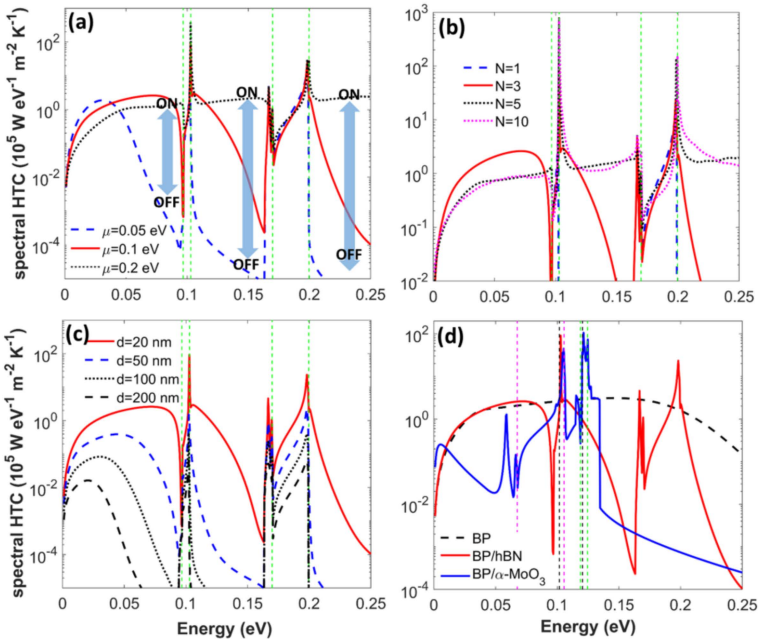

Figure 4.4: SHTC of the BP/hBN parallel-plate structure for different values of (a) $\mu(N = 3, d = 20nm)$, (b) $N(\mu = 0.1eV, d = 20nm)$, and (c) $d(N = 3, \mu = 0.1eV)$ (d) compares the SHTCs of BP, BP/hBN, and BP/$\alpha - MoO_3$ structures for $N = 3, \mu = 0.1eV, d = 20nm$ The vertical dashed lines in (d) are the edges of the RBs of $\alpha - MoO_3$, and the resonances of the SHTC for the BP/$\alpha - MoO_3$ parallel-plates occur at the upper edges; i.e., the ENZ frequencies.

the ENZ frequencies. It is also seen that the SHTC enhancement grows from 11.0×10^5 to 368.3×10^5 for $\hbar\omega = 0.102eV$ and from 15.5×10^5 to 30.6×10^5 for $\hbar\omega = 0.198eV$ when μ is increased from 0.05 to 0.2eV.

It is known that the bandgap and, therefore, the optical properties of the BP thin films are passively tunable via the number of the layers[102]. Therefore, the same feature is expected to be observed for the SHTC. As Fig. 4.4(b) illustrates, for this case, the SHTC is seen to be relatively small for a single-layer BP (dashed blue curve) but steeply grow for $N = 3$ (solid red curve) and saturates at the ENZ frequencies close to the upper edges of the RBs for $N = 5$ (dotted black curve). Since efficient active tuning of the BP flakes is achievable for thicker films[165], dotted pink curve in Fig. 4.4(d) proves that it is still possible to obtain high values of the SHTC at the ENZ frequencies for thick BP films ($N = 10$). Note that we have investigated the SHTC for the other numbers of the BP layers, as

well. However, for the sake of briefness, here the results for $N = 1, 3, 5$, and 10 are presented. Figure 4.4(c) also shows that increasing the gap between the parallel-plates reduces the efficiency of the NFRHT.

The NFRHT in the BP parallel-plate structure can be significantly modified by replacing hBN with another phononic material from the vdW family-$\alpha - MoO_3$. The comparison of the three spectra in Fig. 4.4(d) shows that this replacement: (i) notably enhances the SHTC near the ENZ frequencies of $\alpha - MoO_3$, once solid blue and dashed black curves are compared; (ii) spectrally modifies the SHTC resonances, as the solid blue and solid red curves are compared; and (iii) creates an additional resonance around $\hbar\omega_{LO,y}$ due to the in-plane anisotropy of $\alpha - MoO_3$. Note that due to the in-plane and out-of-plane anisotropy of $\alpha - MoO_3$, $\varepsilon_x \neq \varepsilon_y \neq \varepsilon_z$. This feature leads to the appearance of three resonances at the ENZ frequencies of $\alpha - MoO_3$ (i.e., at $\hbar\omega_{LO,x} = 0.12051$,$\hbar\omega_{LO,y} = 0.10551$, and $\hbar\omega_{LO,z} = 0.12448eV$) at which $\varepsilon_x, \varepsilon_y$, and ε_z obtain values close to zero, respectively. We note further that, the main purpose of this study is to investigate SHTC in parallel-plate heterostructures composed of BP and polar vdW materials (i.e., hBN and MoO_3). However, it is also possible to employ the other polar materials, such as SiO_2[92, 166], Al_2O_3[93], and SiC[94, 95] to spectrally modify the SHTC. This point has been already proved in previous reports about graphene/SiO_2[166] and graphene/SiC[167] parallel-plates.

4.3 Conclusion

Summarizing, we have analyzed the NFRHT between two parallel non-rotated BP flakes due to the tunneling of the anisotropic SPPs supported by the flakes. It was shown that the covering of the BP flakes with hBN films leads to the hybridization of the BP's SPPs with the hBN's HPPs and to the significant enhancement of the NFRHT at the hBN's ENZ frequencies. We also demonstrated the possibility of actively switching between the ON and OFF states of the NFRHT by changing the chemical potential of the BP and the possibility of modifying the NFRHT via altering the number of the BP layers in the BP/hBN vdW parallel-plate

structure. The replacement of hBN with $\alpha - MoO_3$ showed the spectral and strong modification of the NFRHT in the BP/$\alpha - MoO_3$ parallel-plate structure compared to the BP/hBN one. Our results suggest the high efficiency of the analyzed structures in the thermal management of optoelectronic devices.

Chapter 5

Multifunctional tunable gradient metasurfaces for terahertz beam splitting and light absorption

This chapter is on part reprinted with permission from: **Veysel Erçağlar**, Hodjat Hajian, Andriy E. Serebryannikov, and Ekmel Özbay, *Optics Letters*, 2021, 46, 3953-3956, DOI: 10.1364/OL.435197

5.1 Introduction

Considering the importance of novel devices in advancing THz science and technology [168], in this chapter we propose a multifunctional all-dielectric gradient metasurface that is composed of a periodic array of binary Si microcylinders, with a π radian difference in the phase delay, and separated from a VO_2 film by a SiO_2 spacing layer (see fig. 1). It is shown that, for the $i-VO_2$ case, the metasurface operates as a polarization-insensitive beam splitter at 0.7 THz in transmittive mode [see fig. 5.1(c)], while it acts as a reflective beam splitter at 1.06 THz for the $m-VO_2$ case [see fig. 5.1(d)]. Moreover, by transferring graphene on the

SiO_2 layer, it is possible to tune the intensity of the split beam (in both $i-VO_2$ and $m-VO_2$ cases) as well as obtain multi-resonant nearly perfect THz light absorption in the $m-VO_2$ case.

5.2 Results and Discussion

5.2.1 Numerical and Theoretical Design of Gradient Metasurface

In our finite difference time domain (FDTD) simulations transverse magnetic (TM) and transverse electric (TE) polarizations stand for X- and Y-oriented electric field of the incident light [see Fig. 5.1(a)]. In our calculations, the refractive indices of Si and SiO_2, that can be considered as temperature-independent in this study, are chosen according to the Palik's data [156]. Moreover, the permittivity of VO_2 in the THz range can be expressed using the Drude model as $\epsilon(\omega) = \epsilon_\infty - \frac{\omega_p^2(\sigma_{VO_2})}{\omega^2+i\omega\gamma}$, where ϵ_∞=12 and the damping frequency (ω_d) is $5.75 \times 10^{13}\ s^{-1}$. Moreover, fitted with the measurements [169], the plasma frequency can be approximately described by $\omega_p^2(\sigma_{VO_2}) = \omega_p(\sigma_0)^2\frac{\sigma}{\sigma_0}$ where $\sigma_0 = 3 \times 10^5\ S/m$, $\omega_p(\sigma_0) = 1.4 \times 10^{15}\ rad/s$ and σ_{VO_2} is chosen as 10 S/m and $2 \times 10^5\ S/m$ for the $i-VO_2$ and $m-VO_2$ cases, respectively [146, 147]. Consequently, for the $i-VO_2$ and $m-VO_2$ cases, the film of VO_2 with thickness t_V (= 2 μm) acts as a transparent layer and a mirror, respectively. Moreover, $t_s = 10\ \mu m$ and the geometrical parameters of Si micropillars ($h = 180\ \mu m$ and $30 < r(\mu m) < 72$) and the unit cell dimension ($p_x = p_y = 150\ \mu m$) have been feasibly chosen according to the experimental reports [123, 140]. In order to realize the required 2π radian phase coverage, we have performed single element unit cell [see Fig. 5.1(a)] simulations for the $i-VO_2$ case at the target frequency of $f = 0.7\ THz$. The numerically calculated transmission and phase results are illustrated in Fig. 5.1(b). It is obvious that an almost 2π coverage in the phase delay is obtained by varying r from 30 μm to 72 μm while the transmission values are maintained at more than 80%.

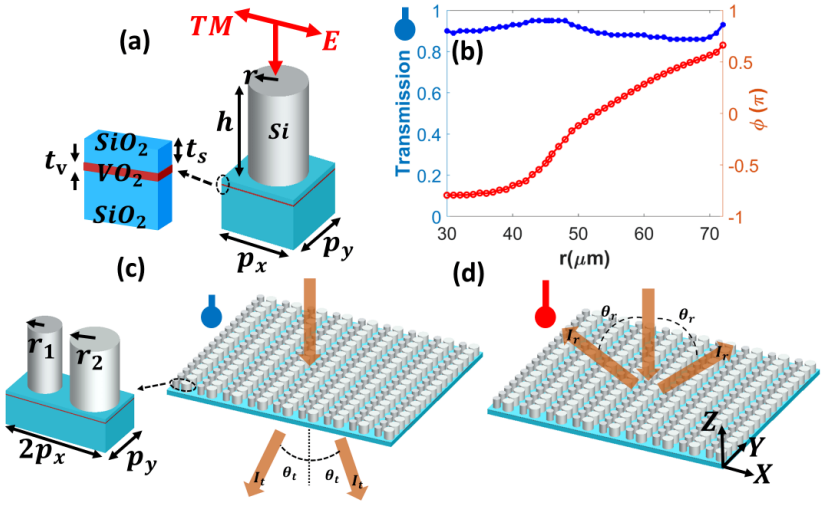

Figure 5.1: (a) Schematic of the metasurface unit cell. (b) i-VO_2 radius dependence of transmission and the phase delay at $f = 0.7\ THz$. (c) and (d) illustrate schematic and different operations of the metasurface with the split angle θ_i and intensity I_i $(i = t, r)$ for the i-VO_2 and m-VO_2 cases, respectively. The binary unit cell is also illustrated in panel (c).

For the sake of the fabrication simplicity of the MBS as well as making it polarization-insensitive, we consider a binary unit cell as shown in Fig. 5.1(c). The operating scheme of the device is also depicted in this panel where I_t denotes the intensity of the split beam for the transmission mode (the $i - VO_2$ case). It has been proven that, in case a π radian phase difference between the two adjacent elements in the binary MBS is achieved, the splitting characteristic is observed [135]. According to the results shown in Fig. 1(b), we choose $r_1 = 45.5\ \mu m$ and $r_2 = 65\ \mu m$ that results in almost $-\pi/2$ and $\pi/2$ phase delays. Consequently, the generalized Snell's law of refraction [121] predicts θ_t for normal incidence at $f = 0.7\ THz$ as

$$\theta_t = sin^{-1}(\frac{\lambda_0}{2\pi n_t}\frac{d\phi}{dx}) = sin^{-1}(\frac{\lambda_0}{2\pi n_{SiO_2}}\frac{\pm\pi}{p_x}) = \pm 45.54^o, \tag{5.1}$$

where $\lambda_0 = c/f$, c is the speed of light in free-space, $d\phi$ is the X-direction phase difference between two adjacent microcylinders in the MBS and $d_x = p_x$. The numerical results for this case are shown in Fig. 5.2.

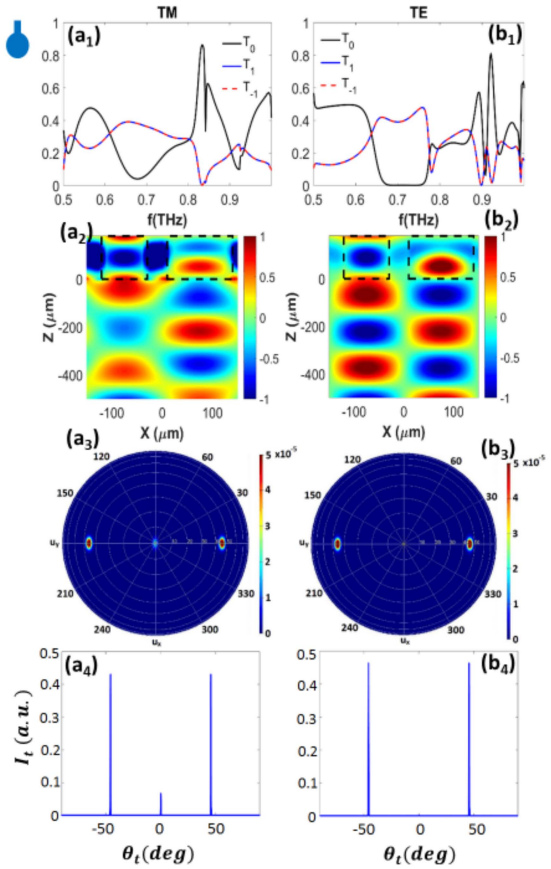

Figure 5.2: Normal incidence transmittive responses of the beam splitter for the i-VO_2 case. (a_1) different orders of light transmission through the metasurface within 0.5 THz to 1 THz. (a_2) and (a_3) the electric field mode profile and the polar plot of the far-field distribution at 0.7 THz. In agreement with (a_3), the normalized far-field intensity of transmitted power is shown in (a_4). (b_1)-(b_4) are similar to (a_1)-(a_4) but for TE polarization.

5.2.2 $i - VO_2$ case

Transmitted light through the MBS, within 0.5 THz to 1 THz, for 0^{th} (T_0, solid black), $1st$ (T_1, solid blue), and -1 (T_{-1}, dashed-red) diffraction orders are shown in panels (a_1) and (b_1) of Fig. 5.2 for TM and TE polarizations, respectively. Note that higher orders are negligible. As seen, T_1 and T_{-1} are equal at all frequencies (they represent the split transmitted powers) and T_0, that stands for non-split transmitted beam, is negligible at the target frequency (i.e. 0.7 THz). It is also understood that the suggested MBS can operate in

a frequency range spanning from 0.66 THz to 0.77 THz for both polarizations, and as expected from Eq. (5.1), θ_t is decreased while the operating frequency is increased. Outside this range, since the difference in the phase delay is not π radian, the metasurface does not act as a polarization-insensitive beam splitter. The near-field electric mode profiles at $f = 0.7\ THz$ for TM and TE polarizations are also shown in panels (a_2) and (b_2) of Fig. 5.2, respectively. It is seen that the interference pattern between the right and left splits happens similarly for both polarizations. In agreement with the near-field mode profiles, polar plots of the far-field distributions of the split beam at the corresponding frequency for both polarizations are shown in Figs. 5.2(a_3) and (b_3). As clearly observed, there is a perfect agreement between the split angle predicted by Eq. (5.1) and the one numerically obtained from the far-field calculations. This point is also understood from the normalized far-field intensity of the transmitted beam for the TM and TE polarizations represented in panels (a_4) and (b_4) of Fig. 5.2, respectively. Moreover, the splitting angle is identical for both polarizations that indicates the polarization-insensitive characteristic of the MBS for the $i - VO_2$ case. Note that it is possible to modify the operating frequency and efficiency of the MBS if different radii are chosen from Fig. 5.1(b).

5.2.3 $m - VO_2$ case

By heating the MBS up to 358 K, due to the IMT, the VO_2 layer acts as a mirror; i.e. transmission is zero. Therefore, it is possible to switch the functionality of the device from a transmittive beam splitter (the $i - VO_2$ case) to a reflective one for the $m - VO_2$ case. Reflection of the MBS within 1 THz to 1.5 THz for both TM and TE polarizations are depicted in panels (a_1) and (b_1) of Fig. 5.3. Similar to Fig. 5.2, here R_0 and $R_{\pm 1}$ stand for zeroth and $\pm$ 1-orders of reflection. Note that, at $f < 1 \sim THZ$, $R_{\pm 1} \sim 0$, thus no splitting functionality is observed. It is seen from these panels that the splitting functionality occurs for both polarizations in $1.32 < f(THz) < 1.37\ THz$ as well as some other resonant frequencies such as 1.06 THz. Moreover, R_1 and R_{-1} are identical denoting the reflected beams are split with equal powers. From the near-field mode profiles of

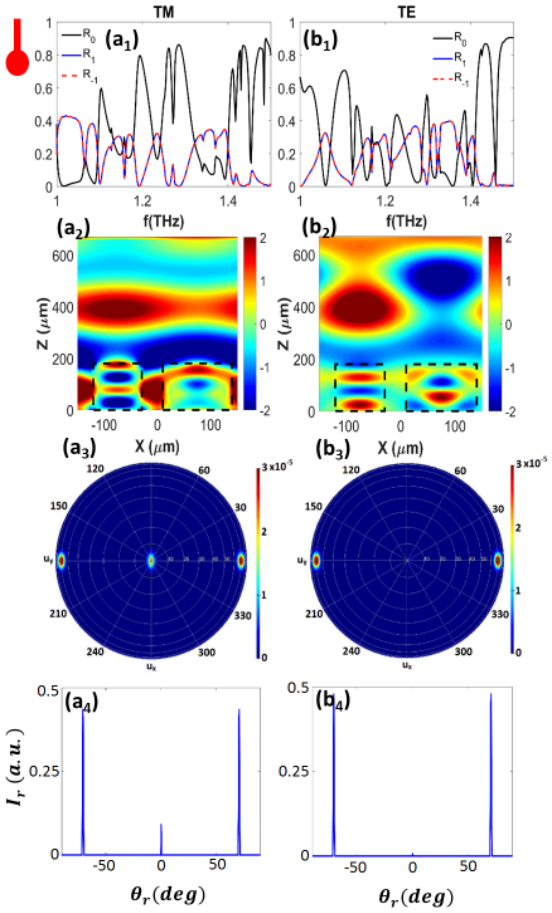

Figure 5.3: Like Fig. 5.2, but the $m-VO_2$ reflective responses of the metasurface at $f = 1.06 \sim THz$.

the reflected light, at $f = 1.06\ THz$ for TM and TE polarizations in Fig. 5.3(a_2) and Fig. 5.3(b_2), it is understood that the interference pattern between the the reflected beams occurs similarly for both polarizations. In support of the near-field responses, as clearly observed from Fig. 5.3(a_3) and Fig. 5.3(b_3), far-field distributions at both polaritions prove the reflected beam is symmetrically split with the split angle of $\theta_r \sim \pm 70^o$ and with polarization-insensitive feature. This numerically obtained θ_r is in fair agreement with the predicated value by the generalized Snell's law of reflection [121] for normal incidence at $f = 1.06\ THz$

$$\theta_r = sin^{-1}(\frac{\lambda_0}{2\pi n_i}\frac{d\phi}{dx}) = sin^{-1}(\frac{\lambda_0}{2\pi}\frac{\pm\pi}{p_x}) = \pm 70.63^o, \tag{5.2}$$

where $n_i = 1$. Normalized far-field intensity plots, shown in Fig. 5.3(a_4) and Fig. 5.3(b_4), also verify that the the reflected light is split with the aforementioned

value of θ_r. It is noteworthy that by multiplying the geometrical parameters by a factor of 1.06/0.7, it is possible to overlap the operating frequency of the device for both $i-VO_2$ and $m-VO_2$ cases.

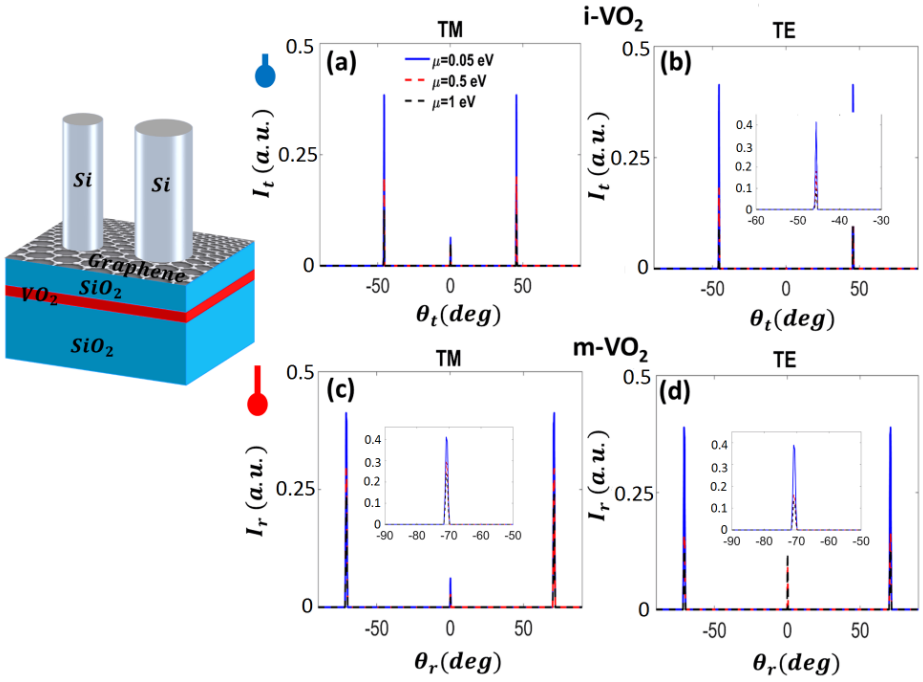

Figure 5.4: Effects of changes in μ of a single-layer graphene on the normalized far-field intensities of the split beams for the $i-VO_2$ [(a), (b)] and $m-VO_2$ cases, and both polarizations. Schematic of the unit cell is illustrated on the left hand side.

5.2.4 Graphene tuning and perfect absorption

Now, our aim is to introduce nearly perfect absorption functionality to the MBS by transferring graphene on the SiO_2 spacing layer [see the schematic in Fig. 5.4(a)] without distorting the aforementioned splitting functionalities of the $i-VO_2$ and $m-VO_2$ cases. As a two-dimensional material, graphene is well-known for the support of low-loss SPPs in the MIR and THz ranges and gate tunable optical responses via modifying its chemical potential μ. Optical conductivity of graphene, σ_g, in general is a function of angular frequency ω and temperature and is expressed as summation of both intra- and inter-band transition terms as

in Eq. 3.5 [170]. τ is the electron relaxation time chosen as 0.1 ps here. Note that in the THz range, the optical conductivity of a multilayer graphene composed of N_g layers can be considered as $\frac{N_g i e^2 \mu}{\pi \hbar^2 \Omega}$. As shown in Fig. 5.4, by introducing graphene in the MBS, it is possible to obtain an additional degree of freedom on controlling the far-field intensity of the split beam for the $i - VO_2$ [panels (a) and (b) shown at $f = 0.7\ THz$] and $m - VO_2$ [panels (c) and (d) illustrated at $f = 1.06\ THz$] cases at both polarizations. As seen from these panels, for both metallic and insulator phases of VO_2 and both polarizations, by increasing μ from 0.05 eV to 1 eV, one can switch the split beam from ON state ($I_{t,r} > 80\%$) to an almost OFF one ($I_{t,r} < 45\%$) and vice versa. Moreover, for $\mu < 0.05\ eV$ the MBS acts like graphene is absent as in Figs. 5.2 and 5.3. Finally, for the $m - VO_2$ case, by choosing t_s as 10 μm it is possible to achieve the nearly perfect absorption feature as the third functionality of the MBS for $\mu > 0.5\ eV$ (see Fig. 5.5).

For the $m - VO_2$ case, TM and TE normal incidence absorption responses of the graphene-integrated MBS are shown in panels (a) and (c) of Fig. 5.5, respectively. It is obvious that by increasing the chemical potential of graphene up to 0.5 eV and 1 eV, isotropic (e.g. at $f = 0.93\ THz$) and anisotropic (e.g. at $f = 0.63\ THz$) nearly perfect resonant absorption peaks can be obtained at some frequencies. Note that, from a practical point of view, $\mu = 1\ eV$ for a single layer graphene is equivalent to $\mu = 0.5\ eV$ for a bi-layer graphene at THz frequencies and can be obtained by top gating [171]. Moreover, the MBS can be heated simultaneously on a heating stage. As a result, in addition to transmittive and reflective splitting functionalities, the suggested device can also act as a multiresonant nearly perfect THz absorber for the "$m-VO_2$" case. To understand the absorption mechanism, we represent the mode profiles at $f = 0.93\ THz$ at which the device functions polarization-insensitively.

The side-view $|E_x|$ mode profiles in Figs. 5.5(b_2) and Fig. 5.5(d_2) illustrate resonant electric fields, for TM and TE polarizations respectively, that are captured inside the high-index microcylinders due to Fabry-Perot (FP) resonances [129]. Consequently these FP resonances excite graphene SPPs, as observed from the top-views of $|E_x|$ at $Z = 0$ plane for both TM and TE polarizations [see panels

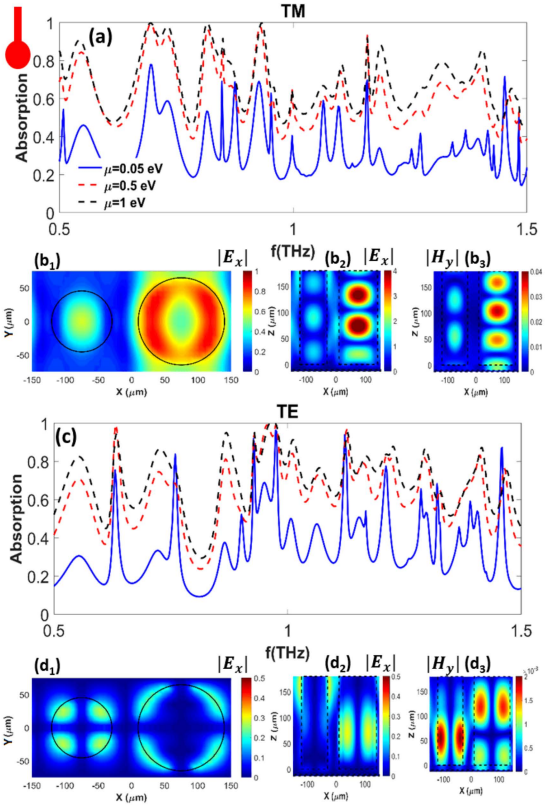

Figure 5.5: TM and TE tunable resonant absorption responses of the single-layer graphene-integrated metasurface for the $m - VO_2$ case within 0.5 THz to 1.5 THz. The mode profiles are represented at 0.93 THz with $\mu = 1$ eV.

5.5(b_1) and Fig. 5.5(d_1)]. Moreover, the side-views of $|H_y|$ in panels 5.5(b_3) and 5.5(d_3) convey this point that the magnetic fields are localized beneath the microcylinders in the SiO_2 spacing layer without any interaction with the adjacent unit cells. This point indicates that localized SPP resonances are responsible for the obtained nearly perfect resonant absorptions, as a typical characteristic of metasurface absorbers. [127].

5.3 Conclusion

To conclude, we have proposed an all-dielectric gradient metasurface that is integrated with VO_2 and graphene, and exhibits three different functionalities with

tunable characteristics in the THz range. For the $i - VO_2$ case, the metasurface acts as a transmittive beam splitter that its functionality can be switched to a reflective one for the $m - VO_2$ case. The intensity of transmitted or reflected splitted beams are also tuned via the chemical potential of graphene. Moreover, the device functions as a nearly perfect light absorber for the $m - VO_2$ case at high values of μ. It is expected that the suggested metasurface finds potential applications in THz beam splittng, multiplexing and light absorption.

Chapter 6

Conclusion and Future Outlook

In the previous chapters, the physics behind the proposed metasurfaces is explained in detail and the potential applications are shown. In this chapter, further applications in the area of 5G and beyond technologies will be discussed.

While technology is developing, people around the world getting closer than ever before they were. Communication among people is a key concern these days. Reliability and cost are the essential criteria for communication. In this regard, intensive research is conducted to ensure cheaper, faster, and more secure communication. For this reason, 5G technology is currently being set around the world. However, 5G is not coming alone, thus 5G and beyond technologies are investigated comprehensively. One of the main applications of 5G and beyond technologies is not only the communication of the people but also devices that require a large amount of data transferred and processed in a short amount of time. Systems can be exhausted while increasing the number of devices. A new concept is emerging in this perspective which is called the Internet of Things (IoT). In the following 5G and beyond as well as IoT applications of the proposed structures will be discussed.

In the second chapter, a thermally tunable spectrally selective absorber enabled by an all-dielectric metamirror was analyzed. Since the structure is highly

sensitive to temperature changes, can be used for a situation that requires high sensitivity to temperature and stability for temperature such as NASA's James Webb Space Telescope which is operating in very low and stable temperatures. Also integrated communication unit to the sensor can be the main application for IoT.

In the third chapter, a VO_2-graphene-integrated hBN-based metasurface for bi-tunable phonon-induced transparency and nearly perfect resonant absorption was investigated. The structure is highly sensitive to refractive index changes and one of the applications to the refractive index change can be the sensing of bioanalytes. In the future of 5G and beyond and IoT, medical sensors are integrated within devices such as smartwatches or glasses or even bio-robots which require sensitivity to detect changes in the environment to understand an infection or a disorder. Since the footprint of the device is small, metasurface can easily be integrated with other devices or the stand-alone device itself.

In the fourth chapter, BP/hBN and BP/$\alpha - MoO_3$ parallel-plate structures for near-field radiative heat transfer were explored. The structure itself is a device for radiative heat transfer which can be used for a radiative cooler. Since devices designed for 5G and beyond require a high amount of data processed, heat resulting from exhausting processes in the devices may cause performance losses. An integrated radiative cooler can help performance to be maintained at maximum level and energy savings for external coolers.

In the fifth chapter, a multifunctional tunable gradient metasurface for terahertz beam splitting and light absorption was studied. Terahertz is offering a large spectrum of opportunities for 5G and beyond technologies. Since the structure is already operating in the terahertz regime, the metasurface can serve as a cost-effective integrated beam splitter and electro-optic modulator in the communication channel. Besides, with the scaling principle, the device can be reconfigured to serve in infrared or microwave regions as well.

In conclusion, the proposed devices showed great opportunities for a variety of applications. Furthermore, these opportunities and advantages can be shown

experimentally as well as a future outlook.

Bibliography

[1] N. Engheta and R. W. Ziolkowski, *Metamaterials: physics and engineering explorations*. Wiley-Interscience, 2006.

[2] D. U. Yildirim, A. Ghobadi, M. C. Soydan, M. Gokbayrak, A. Toprak, B. Butun, and E. Ozbay, "Colorimetric and Near-Absolute Polarization Insensitive Refractive-Index Sensing in All-Dielectric Guided-Mode Resonance based Metasurface," *The Journal of Physical Chemistry C*, 2019.

[3] M. C. Soydan, A. Ghobadi, D. U. Yildirim, E. Duman, A. Bek, V. B. Erturk, and E. Ozbay, "Lithography-Free Random Bismuth Nanostructures for Full Solar Spectrum Harvesting and Mid-Infrared Sensing," *Advanced Optical Materials*, vol. 8, no. 4, p. 1901203, 2020.

[4] D. U. Yildirim, A. Ghobadi, and E. Ozbay, "Near-absolute polarization insensitivity in graphene based ultra-narrowband perfect visible light absorber," *Scientific Reports*, vol. 8, Oct. 2018.

[5] D. U. Yildirim, A. Ghobadi, M. C. Soydan, O. Atesal, A. Toprak, M. D. Caliskan, and E. Ozbay, "Disordered and densely packed ito nanorods as an excellent lithography-free optical solar reflector metasurface," *ACS Photonics*, vol. 6, no. 7, pp. 1812–1822, 2019.

[6] M. C. Soydan, A. Ghobadi, D. U. Yildirim, V. B. Erturk, and E. Ozbay, "All ceramic-based metal-free ultra-broadband perfect absorber," *Plasmonics*, vol. 14, pp. 1801–1815, jun 2019.

[7] M. C. Soydan, A. Ghobadi, D. U. Yildirim, V. B. Erturk, and E. Ozbay, "Deep subwavelength light confinement in disordered bismuth nanorods as

a linearly thermal-tunable metamaterial," *physica status solidi (RRL) – Rapid Research Letters*, vol. 14, p. 2000066, apr 2020.

[8] A. K. Osgouei, H. Hajian, B. Khalichi, A. E. Serebryannikov, A. Ghobadi, and E. Ozbay, "Active tuning from narrowband to broadband absorbers using a sub-wavelength VO2 embedded layer," *Plasmonics*, vol. 16, pp. 1013–1021, jan 2021.

[9] Z. Eftekhari, A. Ghobadi, M. C. Soydan, D. U. Yildirim, N. Cinel, and E. Ozbay, "Strong light emission from a defective hexagonal boron nitride monolayer coupled to near-touching random plasmonic nanounits," *Optics Letters*, vol. 46, p. 1664, mar 2021.

[10] A. K. Osgouei, A. Ghobadi, B. Khalichi, and E. Ozbay, "A spectrally selective gap surface-plasmon-based nanoantenna emitter compatible with multiple thermal infrared applications," *Journal of Optics*, vol. 23, p. 085001, aug 2021.

[11] E. Buhara, A. K. Osgouei, B. Khalichi, H. Kocer, A. Ghobadi, and E. Ozbay, "Thermally tunable from narrowband to broadband metamaterial-based nanoantenna emitter," in *2021 IEEE Photonics Conference (IPC)*, IEEE, oct 2021.

[12] B. Khalichi, A. Ghobadi, A. K. Osgouei, H. Kocer, and E. Ozbay, "A transparent all-dielectric multifunctional nanoantenna emitter compatible with thermal infrared and cooling scenarios," *IEEE Access*, vol. 9, pp. 98590–98602, 2021.

[13] D. U. Yildirim, A. Ghobadi, and E. Ozbay, "Nanosensors based on localized surface plasmon resonance," aug 2021.

[14] D. U. Yildirim, A. Ghobadi, M. C. Soydan, O. Atesal, A. Toprak, M. D. Caliskan, and E. Ozbay, "Disordered and densely packed ITO nanorods as an excellent lithography-free optical solar reflector metasurface for the radiative cooling of spacecraft," in *Metamaterials, Metadevices, and Metasystems 2019* (N. Engheta, M. A. Noginov, and N. I. Zheludev, eds.), SPIE, sep 2019.

[15] M. C. Cakir, H. Kocer, Y. Durna, D. U. Yildirim, A. Ghobadi, H. Hajian, K. Aydin, H. Kurt, N. Saglam, and E. Ozbay, "Unveiling the optical parameters of vanadium dioxide in the phase transition region: a hybrid modeling approach," *RSC Advances*, vol. 10, no. 50, pp. 29945–29955, 2020.

[16] B. Khalichi, A. Ghobadi, A. K. Osgouei, and E. Ozbay, "Diode like high-contrast asymmetric transmission of linearly polarized waves based on plasmon-tunneling effect coupling to electromagnetic radiation modes," *Journal of Physics D: Applied Physics*, vol. 54, p. 365102, jun 2021.

[17] A. K. Osgouei, H. Hajian, A. E. Serebryannikov, and E. Ozbay, "Hybrid indium tin oxide-au metamaterial as a multiband bi-functional light absorber in the visible and near-infrared ranges," *Journal of Physics D: Applied Physics*, vol. 54, p. 275102, apr 2021.

[18] A. K. Osgouei, E. Buhara, B. Khalichi, A. Ghobadi, and E. Ozbay, "Wavelength selectivity in a polarization-insensitive metamaterial-based absorber consistent with atmospheric absorption windows," in *2021 IEEE Photonics Conference (IPC)*, IEEE, oct 2021.

[19] A. K. Osgouei, B. Khalichi, E. Buhara, A. Ghobadi, and E. Ozbay, "Dual-band polarization insensitive metamaterial-based absorber suitable for sensing applications," in *2021 IEEE Photonics Conference (IPC)*, IEEE, oct 2021.

[20] B. Khalichi, Z. R. Omam, A. K. Osgouei, A. Ghobadi, and E. Ozbay, "Highly one-way electromagnetic wave transmission based on outcoupling of surface plasmon polaritons to radiation modes," in *2022 IEEE International Symposium on Antennas and Propagation and USNC-URSI Radio Science Meeting*, IEEE, jul 2022.

[21] B. Khalichi, Z. R. Omam, A. K. Osgouei, A. Ghobadi, and E. Ozbay, "A transmissive all-dielectric metasurface-based nanoantenna array for selectivity manipulation of thermal radiation," in *2022 IEEE International Symposium on Antennas and Propagation and USNC-URSI Radio Science Meeting*, IEEE, jul 2022.

[22] B. Khalichi, Z. R. Omam, A. K. Osgouei, A. Ghobadi, and E. Ozbay, "Polarization insensitive phase change material-based nanoantenna array for thermally tunable infrared applications," in *2022 IEEE International Symposium on Antennas and Propagation and USNC-URSI Radio Science Meeting*, IEEE, jul 2022.

[23] K. S. Novoselov, A. Mishchenko, A. Carvalho, and A. H. C. Neto, "2d materials and van der waals heterostructures," *Science*, vol. 353, jul 2016.

[24] P. Ajayan, P. Kim, and K. Banerjee, "Two-dimensional van der waals materials," *Physics Today*, vol. 69, pp. 38–44, sep 2016.

[25] S. Barzegar-Parizi and A. Khavasi, "Designing dual-band absorbers by graphene/metallic metasurfaces," *IEEE Journal of Quantum Electronics*, vol. 55, pp. 1–8, apr 2019.

[26] E. B. Boşdurmaz, H. Hajian, V. Erçağlar, and E. zbay, "Graphene-based metasurface absorber for the active and broadband manipulation of terahertz radiation," *Journal of the Optical Society of America B*, vol. 38, p. C160, aug 2021.

[27] J. Zhang, S. Shi, H. Jiao, X. Ji, Z. Wang, and X. Cheng, "Ultra-broadband reflector using double-layer subwavelength gratings," *Photonics Research*, vol. 8, no. 3, p. 426, 2020.

[28] S. Ogawa and M. Kimata, "Wavelength- or polarization-selective thermal infrared detectors for multi-color or polarimetric imaging using plasmonics and metamaterials," *Materials*, vol. 10, p. 493, Apr 2017.

[29] F. Monticone, R. Fleury, and A. Alu, "Physical bounds and limitations of cloaking and invisibility using passive metamaterials," *2013 USNC-URSI Radio Science Meeting (Joint with AP-S Symposium)*, 2013.

[30] M. Mutlu, S. Cakmakyapan, A. E. Serebryannikov, and E. Ozbay, "One-way reciprocal spoof surface plasmons and relevant reversible diodelike beaming," *Phys. Rev. B*, vol. 87, p. 205123, may 2013.

[31] K. Aydin, V. E. Ferry, R. M. Briggs, and H. A. Atwater, "Broadband polarization-independent resonant light absorption using ultrathin plasmonic super absorbers," *Nature Communications*, 2011.

[32] Z. Li, S. Butun, and K. Aydin, "Large-area, lithography-free super absorbers and color filters at visible frequencies using ultrathin metallic films," *ACS Photonics*, vol. 2, p. 183188, Apr 2015.

[33] D. Rosenblatt, A. Sharon, and A. Friesem, "Resonant grating waveguide structures," *IEEE Journal of Quantum Electronics*, vol. 33, no. 11, pp. 2038–2059, 1997.

[34] D. U. Yildirim, A. Ghobadi, M. C. Soydan, A. E. Serebryannikov, and E. Ozbay, "One-way and near-absolute polarization insensitive near-perfect absorption by using an all-dielectric metasurface," *Opt. Lett.*, vol. 45, no. 7, pp. 2010–2013, 2020.

[35] A. Yariv and P. Yeh, *Photonics: Optical Electronics in Modern Communications (The Oxford Series in Electrical and Computer Engineering)*. New York, NY, USA: Oxford University Press, Inc., 2006.

[36] M. J. Uddin and R. Magnusson, "Guided-mode resonant thermo-optic tunable filters," *IEEE Photonics Technology Letters*, vol. 25, no. 15, pp. 1412–1415, 2013.

[37] K.-J. Boller, A. Imamoğlu, and S. E. Harris, "Observation of electromagnetically induced transparency," *Physical Review Letters*, vol. 66, pp. 2593–2596, may 1991.

[38] M. D. Lukin and A. Imamoğlu, "Controlling photons using electromagnetically induced transparency," *Nature*, vol. 413, pp. 273–276, sep 2001.

[39] D. F. Phillips, A. Fleischhauer, A. Mair, R. L. Walsworth, and M. D. Lukin, "Storage of light in atomic vapor," *Physical Review Letters*, vol. 86, pp. 783–786, jan 2001.

[40] V. A. Fedotov, M. Rose, S. L. Prosvirnin, N. Papasimakis, and N. I. Zheludev, "Sharp trapped-mode resonances in planar metamaterials with a broken structural symmetry," *Physical Review Letters*, vol. 99, oct 2007.

[41] N. Papasimakis, Y. H. Fu, V. A. Fedotov, S. L. Prosvirnin, D. P. Tsai, and N. I. Zheludev, "Metamaterial with polarization and direction insensitive resonant transmission response mimicking electromagnetically induced transparency," *Applied Physics Letters*, vol. 94, p. 211902, may 2009.

[42] Y. Fan, T. Qiao, F. Zhang, Q. Fu, J. Dong, B. Kong, and H. Li, "An electromagnetic modulator based on electrically controllable metamaterial analogue to electromagnetically induced transparency," *Scientific Reports*, vol. 7, jan 2017.

[43] S.-Y. Chiam, R. Singh, C. Rockstuhl, F. Lederer, W. Zhang, and A. A. Bettiol, "Analogue of electromagnetically induced transparency in a terahertz metamaterial," *Physical Review B*, vol. 80, oct 2009.

[44] J. Zhou, C. Zhang, Q. Liu, J. You, X. Zheng, X. Cheng, and T. Jiang, "Controllable all-optical modulation speed in hybrid silicon-germanium devices utilizing the electromagnetically induced transparency effect," *Nanophotonics*, vol. 9, pp. 2797–2807, feb 2020.

[45] C.-Y. Chen, I.-W. Un, N.-H. Tai, and T.-J. Yen, "Asymmetric coupling between subradiant and superradiant plasmonic resonances and its enhanced sensing performance," *Optics Express*, vol. 17, p. 15372, aug 2009.

[46] S. Zhang, D. A. Genov, Y. Wang, M. Liu, and X. Zhang, "Plasmon-induced transparency in metamaterials," *Physical Review Letters*, vol. 101, jul 2008.

[47] N. Liu, L. Langguth, T. Weiss, J. Kstel, M. Fleischhauer, T. Pfau, and H. Giessen, "Plasmonic analogue of electromagnetically induced transparency at the drude damping limit," *Nature Materials*, vol. 8, pp. 758–762, jul 2009.

[48] X.-J. He, L. Wang, J.-M. Wang, X.-H. Tian, J.-X. Jiang, and Z.-X. Geng, "Electromagnetically induced transparency in planar complementary metamaterial for refractive index sensing applications," *Journal of Physics D: Applied Physics*, vol. 46, p. 365302, aug 2013.

[49] W. Wang, Y. Li, P. Xu, Z. Chen, J. Chen, J. Qian, J. Qi, Q. Sun, and J. Xu, "Polarization-insensitive plasmonic-induced transparency in planar metamaterial consisting of a regular triangle and a ring," *Journal of Optics*, vol. 16, p. 125013, nov 2014.

[50] X. Niu, X. Hu, Q. Yan, J. Zhu, H. Cheng, Y. Huang, C. Lu, Y. Fu, and Q. Gong, "Plasmon-induced transparency effect for ultracompact on-chip devices," *Nanophotonics*, vol. 8, pp. 1125–1149, jun 2019.

[51] H. Yan, T. Low, F. Guinea, F. Xia, and P. Avouris, "Tunable phonon-induced transparency in bilayer graphene nanoribbons," *Nano Letters*, vol. 14, pp. 4581–4586, jul 2014.

[52] P. Pitchappa, M. Manjappa, C. P. Ho, Y. Qian, R. Singh, N. Singh, and C. Lee, "Active control of near-field coupling in conductively coupled micro-electromechanical system metamaterial devices," *Applied Physics Letters*, vol. 108, p. 111102, mar 2016.

[53] Z. Chen, X. Song, R. Jiao, G. Duan, L. Wang, and L. Yu, "Tunable electromagnetically induced transparency in plasmonic system and its application in nanosensor and spectral splitting," *IEEE Photonics Journal*, vol. 7, pp. 1–8, dec 2015.

[54] X. Han, T. Wang, X. Li, B. Liu, Y. He, and J. Tang, "Dynamically tunable slow light based on plasmon induced transparency in disk resonators coupled MDM waveguide system," *Journal of Physics D: Applied Physics*, vol. 48, p. 235102, may 2015.

[55] J. Wu, B. Jin, J. Wan, L. Liang, Y. Zhang, T. Jia, C. Cao, L. Kang, W. Xu, J. Chen, and P. Wu, "Superconducting terahertz metamaterials mimicking electromagnetically induced transparency," *Applied Physics Letters*, vol. 99, p. 161113, oct 2011.

[56] J. Gu, R. Singh, X. Liu, X. Zhang, Y. Ma, S. Zhang, S. A. Maier, Z. Tian, A. K. Azad, H.-T. Chen, A. J. Taylor, J. Han, and W. Zhang, "Active control of electromagnetically induced transparency analogue in terahertz metamaterials," *Nature Communications*, vol. 3, jan 2012.

[57] P. Pitchappa, M. Manjappa, C. P. Ho, R. Singh, N. Singh, and C. Lee, "Active control of electromagnetically induced transparency analog in terahertz MEMS metamaterial," *Advanced Optical Materials*, vol. 4, pp. 541–547, jan 2016.

[58] H. Zhang, Y. Cao, Y. Liu, Y. Li, and Y. Zhang, "A novel graphene metamaterial design for tunable terahertz plasmon induced transparency by two bright mode coupling," *Optics Communications*, vol. 391, pp. 9–15, may 2017.

[59] S. J. Kindness, N. W. Almond, B. Wei, R. Wallis, W. Michailow, V. S. Kamboj, P. Braeuninger-Weimer, S. Hofmann, H. E. Beere, D. A. Ritchie, and R. Degl'Innocenti, "Active control of electromagnetically induced transparency in a terahertz metamaterial array with graphene for continuous resonance frequency tuning," *Advanced Optical Materials*, vol. 6, p. 1800570, aug 2018.

[60] C. Liu, P. Liu, C. Yang, Y. Lin, and S. Zha, "Dynamic electromagnetically induced transparency based on a metal-graphene hybrid metamaterial," *Optical Materials Express*, vol. 8, p. 1132, apr 2018.

[61] Y. Liu, R. Zhong, Z. Lian, C. Bu, and S. Liu, "Dynamically tunable band stop filter enabled by the metal-graphene metamaterials," *Scientific Reports*, vol. 8, feb 2018.

[62] M. Habib, M. Gokbayrak, E. Ozbay, and H. Caglayan, "Electrically controllable plasmon induced reflectance in hybrid metamaterials," *Applied Physics Letters*, vol. 113, p. 221105, nov 2018.

[63] T. Liu, H. Wang, C. Zhou, X. Jiang, and S. Xiao, "Active control of electromagnetically induced transparency analog in all-dielectric metamaterials loaded with graphene," *Journal of Physics D: Applied Physics*, vol. 53, p. 505105, oct 2020.

[64] M. Chen, Z. Xiao, X. Lu, F. Lv, and Y. Zhou, "Simulation of dynamically tunable and switchable electromagnetically induced transparency analogue based on metal-graphene hybrid metamaterial," *Carbon*, vol. 159, pp. 273–282, apr 2020.

[65] H. Hajian, I. D. Rukhlenko, G. W. Hanson, T. Low, B. Butun, and E. Ozbay, "Tunable plasmon-phonon polaritons in anisotropic 2d materials on hexagonal boron nitride," *Nanophotonics*, vol. 9, pp. 3909–3920, jun 2020.

[66] J. D. Caldwell, A. V. Kretinin, Y. Chen, V. Giannini, M. M. Fogler, Y. Francescato, C. T. Ellis, J. G. Tischler, C. R. Woods, A. J. Giles, M. Hong, K. Watanabe, T. Taniguchi, S. A. Maier, and K. S. Novoselov, "Sub-diffractional volume-confined polaritons in the natural hyperbolic material hexagonal boron nitride," *Nature Communications*, vol. 5, oct 2014.

[67] S. Dai, Z. Fei, Q. Ma, A. S. Rodin, M. Wagner, A. S. McLeod, M. K. Liu, W. Gannett, W. Regan, K. Watanabe, T. Taniguchi, M. Thiemens, G. Dominguez, A. H. C. Neto, A. Zettl, F. Keilmann, P. Jarillo-Herrero, M. M. Fogler, and D. N. Basov, "Tunable phonon polaritons in atomically thin van der waals crystals of boron nitride," *Science*, vol. 343, pp. 1125–1129, mar 2014.

[68] S. Dai, Q. Ma, M. K. Liu, T. Andersen, Z. Fei, M. D. Goldflam, M. Wagner, K. Watanabe, T. Taniguchi, M. Thiemens, F. Keilmann, G. C. A. M. Janssen, S.-E. Zhu, P. Jarillo-Herrero, M. M. Fogler, and D. N. Basov, "Graphene on hexagonal boron nitride as a tunable hyperbolic metamaterial," *Nature Nanotechnology*, vol. 10, pp. 682–686, jun 2015.

[69] M. J. Dicken, K. Aydin, I. M. Pryce, L. A. Sweatlock, E. M. Boyd, S. Walavalkar, J. Ma, and H. A. Atwater, "Frequency tunable near-infrared

metamaterials based on VO_2 phase transition," *Optics Express*, vol. 17, p. 18330, sep 2009.

[70] H. Kocer, S. Butun, E. Palacios, Z. Liu, S. Tongay, D. Fu, K. Wang, J. Wu, and K. Aydin, "Intensity tunable infrared broadband absorbers based on VO2 phase transition using planar layered thin films," *Scientific Reports*, vol. 5, aug 2015.

[71] T. G. Folland, A. Fali, S. T. White, J. R. Matson, S. Liu, N. A. Aghamiri, J. H. Edgar, R. F. Haglund, Y. Abate, and J. D. Caldwell, "Reconfigurable infrared hyperbolic metasurfaces using phase change materials," *Nature Communications*, vol. 9, oct 2018.

[72] S. Dai, J. Zhang, Q. Ma, S. Kittiwatanakul, A. McLeod, X. Chen, S. G. Corder, K. Watanabe, T. Taniguchi, J. Lu, Q. Dai, P. Jarillo-Herrero, M. Liu, and D. N. Basov, "Phase-change hyperbolic heterostructures for nanopolaritonics: A case study of hBN/VO_2," *Advanced Materials*, vol. 31, p. 1900251, mar 2019.

[73] H. Hajian, A. Ghobadi, A. E. Serebryannikov, B. Butun, G. A. E. Vandenbosch, and E. Ozbay, "VO_2-hBN-graphene-based bi-functional metamaterial for mid-infrared bi-tunable asymmetric transmission and nearly perfect resonant absorption," *Journal of the Optical Society of America B*, vol. 36, p. 1607, may 2019.

[74] X. Song, Z. Liu, J. Scheuer, Y. Xiang, and K. Aydin, "Tunable polaritonic metasurface absorbers in mid-IR based on hexagonal boron nitride and vanadium dioxide layers," *Journal of Physics D: Applied Physics*, vol. 52, p. 164002, feb 2019.

[75] S. Ye, B. Wu, Z. Wang, C. Sun, B. Wei, C. Dong, and S. Jian, "Plasmonically induced transparency in hexagon boron nitride–graphene–silica grating-based structure within the upper reststrahlen band and outside the reststrahlen band," *IEEE Photonics Journal*, vol. 11, pp. 1–13, feb 2019.

[76] Z. Zhang, J. Yang, Y. Han, X. He, J. Zhang, J. Huang, D. Chen, S. Xu, and W. Xie, "Actively tunable terahertz electromagnetically induced transparency analogue based on vanadium-oxide-assisted metamaterials," *Applied Physics A*, vol. 126, feb 2020.

[77] M. Chen, Z. Xiao, X. Lu, F. Lv, Z. Cui, and Q. Xu, "Dynamically tunable multi-resonance and polarization-insensitive electromagnetically induced transparency-like based on vanadium dioxide film," *Optical Materials*, vol. 102, p. 109811, apr 2020.

[78] D. Polder and M. V. Hove, "Theory of radiative heat transfer between closely spaced bodies," *Physical Review B*, vol. 4, pp. 3303–3314, nov 1971.

[79] A. Narayanaswamy and G. Chen, "Surface modes for near field thermophotovoltaics," *Applied Physics Letters*, vol. 82, pp. 3544–3546, may 2003.

[80] A. Lenert, D. M. Bierman, Y. Nam, W. R. Chan, I. Celanović, M. Soljačić, and E. N. Wang, "A nanophotonic solar thermophotovoltaic device," *Nature Nanotechnology*, vol. 9, pp. 126–130, jan 2014.

[81] Z. M. Zhang, *Nano/Microscale Heat Transfer*. Springer International Publishing, 2020.

[82] C. Zhou, Y. Zhang, L. Qu, and H.-L. Yi, "Near-field negative electroluminescent cooling via nanoparticle doping," *Journal of Quantitative Spectroscopy and Radiative Transfer*, vol. 245, p. 106889, apr 2020.

[83] P. Ben-Abdallah and S.-A. Biehs, "Phase-change radiative thermal diode," *Applied Physics Letters*, vol. 103, p. 191907, nov 2013.

[84] P. Ben-Abdallah and S.-A. Biehs, "Near-field thermal transistor," *Physical Review Letters*, vol. 112, jan 2014.

[85] D. Thompson, L. Zhu, R. Mittapally, S. Sadat, Z. Xing, P. McArdle, M. M. Qazilbash, P. Reddy, and E. Meyhofer, "Hundred-fold enhancement in far-field radiative heat transfer over the blackbody limit," *Nature*, vol. 561, pp. 216–221, sep 2018.

[86] P. Ben-Abdallah, K. Joulain, J. Drevillon, and G. Domingues, "Near-field heat transfer mediated by surface wave hybridization between two films," *Journal of Applied Physics*, vol. 106, p. 044306, aug 2009.

[87] S.-A. Biehs, P. Ben-Abdallah, F. S. S. Rosa, K. Joulain, and J.-J. Greffet, "Nanoscale heat flux between nanoporous materials," *Optics Express*, vol. 19, p. A1088, jul 2011.

[88] R. Guérout, J. Lussange, F. S. S. Rosa, J.-P. Hugonin, D. A. R. Dalvit, J.-J. Greffet, A. Lambrecht, and S. Reynaud, "Enhanced radiative heat transfer between nanostructured gold plates," *Physical Review B*, vol. 85, may 2012.

[89] P. Sabbaghi, L. Long, X. Ying, L. Lambert, S. Taylor, C. Messner, and L. Wang, "Super-planckian radiative heat transfer between macroscale metallic surfaces due to near-field and thin-film effects," *Journal of Applied Physics*, vol. 128, p. 025305, jul 2020.

[90] V. Fernández-Hurtado, F. García-Vidal, S. Fan, and J. Cuevas, "Enhancing near-field radiative heat transfer with si-based metasurfaces," *Physical Review Letters*, vol. 118, may 2017.

[91] J. DeSutter, L. Tang, and M. Francoeur, "A near-field radiative heat transfer device," *Nature Nanotechnology*, vol. 14, pp. 751–755, jul 2019.

[92] M. Ghashami, H. Geng, T. Kim, N. Iacopino, S. K. Cho, and K. Park, "Precision measurement of phonon-polaritonic near-field energy transfer between macroscale planar structures under large thermal gradients," *Physical Review Letters*, vol. 120, apr 2018.

[93] R. S. Ottens, V. Quetschke, S. Wise, A. A. Alemi, R. Lundock, G. Mueller, D. H. Reitze, D. B. Tanner, and B. F. Whiting, "Near-field radiative heat transfer between macroscopic planar surfaces," *Physical Review Letters*, vol. 107, jun 2011.

[94] M. Francoeur, M. P. Mengç, and R. Vaillon, "Near-field radiative heat transfer enhancement via surface phonon polaritons coupling in thin films," *Applied Physics Letters*, vol. 93, p. 043109, jul 2008.

[95] L. Tang, J. DeSutter, and M. Francoeur, "Near-field radiative heat transfer between dissimilar materials mediated by coupled surface phonon- and plasmon-polaritons," *ACS Photonics*, vol. 7, pp. 1304–1311, apr 2020.

[96] O. Ilic, M. Jablan, J. D. Joannopoulos, I. Celanovic, H. Buljan, and M. Soljačić, "Near-field thermal radiation transfer controlled by plasmons in graphene," *Physical Review B*, vol. 85, apr 2012.

[97] J.-H. Jiang and J.-S. Wang, "Caroli formalism in near-field heat transfer between parallel graphene sheets," *Physical Review B*, vol. 96, oct 2017.

[98] J. Yang, W. Du, Y. Su, Y. Fu, S. Gong, S. He, and Y. Ma, "Observing of the super-planckian near-field thermal radiation between graphene sheets," *Nature Communications*, vol. 9, oct 2018.

[99] Y. Zhang, C.-L. Zhou, L. Qu, and H.-L. Yi, "Active control of near-field radiative heat transfer through nonreciprocal graphene surface plasmons," *Applied Physics Letters*, vol. 116, p. 151101, apr 2020.

[100] Y. Zhang, H.-L. Yi, and H.-P. Tan, "Near-field radiative heat transfer between black phosphorus sheets via anisotropic surface plasmon polaritons," *ACS Photonics*, vol. 5, pp. 3739–3747, jul 2018.

[101] J. Shen, S. Guo, X. Liu, B. Liu, W. Wu, and H. He, "Super-planckian thermal radiation enabled by coupled quasi-elliptic 2d black phosphorus plasmons," *Applied Thermal Engineering*, vol. 144, pp. 403–410, nov 2018.

[102] T. Low, A. S. Rodin, A. Carvalho, Y. Jiang, H. Wang, F. Xia, and A. H. C. Neto, "Tunable optical properties of multilayer black phosphorus thin films," *Physical Review B*, vol. 90, aug 2014.

[103] T. Low, A. S. Rodin, A. Carvalho, Y. Jiang, H. Wang, F. Xia, and A. H. C. Neto, "Tunable optical properties of multilayer black phosphorus thin films," *Physical Review B*, vol. 90, aug 2014.

[104] G. Qin, X. Zhang, S.-Y. Yue, Z. Qin, H. Wang, Y. Han, and M. Hu, "Resonant bonding driven giant phonon anharmonicity and low thermal conductivity of phosphorene," *Physical Review B*, vol. 94, oct 2016.

[105] S.-A. Biehs, F. S. S. Rosa, and P. Ben-Abdallah, "Modulation of near-field heat transfer between two gratings," *Applied Physics Letters*, vol. 98, p. 243102, jun 2011.

[106] S.-A. Biehs, M. Tschikin, and P. Ben-Abdallah, "Hyperbolic metamaterials as an analog of a blackbody in the near field," *Physical Review Letters*, vol. 109, sep 2012.

[107] S. Molesky, C. J. Dewalt, and Z. Jacob, "High temperature epsilon-near-zero and epsilon-near-pole metamaterial emitters for thermophotovoltaics," *Optics Express*, vol. 21, p. A96, dec 2012.

[108] S.-A. Biehs, M. Tschikin, R. Messina, and P. Ben-Abdallah, "Super-planckian near-field thermal emission with phonon-polaritonic hyperbolic metamaterials," *Applied Physics Letters*, vol. 102, p. 131106, apr 2013.

[109] M. Lim, J. Song, S. S. Lee, and B. J. Lee, "Tailoring near-field thermal radiation between metallo-dielectric multilayers using coupled surface plasmon polaritons," *Nature Communications*, vol. 9, oct 2018.

[110] X. L. Liu and Z. M. Zhang, "Giant enhancement of nanoscale thermal radiation based on hyperbolic graphene plasmons," *Applied Physics Letters*, vol. 107, p. 143114, oct 2015.

[111] C.-L. Zhou, X.-H. Wu, Y. Zhang, H.-L. Yi, and M. Antezza, "Polariton topological transition effects on radiative heat transfer," *Physical Review B*, vol. 103, apr 2021.

[112] M.-J. He, H. Qi, Y.-T. Ren, Y.-J. Zhao, Y. Zhang, J.-D. Shen, and M. Antezza, "Radiative thermal switch driven by anisotropic black phosphorus plasmons," *Optics Express*, vol. 28, p. 26922, aug 2020.

[113] X. Liu and Y. Xuan, "Super-planckian thermal radiation enabled by hyperbolic surface phonon polaritons," *Science China Technological Sciences*, vol. 59, pp. 1680–1686, oct 2016.

[114] X. Liu, J. Shen, and Y. Xuan, "Pattern-free thermal modulator via thermal radiation between van der waals materials," *Journal of Quantitative Spectroscopy and Radiative Transfer*, vol. 200, pp. 100–107, oct 2017.

[115] K.-J. Tielrooij, N. C. H. Hesp, A. Principi, M. B. Lundeberg, E. A. A. Pogna, L. Banszerus, Z. Mics, M. Massicotte, P. Schmidt, D. Davydovskaya, D. G. Purdie, I. Goykhman, G. Soavi, A. Lombardo, K. Watanabe, T. Taniguchi, M. Bonn, D. Turchinovich, C. Stampfer, A. C. Ferrari, G. Cerullo, M. Polini, and F. H. L. Koppens, "Out-of-plane heat transfer in van der waals stacks through electron–hyperbolic phonon coupling," *Nature Nanotechnology*, vol. 13, pp. 41–46, nov 2017.

[116] Z. Zheng, N. Xu, S. L. Oscurato, M. Tamagnone, F. Sun, Y. Jiang, Y. Ke, J. Chen, W. Huang, W. L. Wilson, A. Ambrosio, S. Deng, and H. Chen, "A mid-infrared biaxial hyperbolic van der waals crystal," *Science Advances*, vol. 5, may 2019.

[117] X. Wu, C. Fu, and Z. M. Zhang, "Near-field radiative heat transfer between two $\alpha - MoO_3$ biaxial crystals," *Journal of Heat Transfer*, vol. 142, may 2020.

[118] X. Wu, C. Fu, and Z. Zhang, "Influence of hBN orientation on the near-field radiative heat transfer between graphene/hBN heterostructures," *Journal of Photonics for Energy*, vol. 9, p. 1, dec 2018.

[119] B. Zhao, B. Guizal, Z. M. Zhang, S. Fan, and M. Antezza, "Near-field heat transfer between graphene/hBN multilayers," *Physical Review B*, vol. 95, jun 2017.

[120] K. Shi, F. Bao, and S. He, "Enhanced near-field thermal radiation based on multilayer graphene-hBN heterostructures," *ACS Photonics*, vol. 4, pp. 971–978, apr 2017.

[121] N. Yu, P. Genevet, M. A. Kats, F. Aieta, J.-P. Tetienne, F. Capasso, and Z. Gaburro, "Light propagation with phase discontinuities: Generalized laws of reflection and refraction," *Science*, vol. 334, pp. 333–337, Sept. 2011.

[122] F. Aieta, P. Genevet, N. Yu, M. A. Kats, Z. Gaburro, and F. Capasso, "Out-of-plane reflection and refraction of light by anisotropic optical antenna metasurfaces with phase discontinuities," *Nano Letters*, vol. 12, pp. 1702–1706, Feb. 2012.

[123] Z. Ma, S. M. Hanham, P. Albella, B. Ng, H. T. Lu, Y. Gong, S. A. Maier, and M. Hong, "Terahertz all-dielectric magnetic mirror metasurfaces," *ACS Photonics*, vol. 3, pp. 1010–1018, May 2016.

[124] V. Erçaglar, V. Erturk, A. Ghobadi, D. U. Yildirim, and E. Ozbay, "Numerical analysis of a thermally tunable spectrally selective absorber enabled by an all-dielectric metamirror," *Optics Letters*, vol. 45, p. 6174, Nov. 2020.

[125] H. Hajian, A. Ghobadi, B. Butun, and E. Ozbay, "Active metamaterial nearly perfect light absorbers: a review [invited]," *Journal of the Optical Society of America B*, vol. 36, p. F131, July 2019.

[126] H.-T. Chen, A. J. Taylor, and N. Yu, "A review of metasurfaces: physics and applications," *Reports on Progress in Physics*, vol. 79, p. 076401, June 2016.

[127] F. Ding, Y. Yang, R. A. Deshpande, and S. I. Bozhevolnyi, "A review of gap-surface plasmon metasurfaces: fundamentals and applications," *Nanophotonics*, vol. 7, pp. 1129–1156, June 2018.

[128] F. Ding, R. Deshpande, C. Meng, and S. I. Bozhevolnyi, "Metasurface-enabled broadband beam splitters integrated with quarter-wave plate functionality," *Nanoscale*, vol. 12, no. 26, pp. 14106–14111, 2020.

[129] D. Zhang, M. Ren, W. Wu, N. Gao, X. Yu, W. Cai, X. Zhang, and J. Xu, "Nanoscale beam splitters based on gradient metasurfaces," *Optics Letters*, vol. 43, p. 267, Jan. 2018.

[130] S. Tang, F. Ding, T. Jiang, T. Cai, and H.-X. Xu, "Polarization-selective dual-wavelength gap-surface plasmon metasurfaces," *Optics Express*, vol. 26, p. 23760, Aug. 2018.

[131] X. Zhang, R. Deng, F. Yang, C. Jiang, S. Xu, and M. Li, "Metasurface-based ultrathin beam splitter with variable split angle and power distribution," *ACS Photonics*, vol. 5, pp. 2997–3002, July 2018.

[132] Z. Li, E. Palacios, S. Butun, and K. Aydin, "Visible-frequency metasurfaces for broadband anomalous reflection and high-efficiency spectrum splitting," *Nano Letters*, vol. 15, pp. 1615–1621, Feb. 2015.

[133] S. Gao, W. Yue, C.-S. Park, S.-S. Lee, E.-S. Kim, and D.-Y. Choi, "Aluminum plasmonic metasurface enabling a wavelength-insensitive phase gradient for linearly polarized visible light," *ACS Photonics*, vol. 4, pp. 322–328, Jan. 2017.

[134] Y. F. Yu, A. Y. Zhu, R. Paniagua-Domnguez, Y. H. Fu, B. Luk'yanchuk, and A. I. Kuznetsov, "High-transmission dielectric metasurface with 2? phase control at visible wavelengths," *Laser & Photonics Reviews*, vol. 9, pp. 412–418, June 2015.

[135] A. Ozer, N. Yilmaz, H. Kocer, and H. Kurt, "Polarization-insensitive beam splitters using all-dielectric phase gradient metasurfaces at visible wavelengths," *Optics Letters*, vol. 43, p. 4350, Sept. 2018.

[136] H. Kocer, Y. Durna, H. Kurt, and E. Ozbay, "Dynamic beam splitter employing an all-dielectric metasurface based on an elastic substrate," *Optics Letters*, vol. 45, p. 3521, June 2020.

[137] W. Chen, R. Chen, Y. Zhou, R. Chen, and Y. Ma, "Spin-dependent switchable metasurfaces using phase change materials," *Optics Express*, vol. 27, p. 25678, Aug. 2019.

[138] H. Kocer, A. Ozer, S. Butun, K. Wang, J. Wu, H. Kurt, and K. Aydin, "Thermally tuning infrared light scattering using planar layered thin films and space gradient metasurface," *IEEE Journal of Selected Topics in Quantum Electronics*, vol. 25, p. 4700607, May 2019.

[139] Z. Li, K. Yao, F. Xia, S. Shen, J. Tian, and Y. Liu, "Graphene plasmonic metasurfaces to steer infrared light," *Scientific Reports*, vol. 5, p. 12423, July 2015.

[140] M. Wei, Q. Xu, Q. Wang, X. Zhang, Y. Li, J. Gu, Z. Tian, X. Zhang, J. Han, and W. Zhang, "Broadband non-polarizing terahertz beam splitters with variable split ratio," *Applied Physics Letters*, vol. 111, p. 071101, Aug. 2017.

[141] X. Zang, H. Gong, Z. Li, J. Xie, Q. Cheng, L. Chen, A. P. Shkurinov, Y. Zhu, and S. Zhuang, "Metasurface for multi-channel terahertz beam splitters and polarization rotators," *Applied Physics Letters*, vol. 112, p. 171111, Apr. 2018.

[142] H. Zeng, Y. Zhang, F. Lan, S. Liang, L. Wang, T. Song, T. Zhang, Z. Shi, Z. Yang, X. Kang, X. Zhang, P. Mazumder, and D. M. Mittleman, "Terahertz dual-polarization beam splitter via an anisotropic matrix metasurface," *IEEE Transactions on Terahertz Science and Technology*, vol. 9, pp. 491–497, Sept. 2019.

[143] D. Chen, J. Yang, J. Huang, W. Bai, J. Zhang, Z. Zhang, S. Xu, and W. Xie, "The novel graphene metasurfaces based on split-ring resonators for tunable polarization switching and beam steering at terahertz frequencies," *Carbon*, vol. 154, pp. 350–356, Dec. 2019.

[144] S. Tang, F. Ding, and S. I. Bozhevolnyi, "Ultra-broadband microwave metasurfaces for polarizer and beam splitting," *EPL (Europhysics Letters)*, vol. 128, p. 47003, Jan. 2020.

[145] M. J. Dicken, K. Aydin, I. M. Pryce, L. A. Sweatlock, E. M. Boyd, S. Walavalkar, J. Ma, and H. A. Atwater, "Frequency tunable near-infrared metamaterials based on VO_2 phase transition," *Optics Express*, vol. 17, p. 18330, Sept. 2009.

[146] S. Wang, L. Kang, and D. H. Werner, "Hybrid resonators and highly tunable terahertz metamaterials enabled by vanadium dioxide (VO2)," *Scientific Reports*, vol. 7, p. 4326, June 2017.

[147] X. Li, S. Tang, F. Ding, S. Zhong, Y. Yang, T. Jiang, and J. Zhou, "Switchable multifunctional terahertz metasurfaces employing vanadium dioxide," *Scientific Reports*, vol. 9, p. 5454, Apr. 2019.

[148] V. Erçağlar, H. Hajian, and E. Özbay, "VO2–graphene-integrated hBN-based metasurface for bi-tunable phonon-induced transparency and nearly perfect resonant absorption," *Journal of Physics D: Applied Physics*, vol. 54, p. 245101, Mar. 2021.

[149] G. K. Shirmanesh, R. Sokhoyan, P. C. Wu, and H. A. Atwater, "Electro-optically tunable multifunctional metasurfaces," *ACS Nano*, vol. 14, pp. 6912–6920, Apr. 2020.

[150] E. D. Palik, *Handbook of optical constants of solids*. Academic Press, 2012.

[151] S. M. Rytov, "Electromagnetic properties of a finely stratified medium," *Soviet Physics JETP*, 1956.

[152] M. Jacques, A. Samani, E. El-Fiky, D. Patel, Z. Xing, and D. V. Plant, "Optimization of thermo-optic phase-shifter design and mitigation of thermal crosstalk on the SOI platform," *Optics Express*, vol. 27, no. 8, pp. 10456–10471, 2019.

[153] S. S. Wang and R. Magnusson, "Theory and applications of guided-mode resonance filters," *Applied Optics*, vol. 32, no. 14, p. 2606, 1993.

[154] H. Watanabe, N. Yamada, and M. Okaji, "Linear thermal expansion coefficient of silicon from 293 to 1000 k," *International Journal of Thermophysics*, vol. 25, no. 1, p. 221236, 2004.

[155] B. J. Frey, D. B. Leviton, and T. J. Madison, "Temperature-dependent refractive index of silicon and germanium," *Optomechanical Technologies for Astronomy*, 2006.

[156] E. D. Palik, *Handbook of optical constants of solids*. Academic Press, 1985.

[157] "Nanophotonic fdtd simulation software - lumerical fdtd."

[158] L. A. Falkovsky, "Optical properties of graphene," *Journal of Physics: Conference Series*, vol. 129, p. 012004, oct 2008.

[159] B. Song, A. Fiorino, E. Meyhofer, and P. Reddy, "Near-field radiative thermal transport: From theory to experiment," *AIP Advances*, vol. 5, p. 053503, may 2015.

[160] O. V. Kotov and Y. E. Lozovik, "Hyperbolic hybrid waves and optical topological transitions in few-layer anisotropic metasurfaces," *Physical Review B*, vol. 100, oct 2019.

[161] H. Hajian, I. D. Rukhlenko, V. Erçağlar, G. Hanson, and E. Ozbay, "Epsilon-near-zero enhancement of near-field radiative heat transfer in BP/hBN and BP/$\alpha - MoO_3$ parallel-plate structures," *Applied Physics Letters*, vol. 120, p. 112204, mar 2022.

[162] S. Biswas, W. S. Whitney, M. Y. Grajower, K. Watanabe, T. Taniguchi, H. A. Bechtel, G. R. Rossman, and H. A. Atwater, "Tunable intraband optical conductivity and polarization-dependent epsilon-near-zero behavior in black phosphorus," *Science Advances*, vol. 7, jan 2021.

[163] H. Hajian, I. D. Rukhlenko, G. W. Hanson, and E. Ozbay, "Hybrid surface plasmon polaritons in graphene coupled anisotropic van der waals material waveguides," *Journal of Physics D: Applied Physics*, vol. 54, p. 455102, aug 2021.

[164] H. Hajian, I. D. Rukhlenko, G. W. Hanson, T. Low, B. Butun, and E. Ozbay, "Tunable plasmon-phonon polaritons in anisotropic 2d materials on hexagonal boron nitride," *Nanophotonics*, vol. 9, pp. 3909–3920, jun 2020.

[165] B. Deng, V. Tran, Y. Xie, H. Jiang, C. Li, Q. Guo, X. Wang, H. Tian, S. J. Koester, H. Wang, J. J. Cha, Q. Xia, L. Yang, and F. Xia, "Efficient electrical control of thin-film black phosphorus bandgap," *Nature Communications*, vol. 8, apr 2017.

[166] X. L. Liu and Z. M. Zhang, "Graphene-assisted near-field radiative heat transfer between corrugated polar materials," *Applied Physics Letters*, vol. 104, p. 251911, jun 2014.

[167] M. He, H. Qi, Y. Ren, Y. Zhao, and M. Antezza, "Active control of near-field radiative heat transfer by a graphene-gratings coating-twisting method," *Optics Letters*, vol. 45, p. 2914, may 2020.

[168] H.-T. Chen, W. J. Padilla, J. M. O. Zide, A. C. Gossard, A. J. Taylor, and R. D. Averitt, "Active terahertz metamaterial devices," *Nature*, vol. 444, pp. 597–600, Nov. 2006.

[169] M. Liu, H. Y. Hwang, H. Tao, A. C. Strikwerda, K. Fan, G. R. Keiser, A. J. Sternbach, K. G. West, S. Kittiwatanakul, J. Lu, S. A. Wolf, F. G. Omenetto, X. Zhang, K. A. Nelson, and R. D. Averitt, "Terahertz-field-induced insulator-to-metal transition in vanadium dioxide metamaterial," *Nature*, vol. 487, pp. 345–348, July 2012.

[170] L. A. Falkovsky, "Optical properties of graphene," *Journal of Physics: Conference Series*, vol. 129, p. 012004, Oct. 2008.

[171] Z. Fang, S. Thongrattanasiri, A. Schlather, Z. Liu, L. Ma, Y. Wang, P. M. Ajayan, P. Nordlander, N. J. Halas, and F. J. G. de Abajo, "Gated tunability and hybridization of localized plasmons in nanostructured graphene," *ACS Nano*, vol. 7, pp. 2388–2395, Feb. 2013.

Appendix A

Scientific Contributions

1. **Veysel Erçağlar**, Volkan Erturk, Amir Ghobadi, Deniz Umut Yildirim, and Ekmel Ozbay, *Optics Letters*, 2020, 45, 6174-6177, DOI: 10.1364/OL.409586

2. **Veysel Erçağlar**, Hodjat Hajian, and Ekmel Özbay, *Journal of Physics D: Applied Physics*, 2021, 54(24), 245101, DOI: 10.1088/1361-6463/abecb2

3. Hodjat Hajian, Ivan D. Rukhlenko, **Veysel Erçağlar**, George Hanson, and Ekmel Özbay, *Applied Physics Letters*, 2022, 120, 112204, DOI: 10.1063/5.0083817

4. **Veysel Erçağlar**, Hodjat Hajian, Andriy E. Serebryannikov, and Ekmel Özbay, *Optics Letters*, 2021, 46, 3953-3956, DOI: 10.1364/OL.435197

5. Ekin Bircan Boşdurmaz, Hodjat Hajian, **Veysel Erçağlar**, and Ekmel Özbay, *Journal of the Optical Society of America B*, 2021, B 38, C160-C167, DOI: 10.1364/JOSAB.427975

6. **Veysel Erçağlar**, Hodjat Hajian, Andriy E. Serebryannikov, and Ekmel Özbay, *Proc. SPIE PC12130, Metamaterials XIII*, PC121301T, 30 May 2022, DOI: 10.1117/12.2626623

Appendix B

Code

```
import numpy as np
import matplotlib.pyplot as plt
import time

def calculate_Z(D,w,h,tao,m1,m2,f=None,ns=1.5):

    C=299792458
    eps0=8.854187817e-12
    e=1.60217662e-19
    Ef=1.0*e
    eta0=120*np.pi
    hbar=1.0545718e-34

    if f is None:
        f=np.linspace(1,50,1000)*1e12

    omega=2*np.pi*f
    betas=omega*ns/C
    sigmag=e**2*Ef*tao/(np.pi*hbar**2*(1+2j*omega*tao))
```

```
    rog=1/sigmag
    q=m2*np.pi/w

    eps_eff=eps0*(1+ns**2)/2


    YS=ns/eta0
    qs=q/(1j*omega*eps_eff)
    YG=m1*(w/D)**2*1/(rog+qs)


    YIN=YG-1j*YS/np.tan(betas*h)

    return 1/YIN

def calculate_R(Z):
    Z0=120*np.pi
    R=np.abs((Z-Z0)/(Z+Z0))**2
    return R

def print_m(a, s):
    for ii, q in enumerate(a[-1]):
        print(s[ii], q)

def ind(a,b,s,h):

    dict_n={"m1k":0, "m2k":1,"m1b":2,"m2b":3}

    a_n=dict_n[a]
    b_n=dict_n[b]
    t=(min(a_n,b_n), max(a_n,b_n))

    if t==(0,1):
```

```
            return s[max(a_n,b_n)], s[min(a_n,b_n)], h[:,:,s[2].size//2, s[3].size//2
        if t == (0, 2):
            return s[max(a_n,b_n)], s[min(a_n,b_n)], h[:,s[1].size//2,:, s[3].size//2
        if t == (0, 3):
            return s[max(a_n,b_n)], s[min(a_n,b_n)], h[:,s[1].size//2,s[2].size//2, :
        if t==(1,2):
            return s[max(a_n,b_n)], s[min(a_n,b_n)], h[s[0].size//2,:,:, s[3].size//2
        if t == (1, 3):
            return s[max(a_n,b_n)], s[min(a_n,b_n)], h[s[0].size//2,:,s[2].size//2, :
        if t == (2, 3):
            return s[max(a_n,b_n)], s[min(a_n,b_n)], h[s[0].size//2,s[1].size//2,:, :

    def run_sweep(m1sb,m2sb,m1sk,m2sk,tt,it):
        print(it)
        minrms35=[1, [0, 0, 0]]
        minrms18=[1, [0, 0, 0]]
        minrms=[1, [0, 0, 0]]
        Rs=[]
        Rb=[]
        Rm=[]
        Z_final=[]
        ii=0
        for m1k in m1sk:
            for m2k in m2sk:
                for m1b in m1sb:
                    for m2b in m2sb:
                        Zk=calculate_Z(5e-6, 3e-6, 7.5e-6, tt, m1k, m2k, f, ns)
                        Zb=calculate_Z(5e-6, 4e-6, 7.5e-6, tt, m1b, m2b, f, ns)
                        Z2=2*Zb+Zk
                        Z1=2*Zk+Zb
                        Z12=Z1*Z2/(Z1+Z2)
                        Z=Z12*Z1/(Z12+Z1)
                        R=calculate_R(Z)
```

```
                    where35=np.where((f*1e-12 < 6.5) & (f*1e-12 > 3.5))
                    sim35=sim[where35]
                    R35=R[where35]

                    where18=np.where((f*1e-12 < 8) & (f*1e-12 > 1))
                    sim18=sim[where18]
                    R18=R[where18]

                    rms35=np.sqrt(np.mean(np.power(sim35-R35, 2)))
                    rms18=np.sqrt(np.mean(np.power(sim18-R18, 2)))
                    rms=np.mean([rms35, rms18])

                    if rms35 < minrms35[0]:
                        minrms35=[rms35, [m1b, m2b, m1k, m2k]]
                        print(it, "3-5", ii, rms35, rms18)
                        Z_final=Z
                        Rs=R
                    if rms18 < minrms18[0]:
                        minrms18=[rms18, [m1b, m2b, m1k, m2k]]
                        print(it, "1-8", ii, rms35, rms18)
                        Rb=R
                    if rms < minrms[0]:
                        minrms=[rms, [m1b, m2b, m1k, m2k]]
                        print(it, "mean", ii, rms35, rms18, rms)
                        Rm=R
                    if ii%10000 == 0:
                        print(ii)

                    ii+=1
    return minrms35, minrms18, minrms, Rs, Rb, Rm, Z_final
```

```
sim=np.loadtxt("9SiOR_1eV.txt", delimiter=",")
nsio=np.loadtxt("SiO2.txt")
ns=nsio[:,1]-1j*nsio[:,2]


f=np.linspace(1,50,1000)*1e12

sim=np.interp(f*1e-12, sim[:,0], sim[:,1])


x=1 #m1k
y=1 #m2k
z=1 #m1b
w=1 #m2b

#physical limits m1k=2.52*1.1 m1b=1.42*1.1

tao=np.linspace(1.0,1.0,1)*1e-13
m1sk=np.linspace(2.7214,2.7216,x) #1
m1sb=np.linspace(0.4182,0.4225,z) #3
m2sk=np.linspace(0.377,0.3790,y) #2
m2sb=np.linspace(0.4462,0.4480,w) #4
t1=(np.linspace(-0.0,0.5,1))*1e-6
t2=(np.linspace(-0.0,0.5,1))*1e-6



legends=[]
minrms35=[1,[0,0,0]]
minrms18=[1,[0,0,0]]
minrms=[1,[0,0,0]]
Rs=[]
Rb=[]
```

```
Rm=[]
ii=0
Z_final=[]
heatmap=np.zeros((x,y,z,w))
star_time=time.time()
for i in range(1):
    minrms35, minrms18, minrms, Rs, Rb, Rm, Z_final = run_sweep(m1sb,m2sb,m1sk,m2
    print(minrms35,minrms18,minrms)

print("Sweep done in", (time.time()-star_time)*1000, "ms")
plt.plot(f*1e-12,sim)
plt.plot(f*1e-12,Rm)
print(minrms35, minrms18, minrms)
legends.append("sim")
plt.legend(legends)
plt.legend(["Simulation", "Calculation" ])
plt.ylim([0,1])
plt.xlim([0,10])
plt.xlabel("Frequency (THz)")
plt.ylabel("Reflection")
plt.show()
```